Final Technical Report

Federal Agency U. S. Department of Energy National Energy Technology Laboratory
FOA Name and Number DE-FOA-0001815
Award Number DE-EE0008384
Award Type Grant
Prime Recipient Regents of the University of Minnesota 200 Oak Street SE Suite 450 Minneapolis, MN 55455
Prime Recipient Type University
Project Title Hybrid HydraulicElectric Architecture for Mobile Machines
Principal Investigator Professor Perry Y. Li Phone: 6126267815 Fax: 6126256069 Email: lixxx099 @umn.edu
DUNS Number 555917996
Project Period September 1, 2018 - April 30, 2022
Report Date July 25, 2022

Table of Content

Hybrid Hydraulic-Electric Architecture for Mobile Machines

Final Technical Report

PI: Perry Y. Li

University of Minnesota

Executive Summary

Traditionally, off-road mobile machines such as excavators and wheel loaders are primarily powered by hydraulics, and throttling valves are used to control their work circuits. In recent years, two general trends are towards more energy efficient systems and electrification. With electrification, both efficiency and control performance can be improved by the elimination of throttling losses and the use of high-bandwidth inverter control. Electrification is generally accomplished with Electro-hydraulic actuators (EHA) but they are limited to lower powered systems due to the high cost of electric machines capable of high power or high torque. This project proposes a new system architecture for off-road vehicles - *Hybrid Hydraulic Electric Architecture* (HHEA) to improve efficiency and control performance without requiring large electric machines. The widely applicable architecture combines hydraulic power and electric power in such a way that the majority of power is provided hydraulically while electric drives are used to modulate this power. In particular, HHEA utilizes multiple common pressure rails to transmit the majority of power and small electric machines to modulate the power.

The energy-saving potential of the the HHEA has been validated for the work circuits of a variety of mobile machines, from small 5-ton excavators to medium sized 20-ton excavators and wheel loaders, and representative duty cycles to reduce energy input by 50-80% compared to the commercial state-of-art load-sensing systems. In addition, the corner power requirements of the electrical machines can be downsized by 85% compared to the EHA approach. Various tradeoff studies have also been conducted, including sensitivities to individual components performances, controllers, accumulator sizes, and variations of the system architecture etc.

A control strategy has been developed to maintain or exceed the motion control precision compared to current systems. The motion control strategy consists of a nominal controller, based on a passivity-based backstepping design, and a transition controller, based on least-norn feedforward design. The nominal controller is used in between common pressure rail switches whereas the transition controller compensates for any disturbance that common pressure rail switchings inflict on the system. The control strategy has been experimentally validated on both a medium pressure (200bar) hardware-in-the-loop (HIL) testbed and a high pressure (300+bar) HIL testbed.

An efficient and power-dense integrated electric-hydraulic machine consisting of an axial flux electric machine and a radial hydrostatic piston hydraulic machine has been designed, constructed and tested. The machine has an active material power density of 6.1kW/kg, a rated speed of 12500 RPM, and a design efficiency of 85%. This is among the highest power density electric machines using conventional materials. While the integrated machine was designed for modulating the hydraulic power within the HHEA, it can also be used in other applications.

0. Introduction and Project Overview

0.1 Background

Efficiency is an increasingly important consideration for the next generation of mobile machines such as those used in construction, agriculture, and mining. Conventional mobile machines use hydraulics as the means for power transmission, and throttling valves as the means for control. Hydraulics has been the mainstay actuation approach because of the high power nature of these machines and hydraulic being the most power-dense of all known actuation technologies. The inefficiency due to the hydraulic systems and control does not just increase fuel consumption and harmful emissions, but also necessitates larger overall systems, such as engines and heat exchangers, and decreases productivity due to lower achievable speeds. In fact, the average efficiency of such machines today is only 21% [1] with respect to the engine power output. If engine efficiency is also considered, the efficiency will only be 7%.

Another driving force in the next generation of mobile machinery is electrification. Electrification, i.e. the use of electric drives, brings the potential benefits of improved energy conversion efficiency, effective control, flexible routing, high energy density storage, and less noise and leakage. Yet, electric actuation still lags far behind hydraulics in power and force/torque densities, and the costs of high-power electric drives are still expensive compared to hydraulic equivalents.

In this project, a new system architecture for combining the merits of electric and hydraulic technologies for mobile machinery with multiple degrees of freedom, traditionally actuated by hydraulics, is proposed and studied. The architecture is shown to be highly energy efficient and controllable by exploiting the respective strengths of hydraulic actuation (such as power density) and electric actuation (such as controllability, efficiency, and energy-dense storage in batteries) while minimizing their respective weaknesses. We refer to the architecture by the name "***Hybrid Hydraulic-Electric Architecture***", HHEA in short. Here, the word "hybrid" has dual meanings: i.e. actuation by hydraulics or electric, and also power from prime-mover or from hydraulic or electric energy storage as in hybrid vehicles. The major weaknesses of hydraulic actuation are the relatively low component efficiency and that attempts to increase system efficiency are often accompanied by a decrease in control performance or an increase in system complexity and bulkiness. The primary weakness of electric actuation is that high power and high torque electric machines are expensive, heavy, and bulky, and hence not appropriate for high-power mobile machines. The latter limitation is due to the challenge to generate and maintain a large magnetic field to develop high force/torque. In contrast, for large-scale systems, hydraulics is one to two orders of magnitude more power dense and torque/force dense than electric actuation. It is because force/torque densities are primarily governed by operating pressure which is limited by material strength.

Conventional mobile machines, such as excavators, skid-steer/wheel loaders, and mowers, have multiple degrees of freedom. A state-of-the-art commercially available architecture for a multi-degree-of-freedom system is a load-sensing (LS) system in which a pressure compensated pump provides a common pressure at a level that is slightly higher (~14 bar) than the highest pressure requirement of all the services. Throttling valves are then used to drop the pressure to the required pressure of the services. This circuit can be quite efficient if all services require nearly the same pressure levels (which is not true of most systems) so that the pressure drops are kept low. However, significant throttling energy losses would be incurred if the required instantaneous pressures differ significantly, as is the case in typical systems. Moreover, energy from over-running loads is typically not recaptured due to a

mismatch in pressures. Finally, to regulate pump outlet pressure, the load-sensing pump often operates in partial displacements, which are less efficient than at full displacement. To improve efficiency over the LS system, it is necessary to i) avoid using throttling valves as the primary means of control; ii) enable the system to recapture energy from overrunning/regenerative loads; iii) improve the components' efficiency either by design or by operation (e.g. operating at full displacement instead of partial displacement); iv) operate the engine at its efficient point.

A popular approach to electrifying hydraulic machines is to utilize an electro-hydraulic actuator (EHA) setup in which an electric motor is used to drive a fixed or variable displacement hydraulic pump/motor to control the flow rate to a single actuator (Fig. 0.1). Besides being throttle-less, regenerative, and efficient, it also has good control performance. High efficiency is due to the high energy conversion efficiency of the electric drives (a combination of power inverters and electric motor/generators can have over 95% efficiency) and the fact that the hydraulic pump/motor can be a fixed displacement unit. Indeed efficiency of 80-95% over a broad operating range providing 29% energy saving has been demonstrated with EHA (see e.g. [2]). High control performance stems from the ability to adjust the torque virtually instantaneously, so as to control the speed of the hydraulic pump and to precisely control the flow in and out of the hydraulic actuator. However, because all power is provided electrically, high-power electric drives, which are prohibitive in cost and size, are needed. Therefore, the EHA approach is currently only practical for low-power machines.

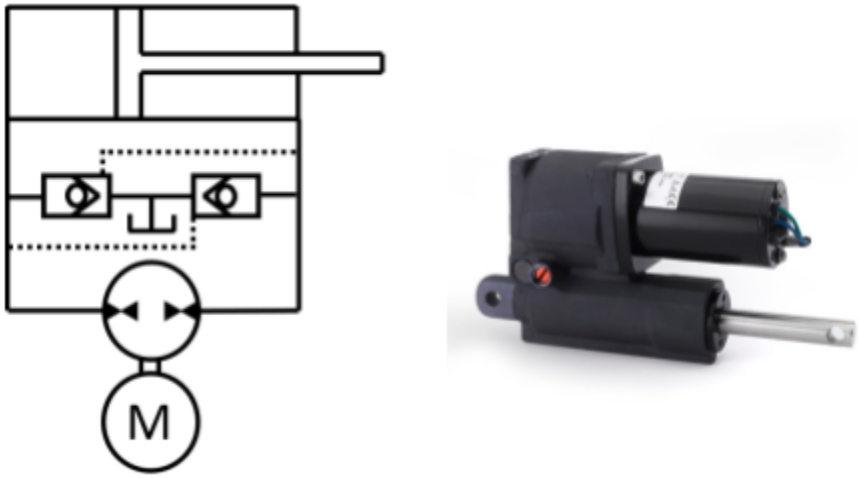

Fig. 0.1: An Electro-Hydraulic Actuator

0.2 The Proposed Hybrid Hydraulic-Electric Architecture (HHEA)

The motivation of this project is to reap the benefit of electrification without requiring large and expensive electric machines. The central idea is to use the power-dense hydraulics to transmit the majority of the power and the controllable and efficient electric actuation for modulation in order to meet the demand of the system.

The proposed HHEA is illustrated in Fig. 0.2. Each degree of freedom of the mobile machine is controlled by a hydraulic-electric control module (HECM) that combines hydraulic power from a set of common pressure-rails (CPRs) and electric power from a D.C. bus to produce precisely controlled hydraulic pressure/flow to drive linear and rotary hydraulic actuators. The architecture is augmented with

energy storages in hydraulic accumulators on the CPRs and in electric batteries on the D.C. bus. The CPR pressures can be constant (simpler) or varying (more versatile). Whereas Fig. 0.2 shows 3 pressure rails at tank, medium, and high pressures, the architecture can easily be extended to accommodate any number of pressure rails.

Each HECM is a combination of an electric motor/generator (permanent magnet AC synchronous motor) and a fixed displacement hydraulic pump/motor[1]. The HECM pump/motor is in series with the selected CPRs and the actuator. With this topology, flow to the actuator can be precisely controlled by controlling the HECM pump/motor. Moreover, the HECM needs only produce the difference between the desired pressure at the actuator and the pressure of the selected CPR. For rotary actuators, the HECM can be simplified as the pump/motor and electric drive can be mechanically coupled to the load. This offers a more direct (and hence, more efficient) path of actuating and recuperating energy from the rotational degrees of freedom.

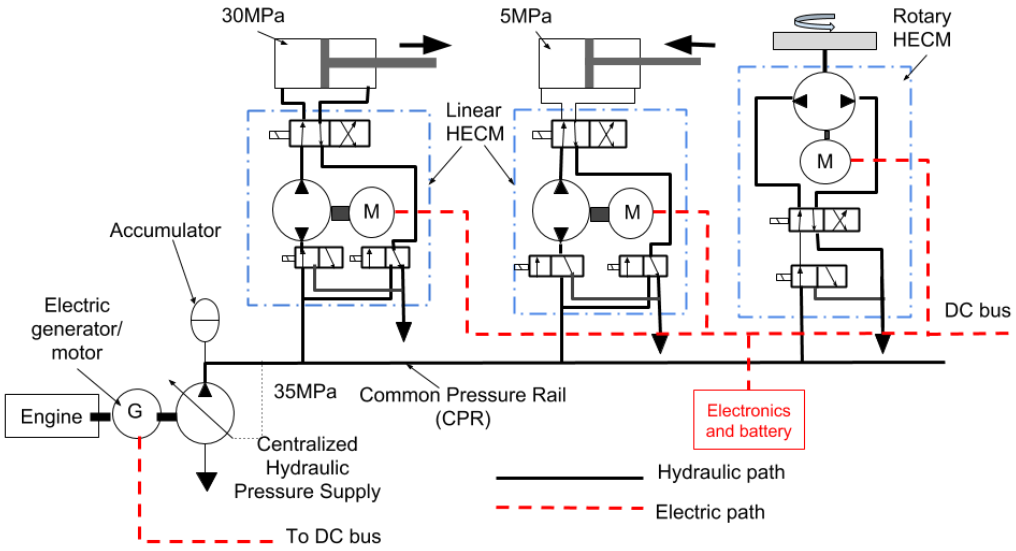

Fig 0.2: Top: The hybrid hydraulic-electric architecture (HHEA) with 3 services and 3 pressure rails at 0 MPa, 17.5 MPa, and 35 MPa. The electric generator/motor at the engine is optional. The figure shows both linear and rotary Hydraulic-Electric Control Modules (HECMs).

A set of switching valves and a directional control valve are used to select which CPRs are connected to the HECM and which actuator port is connected to the pump/motor. For example, in order to produce the desired pressure of 30 MPa, the HECM can select the 35 MPa pressure rail, whereas to produce the desired pressure of 5 MPa, the tank pressure line may be connected. In both cases, the electrical machine needs only buck or boost 5 MPa.

With 3 CPRs, there are 3x3=9 ways of connecting the pressure rails to either side of a linear actuator. Each combination provides a hydraulic force given by:

$$F_{hyd}(P_A, P_B) = P_A A_{cap} + P_B A_{rod}$$

[1] Variable displacement units would provide additional freedom for control at the expense of cost and complexity.

where P_A and $P_B \in \{P_{tank,}, P_{mid}, P_{high}\}$ and A_{cap} and A_{rod} are the capside and rodside areas of the actuator. The hydraulic force can be modulated by bucking or boosting the selected pressure by actuating the electric motor. The force provided by the electric motor is given by:

$$F_{elec} = \frac{2\pi A_{cap/rod}}{D_{HECM}} T_{elec}$$

where T_{elec} is the electric motor torque so that the total force is $F_{act} = F_{hyd} + F_{elec}$. This is illustrated in Fig. 0.3 where the horizontal lines represent the 9 possible hydraulic forces that the common pressure rails can produce. To meet the force requirement of the actuator (red curve), one can select the CPRs that correspond to a $F_{hyd}(P_A, P_B)$ close to the desired actuator force. Then the electric actuation needs only provide the difference between $F_{hyd}(P_A, P_B)$ and the desired actuator force. In contrast, with EHA, the electric motor needs to provide the entirety of the desired actuator force. Therefore, HHEA can significantly downsize the electric motor compared to an EHA approach.

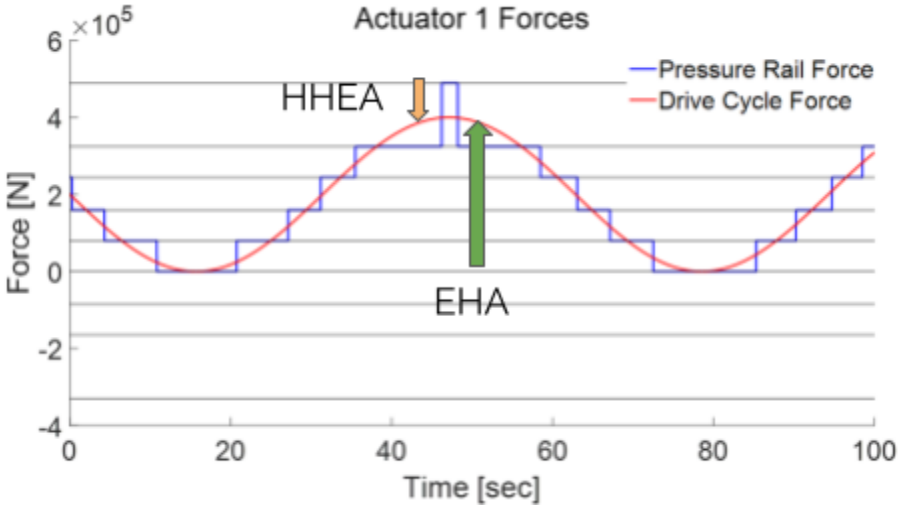

Fig. 0.3: Illustration of hydraulic forces generated using common pressure rails, electric actuation force (from HHEA or EHA), and the desired actuator force.

By controlling the electric motor/generator via efficient power electronic converters, the flow to the hydraulic cylinder or the speed of the rotary service can be controlled precisely and responsively. However, the torque required of the electric generator/motor, which is proportional to the pressure across the pump/motor, needs only be responsible for the difference between the selected CPR pressure and the required pressure of the cylinder/rotary load. If there are n CPRs (including tank), there are potentially $2n^2$ options (may not be unique) for connecting the HECM with the load and supply. Thus, by choosing the pair of pressure rails that most closely provide the desired pressure differential across the cylinder chambers, the torque and power requirements of the electric motor/generator will be significantly reduced. Note that the electric drive can either increase (boost) or decrease (buck) pressure from the selected CPR. This is in contrast to the multiple pressure rail with throttling valves approach where the throttling valves must dissipate energy [3]. Even with only 2 CPRs (including return), the torque (and hence, size) required of the electric drive is reduced by 50%, compared to a purely electrically driven conventional EHA without any hydraulic assist (Fig. 0.1). With three or four CPRs, the electric drive can theoretically be reduced by 75% and 83% (i.e. (2n-3)/(2(n-1))) respectively, etc. if the pressure levels of the rails are uniformly distributed. Further reduction can be achieved if the pressure levels are optimized.

The CPRs can be efficiently and compactly supplied by a single centralized hydraulic power supply. The outlet, and possibly the inlet as well, of the fixed displacement pump, can be alternately connected to the rails or unloaded. This enables the pump to always operate efficiently at full displacement. To avoid frequent switching of the supply pump, or large variations in the pressure levels of the pressure rails, accumulators with sufficient capacities can be installed on each rail. Accumulators also allow for efficient regeneration to occur without first motoring the power supply, thus avoiding the conversion losses associated with power cycling.

The proposed architecture combines electrical actuation and hydraulic actuation in a complementary manner to simultaneously improve efficiency, performance, and compactness. By combining them, the limitation of each actuation approach can be avoided. The proposed architecture is throttle-less and regenerative. It is highly modular and applicable to a wide range of machines, including excavators, wheel loaders, skid steer-loaders, mowers, etc. The power density and efficiency advantages of the HECM can become even greater if the hydraulic pump/motor and the electric motor/generator are intentionally integrated tightly and designed to operate at high speeds. This will have the potential of reducing mechanical friction through fewer bearings and elimination of shaft seals; reducing energy conversion losses by reducing the number of energy conversion stages; improving the power density of the electric motor and motor drive electronics enabled by hydraulic cooling of the electric components, and improving control response by reducing the rotational inertia of the integrated electric-hydraulic machine.

In summary, the proposed hybrid hydraulic-electric architecture (HHEA) is expected to have these features:

1. hydraulics is used as the majority means of power transmission
2. a centralized hydraulic power supply feeds the pressure rails
3. the engine can operate in efficient regimes and can be downsized
4. throttling is not used for control
5. precise control of hydraulic power via the electric power-inverter and the electric-drive
6. reduced size of the electric drives (motor/generator and inverter) compared with systems with only electric actuation
7. use of fixed displacement hydraulic pump/motors ensure high hydraulic efficiency,
8. can recuperate regenerative energy either electrically or hydraulically
9. energy can be stored either in hydraulic accumulators or electric batteries
10. highly modular and applicable to many platforms
11. integration of the electric motor and hydraulic pump improves power density and cost

0.3 Project objective

The objective of this project is to demonstrate a target efficiency of ≥65% (or a 40% energy saving compared with the baseline machine) in hydraulically powered off-highway vehicles through the development of an integrated hydraulic and electric system architecture applicable to a wide range of multi-degree-of-freedom mobile machines.

In this project, efficiency is defined as the ratio of positive output work to input work from the engine output. Thus engine efficiency is not considered, and since there are opportunities for recuperating energy (negative output work), this efficiency measure can theoretically be over 100%.

Specifically, this project will establish the energy-saving potential and design tradeoffs of the proposed system architecture, develop and experimentally validate a control system that can maintain or improve control performance over the conventional system, and design and prototype a compact power-dense integrated electric-hydraulic machine to be utilized as the Hydraulic Electric Control Module (HECM).

0.4 Overview of this technical progress report

The research is organized into three technical thrusts.

- **Thrust A** is concerned with evaluating the energy-saving potential of the proposed system architecture.
- **Thrust B** is concerned with the motion control performance of the machine using the proposed architecture.
- **Thrust C** is concerned with developing an efficient and compact integrated electric-hydraulic machine to be used to buck/boost pressure inside the HECM in Fig. 0.2.

The project was carried out in 3 budget periods.

- Budget period 1 (BP-1) was concerned with establishing the feasibility of the proposed architecture.
- Budget period 2 (BP-2) was concerned with establishing preliminary validation of the energy-saving potential and design approaches.
- Budget period 3 (BP-3) was concerned with establishing refined validation including the testing of prototypes and testing interactions.

In light of this organization, the report is organized accordingly, namely budget period by budget period, and within the report of each budget period, the progress of each thrust is presented. In addition, how the various milestones are met will be discussed.

1. Budget Period 1 (BP1) Technical Progress

Budget Period 1 spans the first 14 months of the project, from September 1, 2018 to October 30, 2019. The main focus is to demonstrate the feasibility of our proposed approach that :

a) the proposed hybrid hydraulic-electric architecture (HHEA) can provide at least 65% efficiency (from engine output to positive work) or 40% energy savings compared with a baseless system;
b) a control strategy suitable for the HHEA is available to provide the desired control performance;
c) the topology for the integrated electric-hydraulic conversion machine (i.e. an electric motor and hydraulic pump/motor combination) to be used in the hydraulic-electric control module (HECM) in the HHEA has the desired efficiency of 85% and gravimetric power density of 5kW/kg.

Research was conducted under the 3 thrusts: within thrust A (energy saving), an energy saving analysis tool has been developed and applied to several selected platforms to determine the energy saving potentials with the proposed HHEA. Within thrust B (control performance), a control algorithm was designed, analyzed and validated through simulation. Within thrust C (integrated electric-hydraulic machine), an integration topology was selected based on system modeling and design optimization of various hydraulic pump/motor and electric motor architectures. Through these works, the feasibility of the proposed approach has been demonstrated. In the future budget periods, the approach will be further validated through prototyping and experimentation, and refined by exploring interactions between different system objectives.

1.1 Thrust A - Energy Saving

Task 1A.1: Survey of State-of-the-Art Machines

State-of-the-art machines in 6 segments – turf, construction, agriculture, material handling, mining and forestry are surveyed, with aids from OEMs in these segments. JCB and Case New Holland (CNH) have been recruited to join the project, together with Toro and Bobcat, to serve as industry advisers. Two aspects of the survey were undertaken. The first is to understand the state of and the economic and technical drivers for electrification for each segment. The second focuses on identifying potential platforms for HHEA study. The latter survey began with a broad familiarization with the machines used in each of the five segments. Five HHEA specific criteria were determined and were used to guide discussions with OEMs in the turf, agriculture, construction and material handling segments. In these discussions, the OEMs provided information pertinent to selecting platforms for HHEA implementation. The machines were then rated according to the five identified criteria.

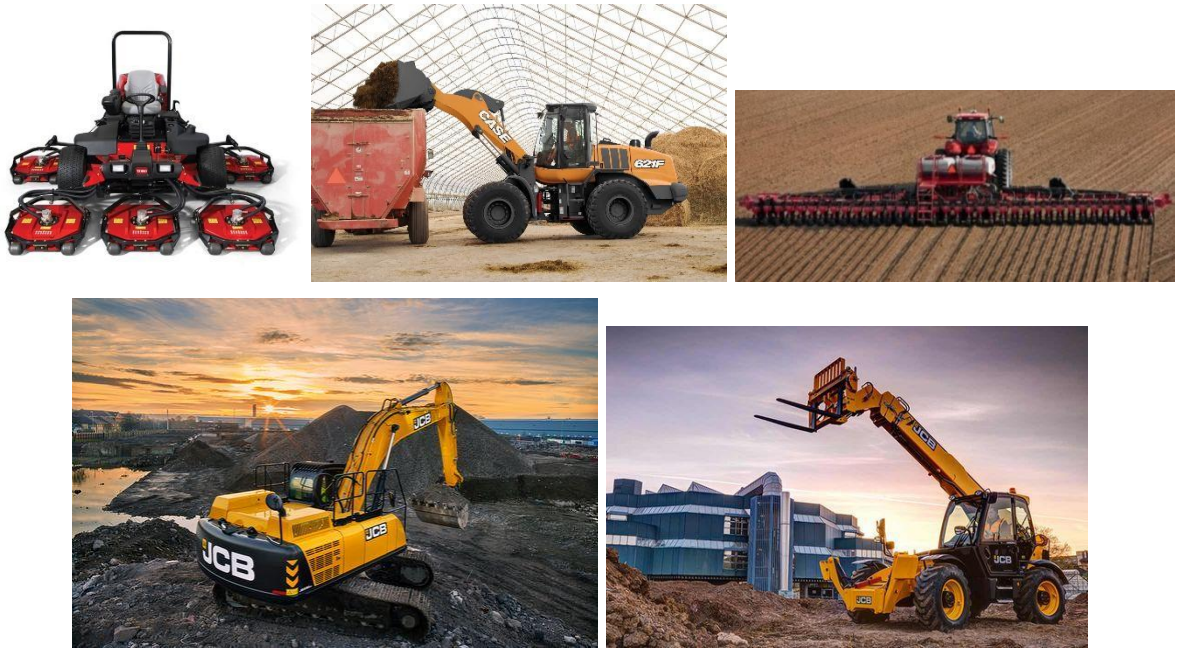

Fig. 1.A1: Identified potential platforms (from top left to bottom right): Toro Groundmaster 4700 rough mower; CNH wheel loader; CNH Early Riser planter; JCB 25-33 ton excavator; JCB telehandler.

The five candidate machines (Fig. 1.A1) that have been identified for the turf, agriculture, construction and material handling segments are: 1) Turf: Rough mowers such as the Toro Groundmaster 4700, which have multiple cutting heads, high power, and have stringent control requirements; 2) Agriculture: Planters, such as the CNH Early Riser, have multiple degrees of freedom and tight control requirements; and wheel-loaders that have a significant energy use footprint. 3) Construction: 20+ tons excavators, such as the JCB 22-Tons excavator, are too high power to be electrified directly. They are, however, prevalent in the industry, consume a large amount of energy and are not very efficient. Wheel-loaders, identified for the agriculture segment, are also widely used in construction. 5) Material handling: We have also identified the telehandler as a potential candidate for our architecture because of its control requirement and are typically multi-degree of freedom. NDAs were executed with OEM partners in order to exchange technical information and drive-cycle.

After pursuing OEMs for a long time to provide duty cycles for the planter and material handler without success, the planter and the material handlers were eventually dropped from the list of machines to consider. Duty cycles for the rough mower were obtained but were not of sufficient details to allow us to study the HHEA adequately. Instead a 5-ton excavator was added as a potential platform instead of the planter, mower, and material handler. The 5-ton excavator is a prime target for full electrification due to their prevalence in the urban setting. As urban centers, especially in Europe, are increasingly becoming more restrictive on the use of diesel engines within the cities, the trend for fully electrifying these small machines is becoming popular. It will be interesting to see how HHEA will fare for this segment of small machine segment.

Milestone 1.1, “Initial Platform Select” is thus accomplished with the selection of these platforms.

Task 1A.2: Identify Optimal Design and Energy Saving Evaluation Tool

A design tool is needed to optimize various factors such as component specifications. To accomplish this, within this tool, an outer-loop parameter and architecture design optimization, and an inner-loop control optimization must be performed. It is desired to see how one design, operated optimally, compares to another optimally operated system. See Fig. 1.A2 for an illustration of this process.

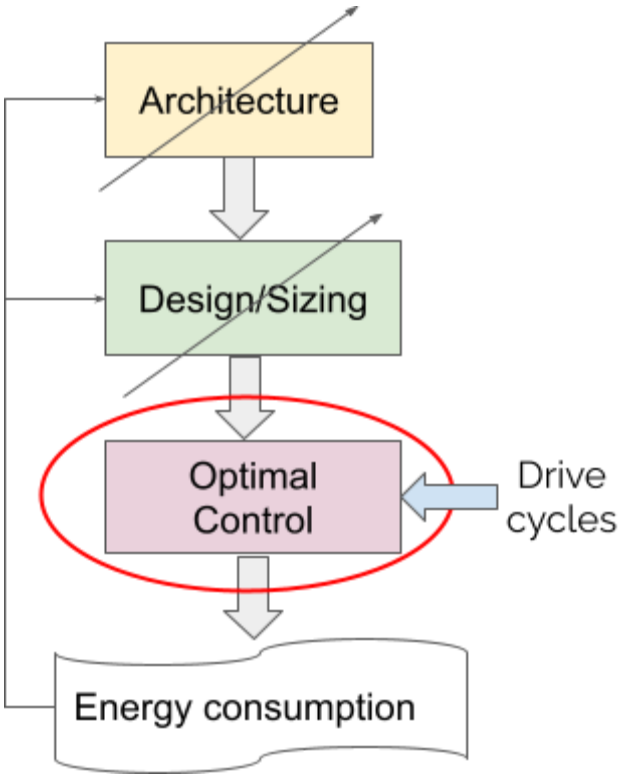

Fig. 1.A2: Flow chart for optimal control and optimal design tool

Prior to developing the design tool, a system model of the proposed architecture for a generic 3 degree-of-freedom pilot system was first developed (in Matlab/Simulink) and exercised. This enabled understanding of the operating characteristics of the proposed architecture.

1) Inner loop optimization

Given a set of pressure rails and its pressure levels, the inner-loop optimizes the operation of the system (ie. rail selection & directional valve position) that minimize energy consumption. This is done by calculating the losses that would be incurred by all operational configurations for each time in the drive cycle. The number of configurations at each time is $(2N^2)^S$ where N is the number of pressure rails and S is the number of services. For a 3 rail, 1 directional valve, 2 service machine, there are $(2x9)^2$ = 324 combinations to be considered at each time. The number of combinations increases drastically as the number of pressure rails and services increase (e.g. for N=3, S=4, there are 104976 combinations!). The combination of configurations at different times is then selected via an optimization. Hydraulic and electric losses in the Hybrid Hydraulic-Electric Control Module (HECM) and losses in the main pumps that generate the pressure rail are included. Hydraulic losses are

computed based on a generic pump/motor model obtained from the literature. Initially, electric losses were accounted for by assuming an overall electric motor-drive efficiency of 90%. This was replaced later by a detailed loss model for the electric drive (see below).

The inner-loop optimization is augmented with a constraint such that the net flow from the electric battery is zero. This is to ensure that the system does not overly draw upon stored energy in the accumulators and batteries. Accumulators, although present at each pressure rail, need not be explicitly accounted for at this stage of the analysis as long as pressure rail pressures remain nearly constant and the net flow direction of each rail is assumed. A Lagrange Multiplier method is used to solve this optimal control with constraint problem. This involves solving the following max-min problem where x(t) represents the configuration decision at each time t:

$$max_{\lambda}\, min_{x(.)} \int_{0}^{T} Losses(t,\, x(t)) \;+\; \lambda\, Power_{battery}(t)\, dt \qquad (1)$$

where λ is the Lagrange Multiplier for the equality zero net battery use constraint. Additional operational constraints, such as avoidance of cavitation and limitations on the electric motor torques can be incorporated by modifying the loss function. The Lagrange multiplier method (LMM) [4] is computationally efficient as the “inner optimization” in (1) can be parallelized. It is orders of magnitude faster than other dynamic optimal approaches such as dynamic programming. Moreover, the optimal control rule can be applied in real-time using the optimized value of λ^{*} as long as the real life drive cycle statistics are similar to those assumed in the analysis.

Fig. 1.A.3 (top) shows the selected pressure rails and the force that can be produced by the rails alone compared to the drive cycle load force. The difference (a small portion) would be made up by the electrical component in the HECM as shown in Fig. 1.A.3 (bottom). Note that although the potential pressure rail forces roughly track the load force, the choice of the rail combination is not necessarily to minimize the pressure requirement of the HECM. The optimal choice depends on the relative efficiencies of the HECM versus that of the pump driving the pressure rails.

An interesting caveat of the the optimal control problem is that with the assumption that the accumulator sizes are sufficiently large to accommodate any reverse flow on any pressurized rail, the main pump that supplies the the pressurized rails are assume to provide or absorb flow to or from the pressure rails in an unidirectional manner. This is to avoid additional energy losses in the main pump due to power cycling. Without explicitly determining how the main pump fills or absorbs flow from the pressurized rail, the expected energy loss in the main pump will be a function of the net flow on each pressurized rail. Specifically, the marginal loss associated with rail flow is conditional on the signs of the net rail flows which are unknown a priori. This prevents the efficient computational structure of normal LMM to be applied directly. Our solution is to decompose the optimization problem into a set of constrained sub-problems that are then solved via standard LMMs. For details, please see [5], [6].

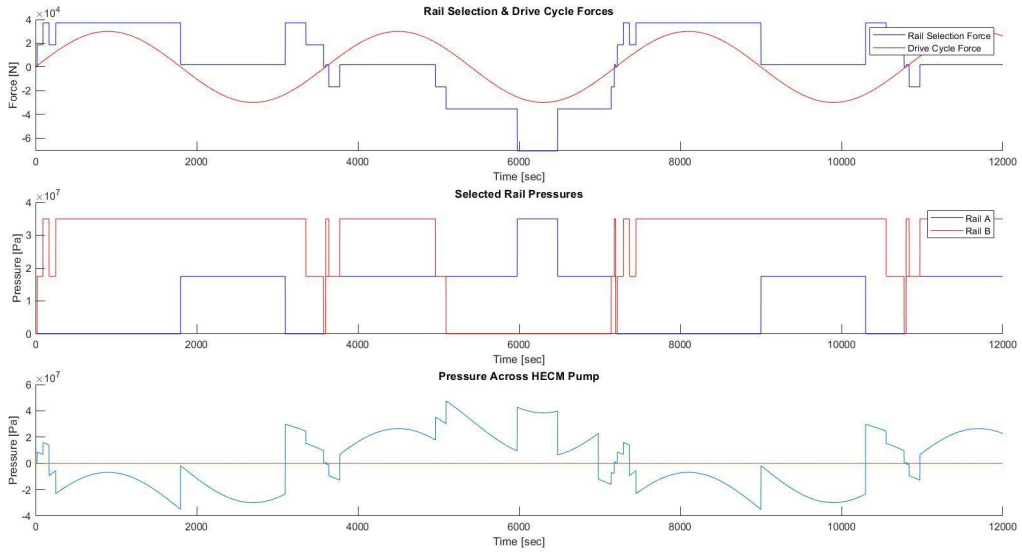

Fig. 1.A.3: Sample results of optimized pressure rails selection. Top) Force provided by selected pressure rails and duty cycle load force. Middle) Selected pressure rails. Bottom) Required pressure of the HECM.

To validate the inner loop optimal control algorithm, the algorithm was tested on a pilot system with a 2 degrees-of-freedom machine and an ad-hoc drive cycle. The results have been compared to a load-sensing architecture (which is the commercial state-of-the-art approach) in terms of energy usage. Results are encouraging which show that energy consumption can be reduced by 58% by using the proposed Hybrid Hydraulic-Electric Architecture (HHEA); and at the same time, maximum torque and corner power requirements for the electrical components are only 17-25% of what would be necessary if the system is to be electrified directly.

2) Outer-loop optimization / Optimal Design

Two types of optimal design have been investigated for Budget Period 1: pressure levels of the pressure rails, and the component sizing.

Optimization of the pressure rails' levels:

A key premise of our proposed architecture is that by using a set of pressure rails, the electric machines can be significantly downsized since they need only be used for pressure boosting or bucking. A simple idea is to uniformly distribute the pressure rails' levels between the minimum and maximum pressures. For n pressure rails, the electrical machine can then be downsized by 2(n-1) times of the maximum pressure range. Thus for n=3 or 4, the electrical machine needs only account for 25% or 13% of the maximum pressure range. A study was performed to investigate whether this downsizing benefit can be improved further when the pressure levels are optimized.

For the case with rotary actuators or linear actuators with unity area ratios, it was shown that optimizing the rails' pressure levels can indeed downsize the electrical machines further. For example, with n=3 rails, and placing the middle rail at 1/3 of the pressure range, the electrical component can be downsized further from ¼ to ⅛ of the torque necessary to generate the full pressure range, i.e. 33% reduction. Optimal solutions for up to n=10 rails have been determined. Beyond n=10, the computational cost becomes prohibitive and the solutions are no longer practical for implementation. Similar trend exists

for other n's and electrical components can be downsized by up to an additional 75%! At n=10, the electric machine needs only account for 1/72 of the maximum pressure range. The results are shown in Fig. 1A.4 (left).

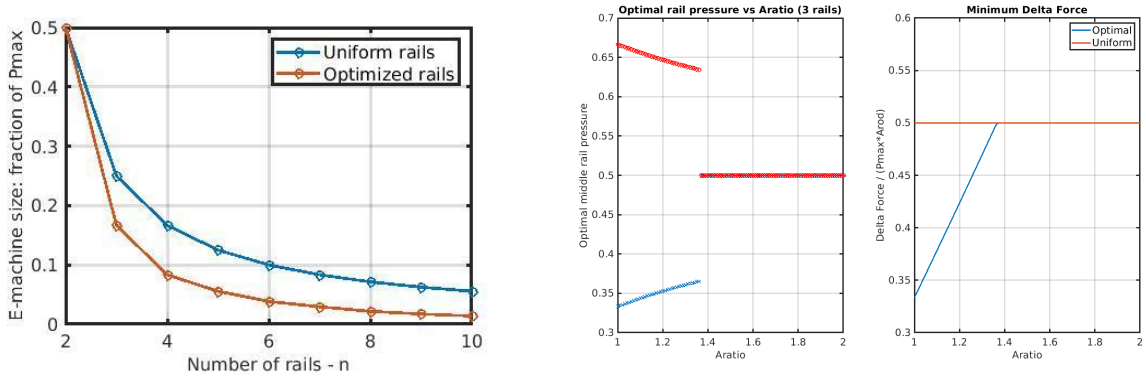

Fig. 1A.4: (Left) Component downsizing via pressure rail optimal for equal area actuators. (Right) Optimal pressure rail levels versus area ratios of unequal area actuators.

For the more common case of actuators with unequal areas on the cap-side and rod-side, the optimal pressure levels for various cylinder area ratios assuming arbitrary actuator force that span the full range have been tabulated. It was discovered that for the case of 3 pressure rails, distributing the pressure levels uniformly is in fact optimal for actuator area ratios greater than 1.28. The results for other ratios are shown in Fig. 1A.4 (right). Results for 4 pressure rails have also been similarly obtained. Furthermore, it was also shown that if the actuator force is not expected to span the full force range, further optimization can lead to even smaller electrical components.

Component sizing

Outer loop design optimization was also developed for sizing the displacements of the HECM pump/motor units. This involves embedding the inner loop optimization in a parameter optimization algorithm. According to our current pump/motor efficiency map scaling methodology and the constant speed operating strategy, the size of the main pump/motor that supplies the pressure rails will not affect the overall efficiency and therefore does not require to be optimized. For the pilot system and the pump/motor efficiency map used in the current study, increasing the displacements of the HECM pump/motors while reducing the motor operating speed increases efficiency (by as much as 10%). This result poses interesting tradeoffs between conflicting objectives as larger HECM pump/motor displacements are more expensive and also demand larger torque from the electric components. Thus, increasing efficiency this way will have negative cost implications.

Modeling losses in electric components

Whereas typical efficiency maps of hydraulic components are relatively easy to access, efficiency maps of electric drives and motors at different operating conditions are not. Therefore, a detailed efficiency map for the electric-motor and drive (for the HECM) was developed based on a detailed dynamic model of the motor and drive subsystems in the FLECS software. Fig. 1A.5 shows the efficiency map for a 3.2kW motor-drive at various speeds and torques. It shows that while our estimated average efficiency of 90% is reasonable, the efficiency at low speeds and high torque conditions deviate significantly from this estimate.

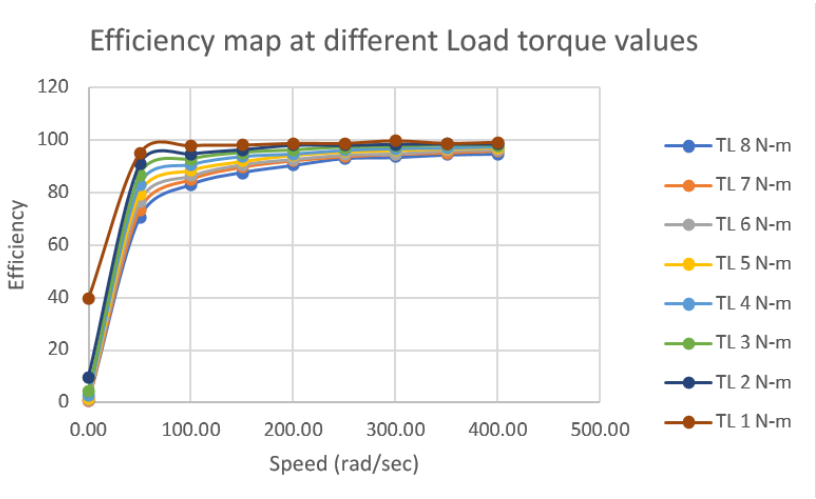

Fig. 1A.5: Efficiency of the 3.2kW motor at different speeds and torques via detailed modeling.

Other architectural considerations

The directional control valve (DCV) determines the placement of the HECM on either the cap-side or the rod-side of an actuator. The effect of fixing the HECM placement and eliminating the DCV has been investigated. Fixing the HECM placement does not change the torque or electrical requirement of the electric machines but may have implications on the overall efficiency. Placing the HECM *exclusively* on either the cap-side (with the benefit of smaller HECM pressure) or the rod-side (with the benefit of smaller HECM displacements), can reduce system complexity and simplify control strategy. For the generic machine and ad-hoc duty cycle used for testing the algorithm, it is found that restricting the HECM on the rod-side has minimal effect on the overall system efficiency. For the rest of the project, the DCV is eliminated and the HEMC is assumed to be placed on the rod-side of the actuator.

The analysis code has been demonstrated on a pilot system. It can be flexibly adapted for other machines and drive cycles.

Milestone 1.2 "Optimal Design Tool" is accomplished.

Task 1A.3: Select hybrid Hydraulic-Electric Architectures

Three sets of machine information and duty cycles have been obtained from OEMs: data for a wheel loader from CNH, data for a 5 ton mini-excavator from JCB, and data for a 22-ton excavator from JCB. The 5-ton mini-excavator was not initially selected as one of the platforms to be analyzed since such a machine is small enough to be directly electrified using electro-hydraulic actuator (EHA) approach. However, it provides an opportunity to compare the HHEA with the direct EHA approach.

The energy-saving potential of the proposed HHEA for the wheel loader and the two excavator platforms were evaluated by modeling the baseline load sensing architecture and by applying the analysis tool developed in Task 1A.2 to the platforms. The results are summarized below.

CNH 821E Wheel Loader:

Component sizing: Two duty cycles were provided by CNH - a short cycle (SC) and a long cycle (LC). The cycles have peak power demands of 90-100kW, and corner power (peak force multiplied by peak velocity) of 300kW-350kW, for each set of the tilt and lift actuators. A direct EHA approach will require

the electric machines to provide these capabilities for peak power (if a variable displacement pump/motor is used) or for corner power (if a fixed displacement pump/motor is used). With the HHEA using 3 pressure rails, the torque requirement is reduced by 85% and the power requirement is reduced by 87%. With 4 pressure rails, the corner power requirements (which is more relevant for HHEA) are reduced to 16.6kW and 20.4kW. Electrical components at this power range are readily available.

Energy consumption: The baseline load sensing (LS) system is analyzed assuming a pressure margin of 13.8 bar and that its main pump is operating at 1800 RPM. Energy consumption is analyzed in an optimistic fashion for the baseline by avoiding extra metering loss that would normally occur during over-running loads. For the HHEA, the electrical drive and motor are assumed to have an average efficiency of 90%. This assumption will be refined in the next iteration when the efficiency map for the electric drive and motor will be applied to the analysis. For fair comparison, the same pump/motor efficiency map, taken from the literature, is assumed for both the LS and HHEA systems after appropriate displacement scalings.

The distributions of the energy inputs and consumption for the long cycle (LC) with the baseline LS and the proposed HHEA are shown in Fig. 1.A5. For the LS, the potential for regenerating energy from over-running load is hardly realized and the energy is throttled away, whereas for the HHEA, regeneration is possible. Losses via throttling and component losses are also significantly reduced with HHEA compared with LS. Consequently, the efficiencies (defined as the ratio of positive output work to input work from the prime mover) with the baseline LS are only 41.3% (LC) and 47.6% (SC). With the HHEA and standard Hydraulic-Electric Control Module (HECM) pump/motor displacements of 107cc, the efficiencies are increased to 107.2% (LC) and 96.2% (SC). The results are summarized in the table below.

Table 1.A1: Efficiency and energy input for the Wheel-loader

	LC: Efficiency / Energy input	SC cycle: Efficiency / Energy input
Loadsense (Baseline)	41.3% / 19.9MJ	47.6% / 24.0 MJ
HHEA (not optimized)	107.2% / 7.7 MJ	96.2% / 11.9MJ
HHEA (size optimized)	119.0% / 6.1 MJ	119.2% / 9.6 MJ

Note that greater than 100% efficiencies are possible because of the efficiency definition being the ratio of positive output work to input work and over-running loads (negative output work) can be regenerated to help with the positive work. Energy consumption is reduced by 50%-61% from 19.9MJ (LC)/24.0MJ(SC) using the LS to 7.7MJ (LC)/11.9MJ(SC) using HHEA. If the HECM pump/motors are allowed to be optimized, further reduction of energy consumption to 6.1MJ(LC)/9.6MJ(SC), at the expense of larger HECM pump/motor sizes, are possible.

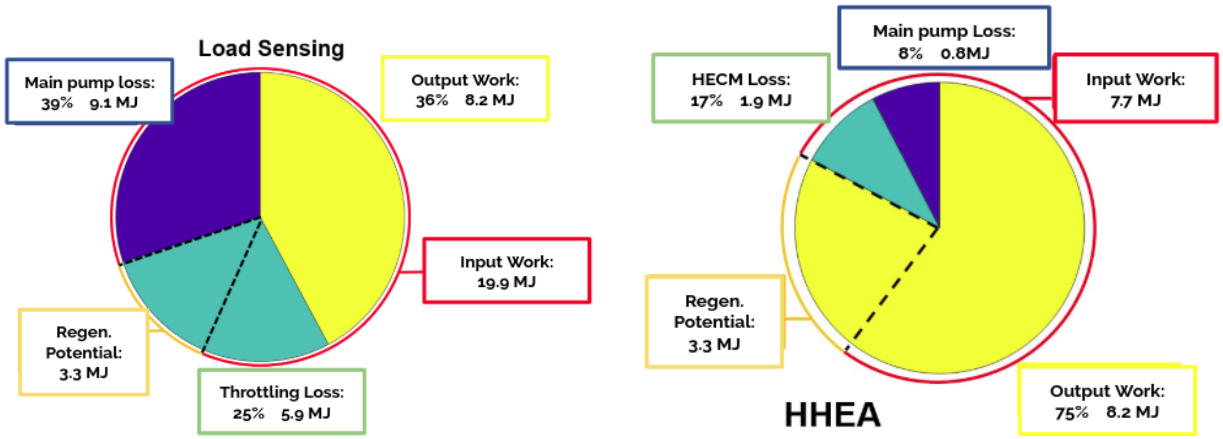

Fig. 1.A5: Left energy usage and consumption charts for the wheel-loader for the baseline load sensing system (left) and the proposed HHEA (right).

JCB 48zi mini-excavator:

For the 5-ton mini-excavator, 3 duty cycles corresponding to the 90 degree dig-swing-dump, grading, and trenching are available for analysis. In contrast to the wheel loader, the baseline load sensing system for this machine needs to actively provide flow during over-running events which increases throttling loss. Because the force and power requirement is relatively small, for the HHEA, only two pressure rails are assumed. Otherwise, the modeling approaches for the load sense baseline and for the HHEA are similar to those for the wheel loader. The efficiencies and input energies for the baseline two options of HHEA (with and without directional control valve), and direct EHA are shown in the table below.

Table 1.A2: Efficiency and energy input for the mini-excavator

	90deg: efficiency / energy input	grading: efficiency/ energy input	trenching: efficiency / energy input
LS (baseline)	29.7% / 1.64 MJ	19.5% / 1.94MJ	31.4% / 1.39 MJ
HHEA (w/ DCV)	104.9 % / 0.46MJ	61.8% / 0.61MJ	89.5% / 0.49MJ
HHEA (no DCV)	101.8 % / 0.48MJ	58.5 % / 0.65MJ	86.1% / 0.51 MJ
EHA	94.5 % / 0.51MJ (elect)	57.8 % / 0.66 MJ (elect)	86.3% / 0.51 MJ (elect)

Thus, the HHEA options are 3 times more efficient and save over 65% of input energy. Note also that eliminating the directional control valve (DCV) reduces efficiency minimally but is beneficial in reducing complexity and improving control performance. It is also interesting to note that HHEA and EHA have similar efficiency but HHEA has the benefit of smaller torque requirements for the electric motors and smaller battery size, and is therefore potentially lower cost.

As an illustration of the distributions of the energy input and energy consumptions, the pie-charts for the trenching cycle are shown in Fig. 1.A6 for the load sense and the HHEA. Similar to the wheel

loader case, energy losses through throttling and component inefficiencies are reduced significantly, and energy from over-running loads are regenerated with the HHEA.

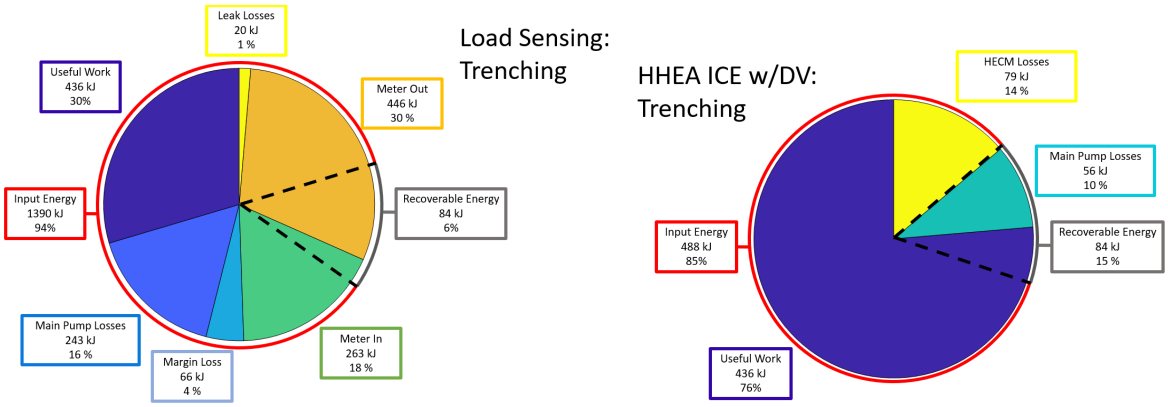

Fig. 1.A5: Left energy usage and consumption charts for the mini-excavator for the baseline load sensing system (left) and the proposed HHEA (right).

JCB 22 ton-excavator:

For the 22-ton mini-excavator, 3 duty cycles corresponding to the 90 degree dig-swing-dump, grading, and trenching are available for analysis. Because of the large power, three pressure rails are assumed. Based on results from the mini-excavator, the DCV is eliminated and the HECM is fixed on the rod side of the actuator. The modeling approaches for the load sense baseline and for the HHEA are similar to those for the wheel loader. The efficiencies and input energies for the baseline and the 3 rail HHEA are shown in the table below indicating the HHEA is 3 times more efficient (over 65% energy saving).

Table 1.A3: Efficiency and energy input for the 22 ton-excavator

	90deg: efficiency / energy input	grading: efficiency/ energy input	trenching: efficiency / energy input
LS (baseline)	38.3%/14.2MJ	22.7% /12.5MJ	35.1% / 13.1 MJ
HHEA (no DCV)	121.4 % / 4.48MJ	103.2 % / 2.75MJ	103% / 4.46 MJ

To illustrate the benefit of HHEA in terms of reducing electrical component sizes. The power requirements for the electrical components for a direct EHA and the HHEA architectures are shown in the table below.

Table 1.A4: Electrical component size requirements for the 22 ton excavator

	Axis 1	Axis 2	Axis 3	Axis 4
Direct EHA (peak/corner power)	59/108 kW	23/302 kW	12.6/212 kW	42/80 kW
4 rail HHEA (corner power)	10.6 kW	24 kW	17 kW	15 kW

This analysis above shows that the HHEA does provide, for both the wheel-loader, the mini-excavator, and the large excavator the target efficiency (> 65%) and energy saving (> 40%) for this project and for the BP1 go/no-go decision.

1.2 Thrust B: Control Performance

Task 1.B1: Survey of control/modeling paradigms

This task involves reviewing control oriented modeling paradigms for hydraulic control systems. The survey includes control methodology for the energy management of hybrid vehicles as well as for trajectory tracking of hydraulic actuators.

Task 1.B2: Develop control-oriented HECM model

A control-oriented HECM model has been constructed that includes pressure dynamics and switchable pressure rails. At first, the pump/motor speed was used as the control input, later electric motor torque was used as input. The model is sufficient for investigating the nominal HECM control strategy. The model can be exercised in combination with models of electrical drives and motors, but with great computational expense, to determine if using motor torque as input is sufficiently accurate.

Task 1.B3: Nominal HECM control strategy

A passivity-based, backstepping control strategy as a basis to control the HECM in between pressure rail switching events. The dynamics of the system are given by:

$$M\ddot{x} = P_{cap}A_{cap} - P_{rod}A_{rod} - F_L - f$$

$$\dot{P}_{rod} = \frac{\beta}{V_{rod}(x)}(Q + A_{rod}\dot{x})$$

$$Q = \frac{D}{2\pi}\omega$$

$$J\dot{\omega} = \frac{(P_B - P_{rod})D}{2\pi} + T_m$$

Control design proceeds from assuming successively rod-side cylinder pressure P_{rod}, pump flow Q, and finally, electric motor torque T_M as the inputs. At each step, the Lyapunov function for proving stability is successively extended to include additional states by adding to it the energy associated with that state. In passivity based backstepping, the Lyapunov functions are motivated by natural energy functions(Li and Wang 2014).

Since the method makes use of the natural energetic interactions between components, the approach is potentially more robust. Theoretical nonlinear systems analysis (based on Lyapunov functions) has been conducted showing that this control strategy leads to stable trajectory tracking in the absence of pressure rail switching events. Figure 1.B1 shows that with HECM pump/motor torque as input, the algorithm successfully tracks a position trajectory provided by an OEM with a maximum tracking error of 5mm. For a more detailed description of the passivity-based backstepping controller, see [7].

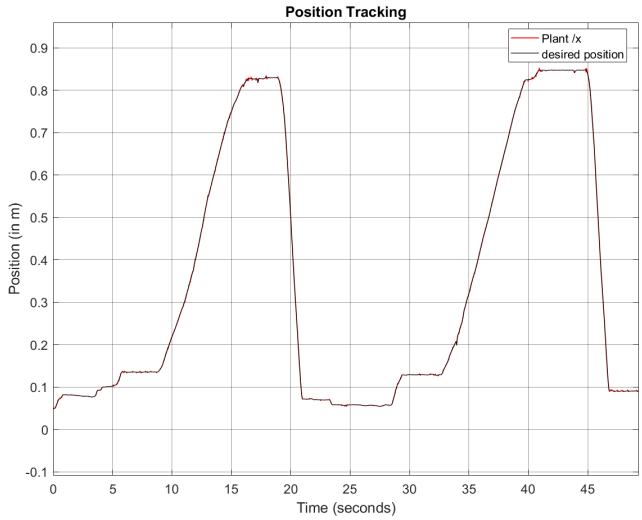

Fig. 1.B1: Simulation of the passivity-based back-stepping controller using mechanical torque as input.

Since the HECM mechanical torque is provided by the electric motor, the impact that the mechanical torque is not the actual input is evaluated. To this end, a detailed model of an electric drive and electric motor combination was first developed in Matlab/Simulink. Figure 1.B2 illustrates the modeling strategy except that the outer-loop speed/position control is replaced by the passivity-based back-stepping control and the permanent magnet synchronous machine (PMSM) is augmented with external load and inertia corresponding to the HECM hydraulic pump/motor that it is connected to. The electronic switching frequency is assumed to be 20kHz and the inner loop proportional-integral (P-I) torque controller is tuned for a 1kHz bandwidth. Although the motor-drive is modeled for a 3.5kW system, for use with the HHEA system, the torque and power capabilities are scaled while maintaining the efficiency profiles for a given speed and fractional torque.

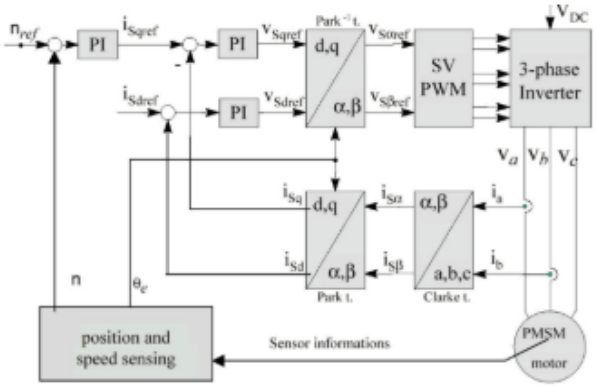

Fig. 1.B2: Block diagram of the electrical model used for energy saving analysis and control strategy.

The time-response of the electric drive's D-Q current stabilizes quickly as the demanded torque is varied. The consequence of this response is that the desired motor torque and the actual output torque are nearly identical as shown in Fig. 1.B3. Finally, Fig. 1.B4 shows that the position tracking performances, with torque as input or with reference torque for the electric drive as input, are also nearly identical. This

means that as far as control performance is concerned, the dynamics of the electric drive/motor can be ignored, thus significantly simplifying the control design and reducing simulation times.

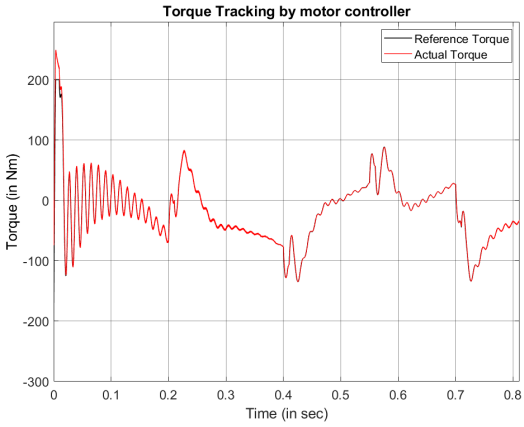

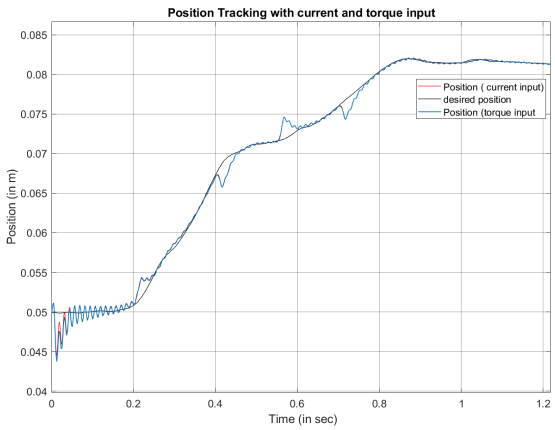

Fig. 1.B3: Command torque & achieved torque.

Fig. 1.B4: Position tracking w/torque or electric input

Figure 1.B4 illustrates that position tracking can be achieved using the passivity-based back-stepping control algorithm despite the electric drive-motor dynamics. The occasional deviations from the desired trajectory take place at instances of pressure rail switching events. The presence of this error is expected and can be mitigated with the nominal controller by increasing the control gains, at the expense of increased torque demand from the electric motor/drive. This is feasible with the use of charging capacitors to provide large transient currents. A more systematic approach of developing a "transition" controller that explicitly deals with the pressure rail transition events will be discussed below.

Milestone 1.3 "nominal control" is accomplished.

Task 1.B4: Verify HECM control strategy

The main task of verifying the control strategy under various scenarios is to develop alternative approaches to mitigate the effect of pressure rail switching, without the need for a significant increase in motor torque requirement. One approach is to reduce the frequency of pressure rail switching by preferring to use currently selected rails by introducing a decaying penalty to rail switching. Another approach is to alter the relative timing of the pressure rails switchings. For example, if the HECM is placed on one side of the actuator, the rail switching on the opposite side can be delayed to allow time for the pressure on the capside to reach the required level. Results show that both strategies are effective, with the latter reducing the torque requirement by 67% while achieving the same tracking performance. Fig. 1.B5 illustrates that with the introduction of the rail-switching penalty, spurious switching events were minimized leading to a significant reduction in control errors.

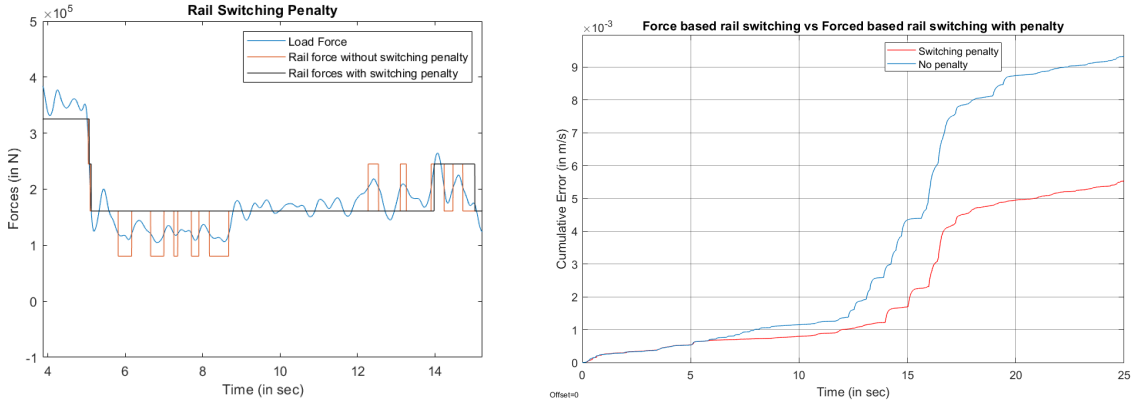

Fig. 1.B5. (Left) Rail selections with and without switching penalty. (Right) Integrated position errors with and without switching penalty.

Figure 1.B6 illustrates a preliminary concept of "transition control" wherein the electric motor anticipates a disturbance due to pressure rails switch and acts to preemptively compensates. In BP.1, this concept was realized using a delayed switch and a bang-bang control of the electric motor. As seen in Fig. 1.B6, the bang bang control initiates a fast accelerating prior to the transition followed by a fast deceleration. For this particular pressure rail switch, the controller is able to reduce position error from 7.1mm to 0.5mm, thus validating the concept. The timings of the bang-bang control were however critical. In BP1, they were determined by a computationally expensive offline optimization for each switch. This idea of a "transition control" will be formalized in BP2 using the least norm control concept which is much more amenable to real-time implementation.

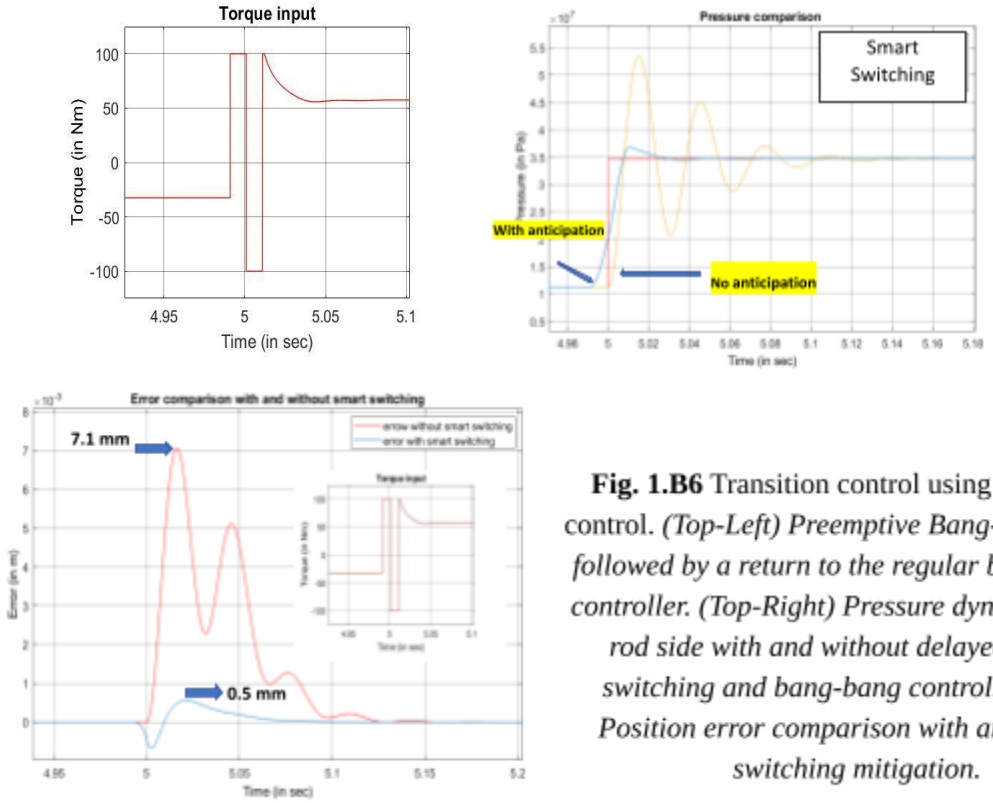

Fig. 1.B6 Transition control using bang-bang control. *(Top-Left) Preemptive Bang-bang control followed by a return to the regular backstepping controller. (Top-Right) Pressure dynamics on the rod side with and without delayed capside switching and bang-bang control. (Bottom) Position error comparison with and without switching mitigation.*

1.3 Thrust C: Integration

Thrust C focuses on the hydraulic-electric integrated control module. Subtasks were carried out for developing the hydraulic pump/motor, the electric motor, and their integration.

Task 1.C1: Select topology for integration

Subtask 1.C1-1: Identify Design Requirements

Selecting a hydraulic topology for the HECM requires knowledge of the operating conditions for the pump/motor unit. Operation is drive-cycle specific but in general, the architecture will operate in all 4 quadrants, which necessitates passing through zero speed. It will need to reach maximum speeds of up to 15000 rpm efficiently. The hydraulic topologies considered were: external gear, internal gear, gerotor, vane, radial piston, and axial piston. An in-depth consideration of design parameters was laid out in a Pugh matrix to evaluate the merit of different hydraulic architectures. The criteria used are listed in Table C1. Analysis of the Pugh matrix suggested that the gerotor and radial ball piston were the best candidates.

Table 1.C1: Design requirements used to evaluate different hydraulic pump/motor topologies

Criteria	**Description**
Maximum Speed Capability	Does the architecture have the potential to run at high speeds
Displacement Density	How much fluid is displaced for a given mass
Cost	Dollar amount
Volumetric efficiency @ high pressure	How volumetrically efficient is the system at high pressure
Mechanical Efficiency @ low speed	How mechanically efficient is the system at low speed
Mechanical Efficiency @ high speed	How mechanically efficient is the system at high speed
Ease of integration	How easily can the architecture become electrically integrated
Ease of valves	How easily can the architecture have active valves
Stick-Slip @ low speed	How noticeable is the stick-slip behavior of the architecture at low speeds
Wear and reliability	How much wear occurs within the architecture
Noise	How loud is the architecture

After completing the Pugh matrix and evaluating different architectures, two possible designs seemed most reasonable. An axial flux electric machine driving a radial ball piston pump or a radial flux electric machine driving a gerotor pump.

Subtask 1.C1-2: Identify Interfacing Constraints

The hydraulic pump is proposed to fit within the rotor of the radial flux electric motor shown in Fig. 1.C1. To investigate the impact this has on the electric motor design, a sizing analysis was conducted as a function of design rotational speed with constraints imposed to ensure that the electric machine's rotor can accommodate the hydraulic pump. Scaling rules for the required diameter of a hydraulic pump

(for a specific required flow) were developed for the gerotor and radial ball piston architectures. Results shown in Fig. C2 indicate that for the given design specification (Table 1.C2), the electric machine must have at least 4 poles.

Table 1.C2: Parameters used for scaling study

Parameter	Power	Speed	Magnet Material	Steel lamination	Air Gap Flux Density
Rating	20kW	15000 RPM	Arnold Recoma 35E	Arnon-7	0.8T

The sizing analysis further reveals that the overall size of the electric machine is large compared to the hydraulic pump. Attempts to reduce the size have resulted in two new topologies based on axial flux electric machines which significantly reduce the overall machine size. From a sizing perspective, the moment of inertia of the rotating mass is the critical quantity to compare when evaluating a machine topology, as this determines the transient response of the overall system. Results in Fig. 1.C3 indicate that the axial flux machine topologies yield the lowest moment of inertia. The superiority of the axial flux topology also dictated the use of the radial ball piston architecture, because it naturally integrates and scales with the axial flux motor.

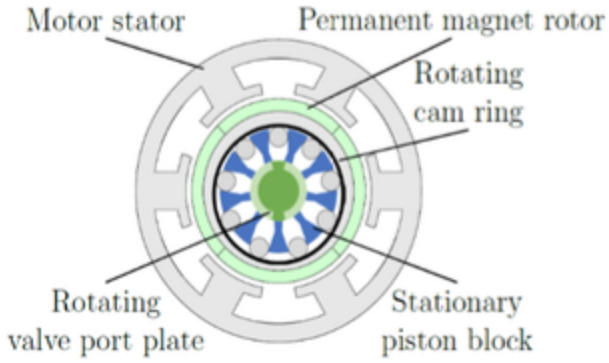

Fig. 1.C1: Integrated Motor-Pump schematic.

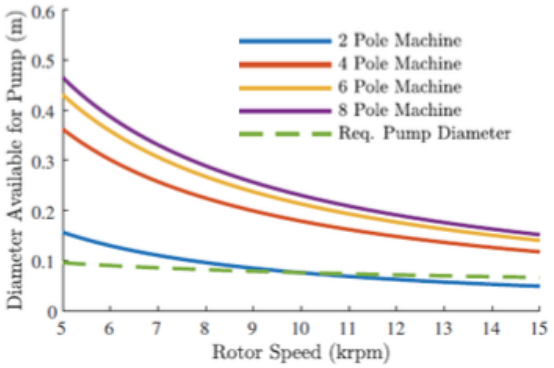

Fig. 1.C2: Max. available space for hydraulic pump

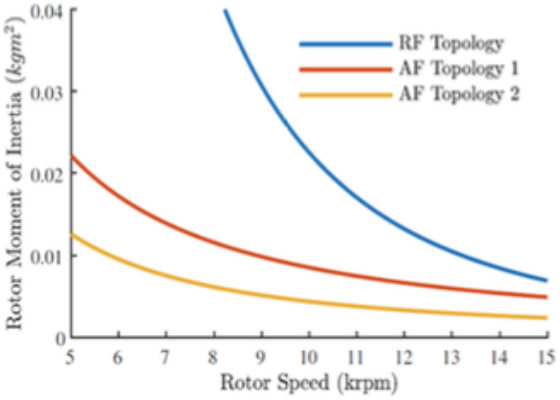

Fig. 1.C3. Rotor moment of inertia comparison

Subtask 1.C1-3: Electric Machine Modeling and Design

Radial flux topology: Analytic dimension equations and electromagnetic Finite Element Analysis (FEA) models have been developed for the radial flux electric machine of Fig. 1.C1 and linked to an optimization algorithm. A preliminary multi-objective optimization was performed to maximize efficiency and torque per rotor volume (TRV) while minimizing torque ripple. The machine was considered to have a bore in the rotor, with a diameter required to accommodate the hydraulic pump at 15000 RPM. Fig. 1.C4 shows a Pareto plot of the performance metrics and the geometry for globally optimal design is shown in Fig. 1.C5.

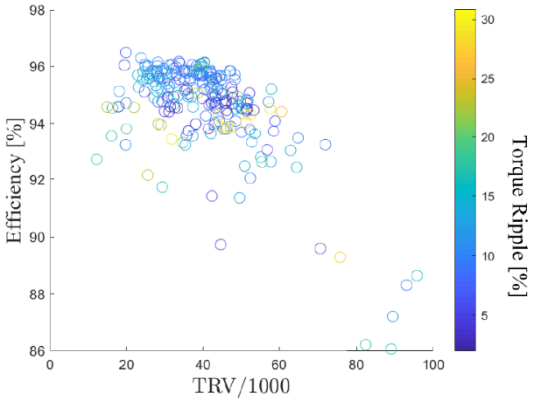

Fig. 1.C4: Performance of candidate designs.

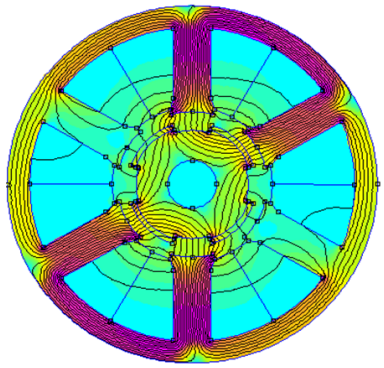

Fig. 1.C5: Optimal Geometry

Axial flux motor: The novel axial flux machine topologies also require 3D FEA for accurate modeling. Detailed FEA models are developed for the topology using *MagNet* by Mentor Infolytica. Designs with an iron core and without an iron core have been considered.

For the coreless machines, designs considered have a coreless stator winding and two permanent magnet rotors. Coreless stator tends to improve efficiency (by eliminating stator iron loss) and reduce torque ripple. Because 3D models are computationally intensive, an equivalent 2D model was developed for the axial flux machine and linked to a Multi-Objective Genetic Algorithm for optimization. The

objectives of the optimization were to maximize efficiency, minimize cost [$/kW], and reduce torque ripple. Fig. 1.C6 shows the 2D equivalent model and the optimization results are shown in Fig. 1.C7. Results from preliminary optimization with 50 individuals and 50 generations indicate candidate designs with efficiencies close to 97% and a cost well below $20/kW. Note that this efficiency and cost tradeoff is based on the electric machine alone. The costs are calculated from estimates of the raw material cost of the electric machine active materials.

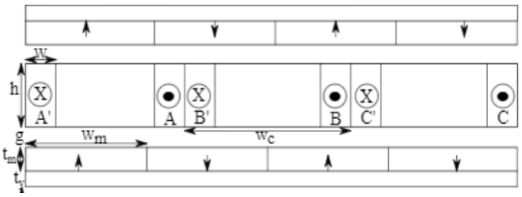

Fig. 1.C6: 2D equivalent model.

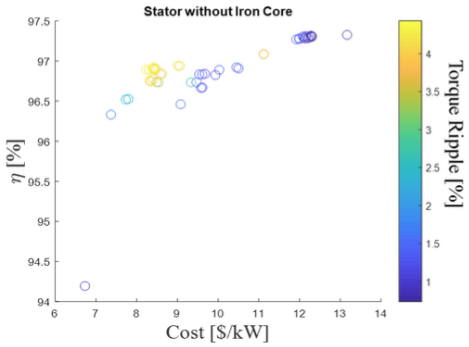

Fig. 1.C7: Optimization results for AF_PMSM

Fig. 1.C8 (left) shows the Pareto optimal front for efficiency, power density, and cost for the coreless stator machine. It is evident that the motor can reach a gravimetric power density of up to 10.5 kW/kg. However, this comes at the expense of reduced efficiency. So, there needs to be a balance between the two objectives. A detailed FEA analysis was conducted on a particular design using a current density of J=20A/mm^2 which has a 92.6% efficiency and power density of 9.78kW/kg. It was found that stator coil loss is the dominant loss.

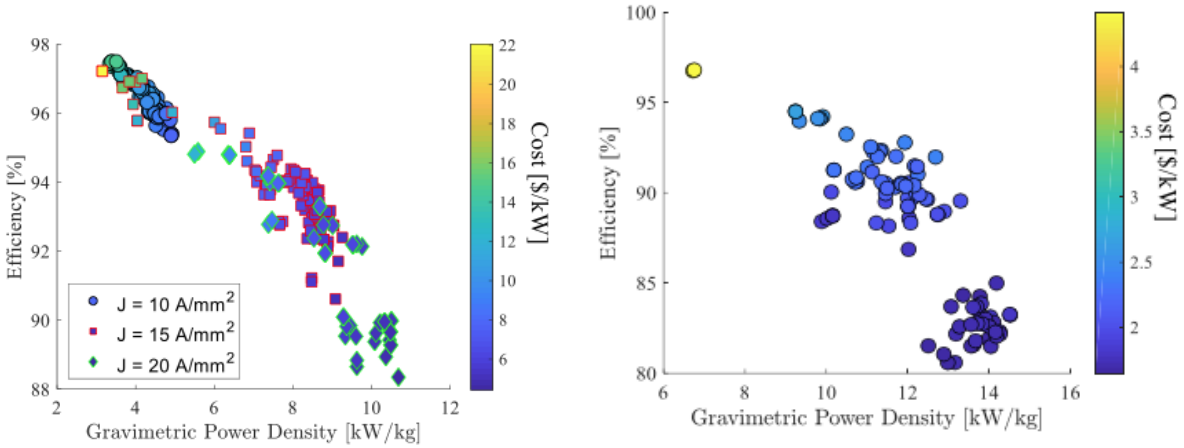

Fig. 1.C8: Gravimetric power density versus efficiency and cost for different current densities for coreless design (left) and iron cored design (right).

Axial flux motor designs with iron core were also considered. An advantage of iron-cored machines is lower material cost as they require less permanent magnet to maintain the same air gap flux density. This also leads to lower rotor mass, smaller moment of inertia, faster response time, and improved gravimetric power density, at the cost of greater losses and lower efficiency. Since high-grade steel and fabrication of specialized stator laminations are needed, fabrication cost may also increase.

During the analysis phase, only 8 pole designs with 6 and 12 slots were explored. It was observed that 12 slot designs outperformed the 6 slot designs. Other slot-pole combinations may yield further improved designs and will be investigated.

Fig. 1.C8 (right) shows that the optimized iron-cored motors can also have high efficiency and power density. For example, it is possible to achieve efficiency of 91.85% for a 20kW motor that weighs 1.65kg. The topology of the optimized axial flux machine is shown in Fig. 1C9.

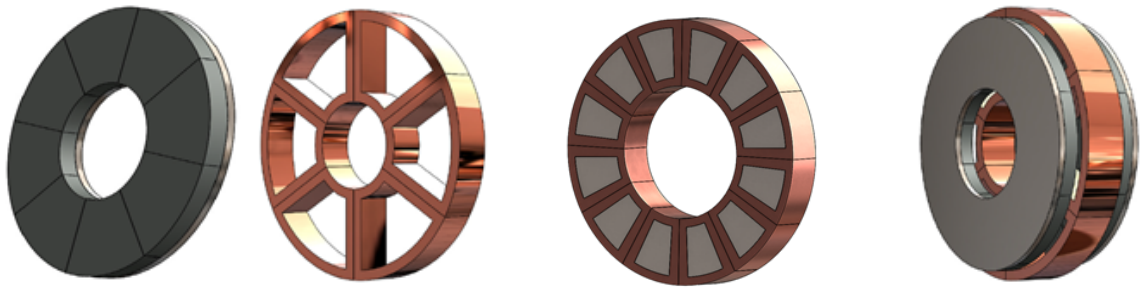

Fig. 1C.9: Optimized Axial Flux Machine topology: a) rotor; b) stator; c) combined rotor and stator

Linear machine: Previously developed linear electric machine models have been extended to this study and used to explore the design space. The linear machine chosen, shown in Fig. 1.C10, inherently features a high gravimetric power density relative to other linear machines. The stator consists of an E-shaped iron core and the mover has a hollow iron with the Halbach array mounted on it. The machine was optimized for efficiency, power density, and cost. The Pareto plot is shown in Fig. 1.C11 for the electric machine alone. The cost values again reflect the raw material cost of the electric machine materials alone. Optimization results suggest that motor designs with a smaller bore-to-stroke ratio and a higher oscillation frequency can give better performance. Although efficiency can be very high, the gravimetric power density values obtained are low (max is 1.1kW/kg). Thus, linear electric machines will not be able to meet the power-density requirement of this project. Hence, the linear machine topology will not be pursued further.

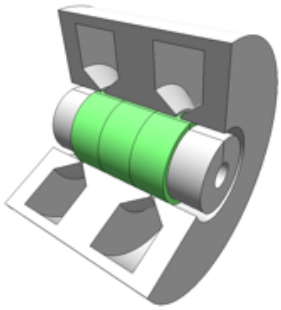

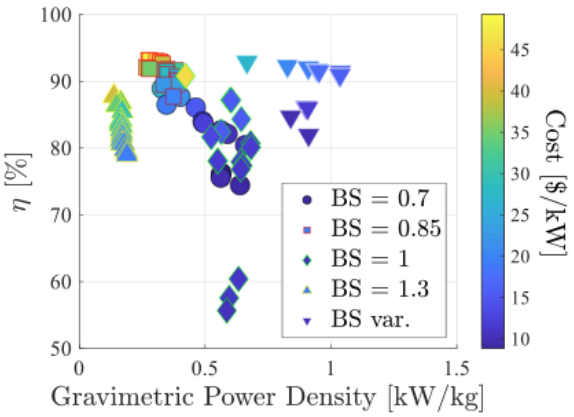

Figure 1.C10: Linear Electric Machine

Figure 1.C11: Optimization Results for Linear Electric Machine for f=132Hz & different bore-to-stroke (BS) ratios.

Subtask 1.C1-4: Hydraulic machine modeling and design

Radial Ball Piston Architecture: A radial ball piston pump, Fig. 1.C12, uses rolling balls as pistons to reduce friction between the cam and the piston. It also creates a more power-dense design when compared to a standard piston with a roller attached. The axial-flux motor / radial ball piston pump topology would have a stationary cam and pintle, with the electric motor spinning the cylinder block. The eccentricity of the cylinder block and cam then causes the ball pistons to reciprocate.

A Matlab model of the pump has been developed to estimate the efficiency of different pump designs. The pressure dynamics within the cylinder are modeled to accurately calculate the output flow of the pump. The leakage and shear at the ball piston–cylinder interface are modeled, as are the leakage and the shear between the pintle and the cylinder block.

The calculated efficiency is then used as the optimization parameter in a single objective genetic algorithm. Table 1.C3 shows the results of optimizing three differently sized radial piston pumps. Each optimization used 100 individuals and 225 generations. In this study, the hydraulic pump was optimized at the rated speed of 15000RPM. The optimized pump has a mass of 1.02kg and an efficiency of 94.16%.

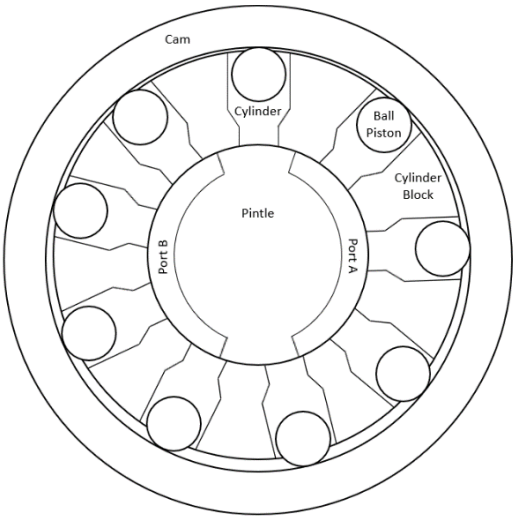

Fig. 1.C12: Radial ball piston pump/motor.

Table 1.C3: Optimization results for hydraulic pump/motor.

Max speed:	5000 RPM	10000 RPM	15000 RPM
Efficiency:	97.00%	95.38%	94.16%

Subtask 1.C1-5: Integrated Hydraulic-Electric Model and power electronics

An electric motor model was developed in the Matlab-Simulink environment based on lookup tables obtained from finite element analysis of the designed axial flux motor. This model was interfaced with the model for the hydraulic pump designed by the collaborating mechanical engineering team. Control was designed for the integrated system with an inner current control loop and an outer speed control loop. Simulation shows adequate control performance.

The terminal voltage for the motor is assumed to be 3-phase, 480 V (l-l). Analytic sizing equations for power electronics have been compiled from the literature. These equations are used in conjunction with the electric machine parameters determined for the optimal machine design (i.e., back-EMF, electrical frequency, etc.).

To estimate the efficiency and power density of the power electronics, an output power of 20kW is assumed. The efficiency of the power electronics is estimated at steady state operating conditions using the PLECS blockset in Matlab Simulink. The motor model obtained from FEA is fed by a 3 phase Voltage Source Inverter (VSI). The fundamental frequency is 1kHz. Space Vector Modulation is employed, with a switching frequency of 21kHz. A suitable SiC MOSFET C2M0025120D from Cree-Wolfspeed is selected. The total loss in the power electronic devices, DC bus capacitor, gate resistor, and various other supporting circuit components is estimated to be about 250 W, resulting in an efficiency of 98.75%. 90% of the losses are conduction losses and the remaining 10% are switching losses.

The mass of the power electronics is estimated using datasheet values for the mass of the power electronic switches and the DC bus capacitor. The total mass, including the DC bus capacitor, power semiconductor devices, sensors, PCB, cooling plate, and other auxiliary components, is estimated to be 0.88 kg. This gives a power density of 22.72kW/kg which is reasonably close to commercial SiC EV inverters in the literature.

Subtask 1.C1-6: Evaluate Linear/Rotary Topologies

Analysis indicates that the rotary machine is the most cost-effective and energy-efficient option. The linear machine potentially has a more desirable form factor, but its low power density makes it less appealing at the selected power range. Of the rotary machines considered, the Axial Flux Permanent Magnet Synchronous Motor (AF-PMSM) topology appears to be the most compelling for this application.

This task is complete and with the choice of combining an axial flux permanent magnet synchronous machine (AF-PMSM) and a radial ball piston pump/motor as the integration topology.

Milestone 1.4 ‘Select integration topology’ is accomplished.

BP-1 Go/No-Go Performance Metric Demonstration

The criteria for the BP1 Go/No-Go decision consist of 3 feasibility demonstrations:

1) At least 1 platform with the potential of reaching 65% efficiency or 40% energy saving;
2) HECM control strategy verified in simulation
3) Integration topology has a gravimetric power density greater than 5kW/kg and a conversion efficiency greater than 85%.

Criteria 1: At least 1 platform with the potential of reaching 65% efficiency or 40% energy saving

As described earlier under task 1A.3, energy saving analysis has been conducted on 3 platforms: a

wheel-loader, a 5-ton mini-excavator, and a 22-ton excavator. For each of these platforms, energy consumption and system efficiency of the baseline load-sensing system were obtained for various drive cycles. Energy consumption when the platforms were operated using the proposed hybrid hydraulic-electric architecture (HHEA) for the same drive cycles was also obtained. In each of these cases, the baseline load sensing system has an efficiency (defined as the positive output work / engine mechanical work) between 20-47%. The efficiencies of the machines using the HHEA are 85-121% except for one drive cycle (mini-excavator grading which has an efficiency of 65%). In each case, the efficiency improvement is over 3 times or at least 66% of energy saving. Hence, this energy saving criterion has been satisfied for 3 platforms.

Criteria 2: HECM control strategy verified in simulation

As described earlier under tasks 1B.2 and 1B.3, the passivity-based backstepping control strategy, assuming that electric motor torque is input, has been shown in analysis and simulation to be effective for tracking the desired actuator trajectory in between rail switching events. In addition, a mitigation strategy has been developed to reduce the harmful effect of rail switching by i) reducing the frequency of rail switching, and ii) using a “transition” control. Therefore, the control strategy criterion has also been met.

Criteria 3: Integration topology has gravimetric power density and conversion efficiency exceeding 5kW/kg and 85%

To estimate the overall efficiency and power density, a 20kW integrated electric-hydraulic conversion machine is assumed. As described earlier under task 1C.1, for this power rating, a radial ball piston pump/motor designed for 15000 rpm has an efficiency of 94.16% and weighs 1.01kg. Also, power electronics have an efficiency of 98.75% and weigh 0.88kg. Both coreless design and iron-cored motor design are considered for the electric motor.

A coreless stator rotary axial flux electric motor has an efficiency of 92.75% and weighs 2.044kg. This leads to a total mass of (1.02+ 0.88 + 2.044)kg=3.944kg so that the power density is 5.07 kW/kg. The total efficiency is: 0.9416 x 0.9875 x 0.9275 = 86.6%.

An iron-cored rotary electric machine has an efficiency of 91.85% and weighs 1.65kg. This leads to a total mass of (1.02+ 0.88 + 1.65)kg=3.55kg so that the power density is 5.63 kW/kg. The total efficiency is: 0.9416 x 0.9875 x 0.9195 = 85.4%.

Thus, either an iron-cored or a coreless option can meet the target efficiency and power density target.

2. Budget Period 2 (BP-2) Technical Progress

Budget Period 2 spans the 15th-28th months (14 months) of the project, from November 1, 2019 to December 31, 2020. The main focus of this budget period is on the preliminary validation of our proposed approach: a) the proposed hybrid hydraulic-electric architecture (HHEA) can provide at least 65% efficiency (from engine output to positive work) or 40% energy savings compared with a baseline system; b) a control strategy suitable for the HHEA is available to provide the desired control performance; c) the topology for the integrated electric-hydraulic conversion machine (i.e. an electric motor and hydraulic pump/motor combination) to be used in the hydraulic-electric control module (HECM) in the HHEA has the desired efficiency of 85% and the gravimetric power density of 5kW/kg.

Building upon the energy-saving study in BP1, thrust A conducted studies to understand the tradeoffs between different design options and objectives, and performed high-fidelity simulations to verify the energy-saving potential of the proposed architecture. In thrust B, the focus is on refining the control strategy and constructing and conducting control experiments on a hardware-in-the-loop experimental testbed. Within thrust C, the electrical and hydraulic subsystem models were validated and explored in order to create a power-dense and efficient integrated electric motor - hydraulic pump prototype.

2.1 Thrust A - Energy Saving

Task 2.A1 – Pareto optimal trade-off analysis

In order to determine the Pareto optimal designs for various objectives, the energy-saving analysis tool is used iteratively for various design choices. As it turned out, all the metrics of interest, other than energy consumption, are direct metrics of the design choices that do not depend on simulations or the effect of control. In particular, we found that the number of common pressure rails is a surrogate of the system complexity, and the HECM electric motor torque requirement is a major component of cost. Because of this, we are able to evaluate the complexity and electric component size metric independently of the energy consumption evaluation (which requires the application of the optimal control algorithm). This makes the Pareto optimal analysis much more straightforward and a grid search approach where the merits are evaluated seems more appropriate.

As an example of the Pareto optimal study, we compared the tradeoff between the number of pressure rails, torque requirement of the electric motor, and energy efficiency for the CNH wheel loader. The study was conducted by evaluating the energy efficiency of the HHEA design with different pressure rails, and with electric motor torque being unconstrained or constrained to be at the minimal requirement dictated by the drive cycle.

Table 2.A1: Pareto tradeoff between electric motor torque capability and efficiency for HHEA applied to a wheel loader. LT torq and TT torq are the torques requirement for the lift and tilt actuators. Here. efficiency is the ratio between positive work and input energy.

	2 CPRs	3CPRs	4CPRs	5CPRs
Unrestricted torque capability	Eff: 69% LT Torq: 712 Nm TT Torq: 782 Nm	Eff: 92% LT Torq: 232 Nm TT Torq: 284 Nm	Eff: 102% LT Torq: 192 Nm TT Torq: 175 Nm	Eff: 104% LT Torq: 155 Nm TT Torq: 143 Nm

The result of this Pareto tradeoff pilot study shows that there is very little advantage of not choosing the smallest feasible electric motor for the given number of pressure rails as the efficiency gain by having larger electric motors are in the other of but increasing the number of pressure rails significantly reduces the required motor size and marginally increases efficiency. Once cost can be assigned to electric component size and number of pressure rails, the overall cost and the payback period can be obtained to determine the optimal choice of the number of pressure rails and the corresponding required motor size.

Milestone 2.1: Pareto optimal analysis tool **is complete** with the completion of task 2.A1 and the demonstration of the Pareto optimal analysis tool in analyzing a pilot set of tradeoffs.

Upon demonstrating that the energy-saving analysis can be used in an iterative manner to obtain Pareto optimal trade-off between different objectives, various trade-off studies have been performed.

1. Sensitivity of energy saving to hydraulic-electric control module (HECM) component efficiency: A study was conducted in which losses in the HECM (i.e. the electric motor and pump/motor) are systematically increased and decreased, and their effects on the overall energy consumption was evaluated. The results are shown in Fig. 2.A1. It was found that overall energy consumption is relatively insensitive to HECM component efficiency. For example, HECM component efficiencies of 100%, 50%, and 25% yield system efficiencies (defined as positive output work/energy input) of 1.25, 1.1, and 0.95 respectively. This indicates that even with modest HECM efficiencies (50%), the architecture provides significant (60%) energy savings.

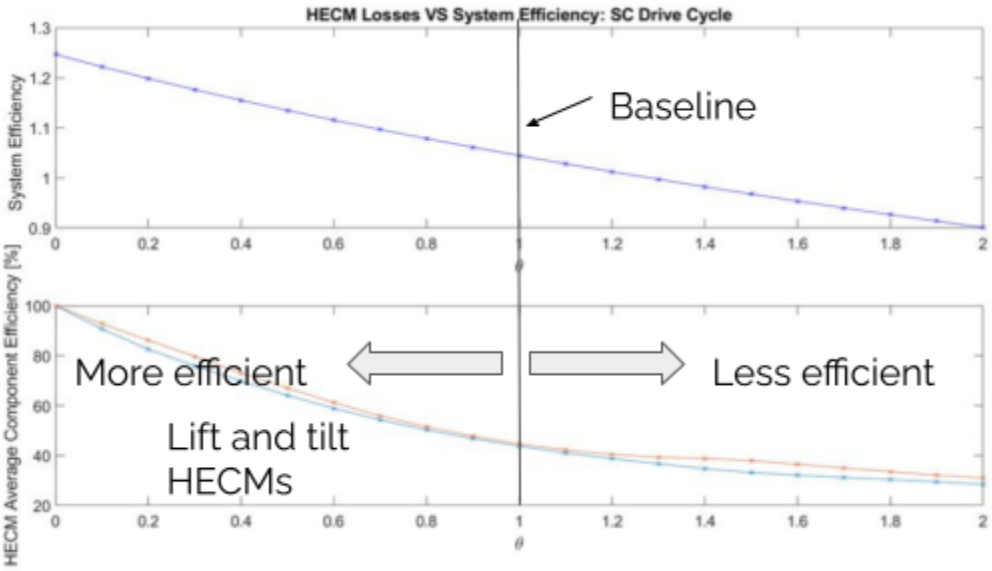

Fig. 2.A1: Top: overall efficiency versus HECM loss factor. Bottom: HECM efficiency versus loss factor. Loss factor of 1 is the nominal case, loss factor of 2 means that losses are doubled, and loss factor of 0.5 means that losses are halved.

2. Detailed versus simplified efficiency maps of electric motors and hydraulic pump/motor maps: the overall system efficiencies were evaluated with analytically derived efficiency maps and experimentally evaluated maps. For example, Fig. 2.A2 and Tab 2.A3 show a 90% efficient electric motor map versus a detailed PLECS-based map and their impact on overall energy consumption. Switching the electrical map has no impact on the overall efficiency in this case. Similarly, when the pump/motor map is replaced from one for a bent-axis to one from an axial-piston unit, the efficiency is changed by about 2%. These results are consistent with the previous result that the overall energy efficiency is relatively insensitive to the HECM efficiencies, the specific maps of the electric motors and of the hydraulic pump/motors.

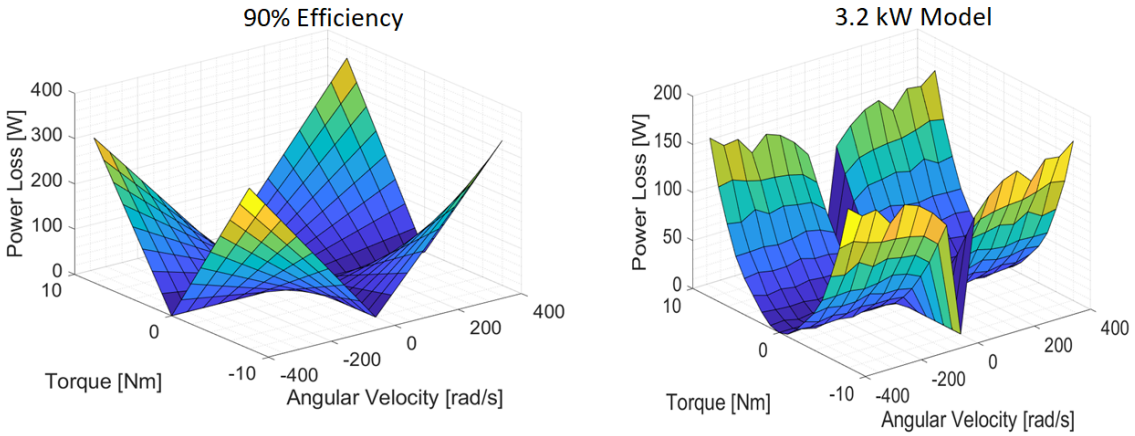

Figure 2.A.2. Loss maps for the old (flat 90%) and new (detailed) models for the electric machines/drives.

Table 2.A2. Wheel-loader efficiencies assuming old and new electric motor/generator maps.

SC Drive Cycle		
Electrical Losses	90% Efficiency	Manikanta Pallantla 3.2 kW Map
System Efficiency [%]	104 %	104 %
HECM Hydraulic Efficiency [%]	Lift: 43.5 % Tilt: 45.0 %	Lift: 42.7 % Tilt: 43.4 %
HECM Electrical Losses [kJ]	169 kJ	138 kJ

LC Drive Cycle		
Electrical Losses	90% Efficiency	Manikanta Pallantla 3.2 kW Map
System Efficiency [%]	116 %	116 %
HECM Hydraulic Efficiency [%]	Lift: 46.9 % Tilt: 46.7 %	Lift: 42.7 % Tilt: 43.4 %
HECM Electrical Losses [kJ]	131 kJ	132 kJ

3. Tradeoff study of energy saving, number of pressure rails and electric component sizes for 3 machines (5 ton excavator, 22 ton excavator, and 20-ton wheel-loader): All three machines show very similar trends. With the proposed HHEA, energy consumption is relatively insensitive to the number of common pressure rails. With 3, 4, and 5 pressure rails, energy savings of 50-80% compared to the baseline load-sensing architecture are achieved for the different machines and drive cycles. The main effect of increasing the number of common pressure rails is the reduction in electric motor size. For the 5-ton excavator, 3 CPRs is a reasonable design, whereas for the 20-ton wheel loader and 22-ton excavator, 4-5 CPRs are more appropriate with the electrical motor size being only 6-20% that of an alternate Electro-hydraulic actuation (EHA) architecture See Figs. 2.A3a and 2.A3b for a sample of the results for a 22-ton excavator and a 5-ton excavator.
4. Comparison between HHEA and STEAM: The HHEA is compared with a common pressure rail architecture in the literature that uses throttling (an architecture known as STEAM [3]) instead of our throttle-less HECM. The STEAM architecture (Fig. 2.A4) was developed by the Institute for Fluid Power Drives and Controls at Aachen University, Germany. It is interesting to compare HHEA with STEAM because both utilize common pressure rails that are fed by a common main pump. The difference lies in how the hydraulic power is modulated to meet the demands of each actuator. The HHEA modulates the hydraulic power by bucking or boosting the power using a hydraulic electric control module (HECM) that combines hydraulic and electric power. In contrast, the STEAM architecture modulates the hydraulic energy using proportional throttling valves. By avoiding throttling valves the HHEA will be more efficient than STEAM but at the expense of added complexity of each of the Hydraulic-Electric Control Modules (HECMs). It is, therefore, useful to quantify by how much the HHEA is more efficient than STEAM.

   The comparison results are shown in Fig. 2.A3a and 2.A3b. For 3 CPRs, HHEA saves 62-70% of input energy compared to load-sensing baseline, and STEAM saves 34-43%. For 5 CPRs, HHEA saves 69-81% over load-sensing whereas STEAM saves 60-69%. It was found that the HHEA uses ~30% less energy than STEAM. The benefit is reduced as the number of common pressure rails increases. For details of this comparison see [8]. These results show the tradeoff between complexity and energy saving. Users can choose which actuator to add a HECM and which to use only throttling according to their cost budget.

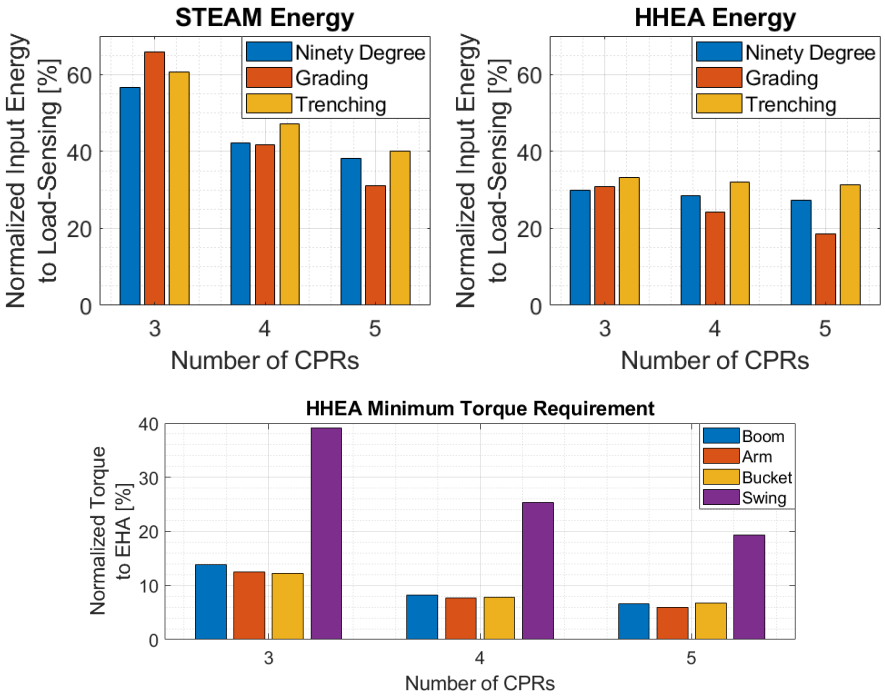

Fig. 2.A3-a: Trade-off studies for a 22-ton excavator comparing HHEA with STEAM for different numbers of common pressure rails.

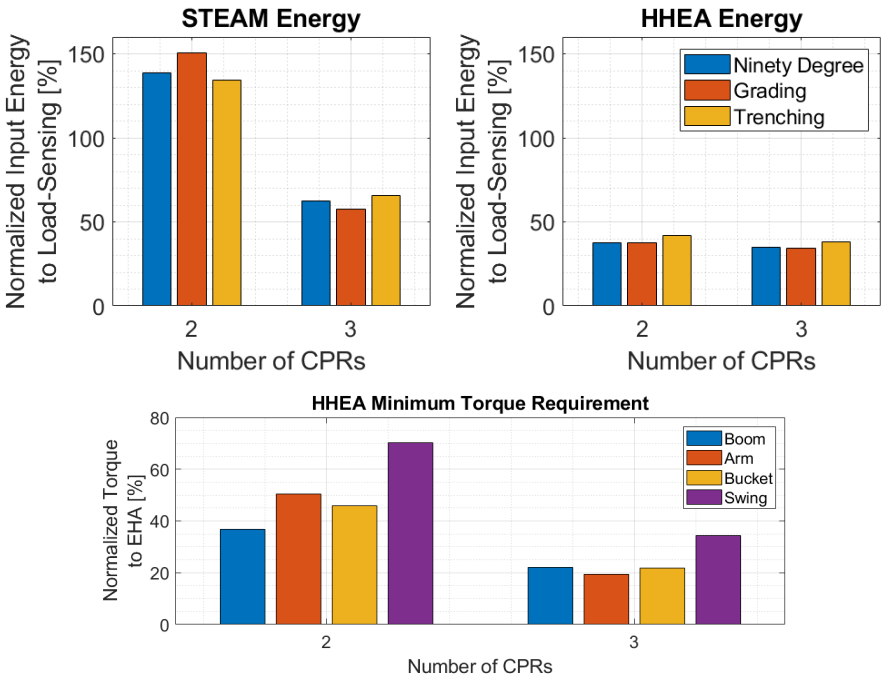

Fig. 2.A3-b: Trade-off studies for a 5-ton excavator comparing HHEA with STEAM for different numbers of common pressure rails.

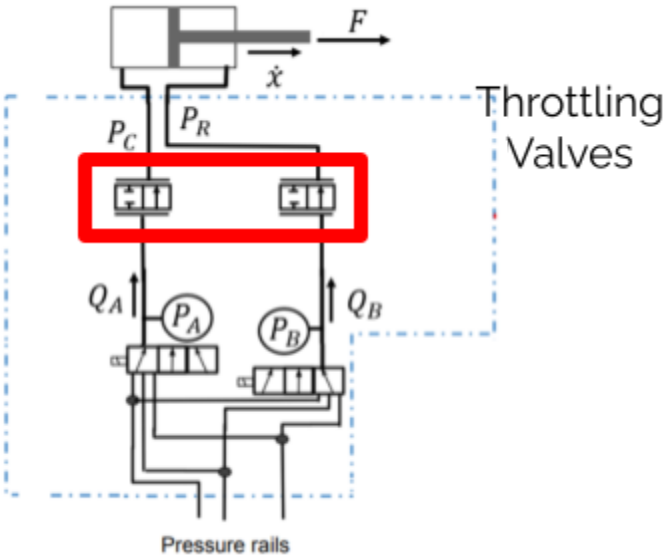

Fig. 2.A4: Schematic of the STEAM architecture that uses multiple common pressure rails and throttling valves for modulation.

5. Fully electrified 5-ton excavator study: A control co-design methodology was applied for the design of a 5-ton excavator that is powered exclusively using an electric battery instead of an internal combustion engine (ICE). Two architectures were studied, one in which the ICE is simply replaced by an electric motor powered by the electric battery; and the second, revealed through systematic optimization, is less complex and does not require the main pump. The energy consumption and electric motor torque requirements for the first fully electrified architecture are shown in FIg. 2.A5.

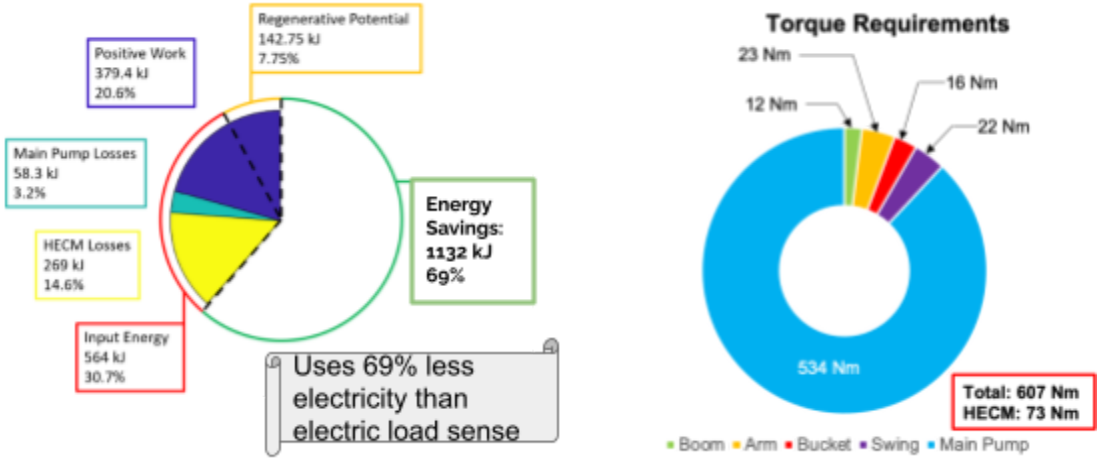

Fig. 2.A5: Energy consumption and torque requirements in which the HHEA utilizes an electric motor to drive a main-pump for filling the common pressure rails

This architecture is quite energy efficient, saving 69% compared with a battery-powered load-sensing system. The electric motor sizes for the individual actuators are also small (even compared to an ICE-driven HHEA system) but it requires a prime mover electric motor capable

of high torque to power the main pump for the common pressure rails. Increasing the number of CPRs leads to a significant reduction in the torque requirements and sizes of electric components of the electric motors for the individual actuators but not for the prime mover. The ICE HHEA requires slightly (2-5%) less engine output work than the electric battery energy for the fully electrified version in most cases.

The second fully electrified architecture emerged when optimizing the first architecture as the torque limitations for the electric motors in the HECMs are made less restrictive. This is illustrated in Fig. 2A.6. Since the operating mode of this architecture requires no net rail flow, the main pump can be completely eliminated. The new architecture is even more efficient than the first architecture, saving 71% energy compared to an electric load-sensing system. The torque requirements of the electric motors for the individual actuators are larger (106 Nm vs 73Nm) but since it does not require the main pump and the electric motor for driving it, the overall complexity is lower despite the electric motor in each HECM being slightly larger.

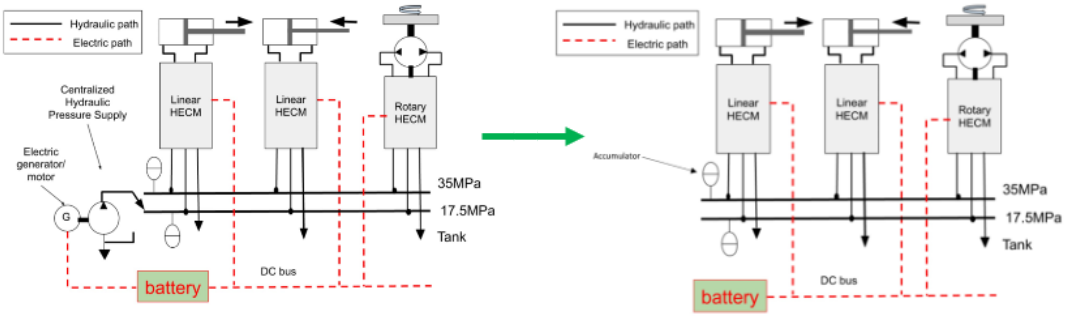

Fig. 2A.6: Evolution for a fully-electrified system architecture: from one with a prime-mover e-motor and one e-motor/h-pump for each degree-of-freedom to one with no prime-mover.

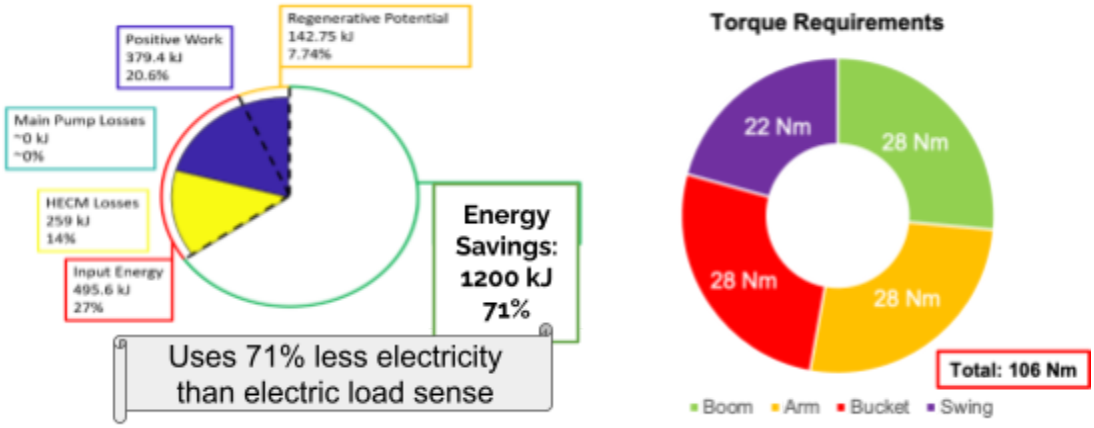

Fig. 2A.7: Energy consumption and torque requirements of a co-designed fully-electric powered system without a prime-mover electric motor and pump.

6. Price/cost models for key components of the HHEA: In order to perform Pareto trade-off analysis with system cost as one of the objectives, cost models for key constituent hydraulic and electrical components of the HHEA have been developed. For each component, the listed sale prices of the product for a selected operating range from publicly available market information were obtained.

The products selected in this analysis would present a balance between price and performance. The price here represents competitive market volume pricing for each component. The performance considers the maturity and robustness of each performance metric of the product. Taking efficiency as an example, the products would either have state-of-the-art efficiency or project a good near-term future efficiency. This way, high-end low volume products, which have supreme performance but very high cost, would still be considered as candidates. After collecting the raw data, curve fitting was applied to develop a semi-empirical model of price as a function of selected sizes or dimensions. The product sizes or dimensions can then be used as variables in Pareto optimizations.

Fixed displacement pump/motors are taken as an example to illustrate the process. A 4-quadrant fixed displacement pump/motor is needed in the HECM. Given the same maximum operating pressure and normal operating temperature, the pump/motor size can be selected by its displacement (in cc per revolution). A displacement range of 5cc to 180cc is predefined. Collecting product information from two representative suppliers in the industry, a sale price versus displacement curve was compiled. A least square curve was fitted to the raw data, and a semi-empirical equation was derived to model the price ($) as a function of the displacement (cc), as shown in Figure 2.A8. The same technique has also been applied to solenoid valves, electrical motors, motor drives, and batteries. Note however, that the list price is generally much higher than what an OEM pays so reasonable discount factors are likely necessary before the price models can be used in the Pareto study.

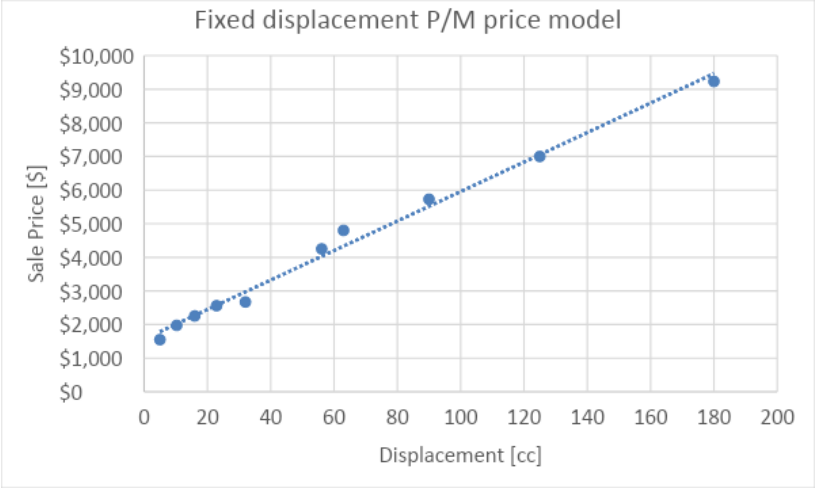

Figure 2.A8: Fixed displacement P/M price model

In addition to these tradeoff studies, the energy optimization algorithm has been updated both theoretically and practically to cope with certain situations (such as in STEAM and for single rotary degree-of-freedom) where our previous Lagrange multiplier algorithm cannot satisfy the constraint functions. This issue is found to be due to decisions at a large number of time points switching in response to an infinitesimal change in the Lagrange multiplier. This problem is solved simply by adding a small amount of random noise in the cost evaluation. It was also found that determining the decision variables by optimizing each individual actuator separately is only slightly suboptimal compared to

optimizing all actuators together. This finding is important for improving computation efficiency for machines with a large number of actuators and is especially usual for real-time control. For details of this topic, see [5].

In all the trade-off studies, energy savings of 50-80% compared to the baseline load-sensing architecture have been established for all three example machines (5-ton and 22-ton excavator, and 20-ton wheel-loader). This level of energy saving exceeds comfortably the criteria for this BP's Go/No-Go decision.

Task 2.A2 – Verify optimal design solutions via high fidelity simulations

This task involves (1) creating high fidelity platform models, (2) establishing a simulation environment, (3) performing simulations to obtain energy consumption for the baseline system and the optimized HHEA design. The goal is to verify that HHEA can provide the desired 65% efficiency or 40% energy saving with high fidelity system models.

Creating high fidelity platform models

A high fidelity model of the baseline (load sensing) work circuit for the CNH wheel loader has been developed using AMESIM. Actual duty cycles of the wheel loader collected through experiments including the operator joystick commands, actuators displacements and actuator loads are used as test vectors to calibrate and validate the model. Once validated, the high-fidelity model is used to perform simulations to obtain baseline energy consumption.

The key components to drive each hydraulic actuator includes several modules: an electric motor generator with its drive, a hydraulic pump motor with its efficiency map, a control valve, and a hydraulic linear actuator. Models of these modules were developed in AIMSIM. The first module including the electric motor with its drive is shown in Fig. 2.A9. A permanent magnet synchronized AC (PMAC) motor was modeled in AMESim. A hierarchical control of three layers was included in the motor drive. The outer layer was a motor speed control loop. The output of the speed feedback loop was the commanded torque. The middle layer was the motor torque tracking loop, with the target torque calculated from the outer speed control loop. The inner loop was the vector control loop to control the motor current so that the target torque defined in the middle layer can be tracked. The motor and drive behavior that was not included in this model was the thermal effect. To account for the thermal effect, an FEA model can be further integrated. A simplified compensation is to associate an efficiency map in the form of a look up table with this model.

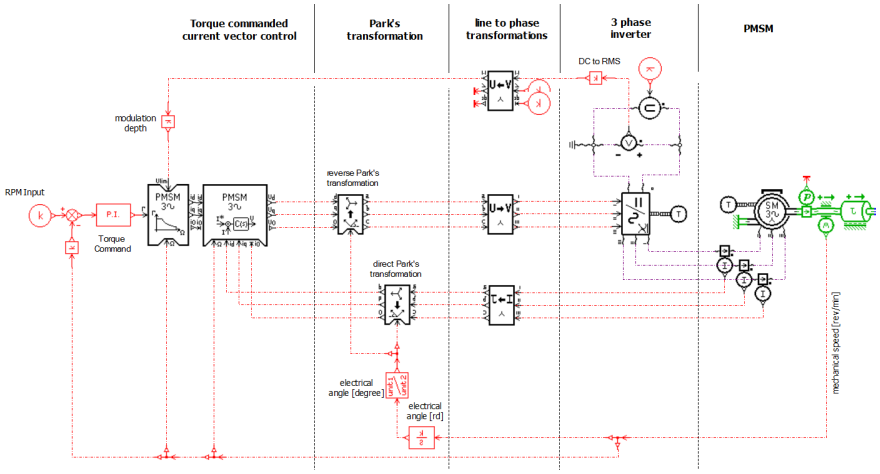

Figure 2.A9: model of a PMAC motor with its drive in AMESim

The second module developed was a hydraulic 4 quadrant variable displacement pump/motor. The volumetric efficiency and the mechanical efficiency were implemented as a multiplier to the theoretical flow and the theoretical torque at different P/M displacements and speeds. An additive loss map was also developed to quantify the power loss at different operating regions. Examples of the loss map with respect to the load pressure and shaft speed at different displacements are shown in Fig. 2.A10.

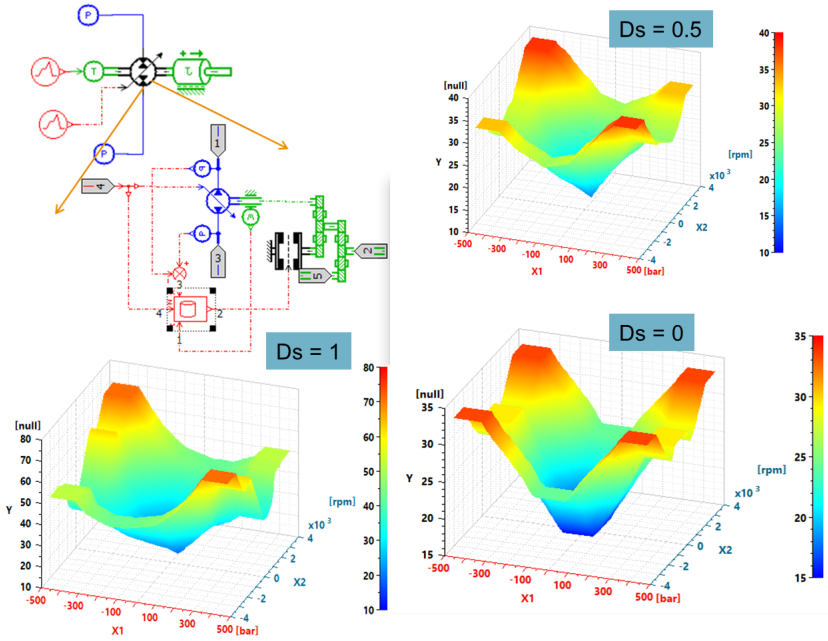

Figure 2.A10: AMESIm model of a hydraulic 4 quadrant variable displacement pump/motor with its selected loss map as a function of load and shaft speed at different displacements

The third module modeled was an electro-hydraulic proportional valve. The valve opening area for each flow path was modeled as a lookup table, with the input being the normalized valve input, and the output being the fractional area. The maximum valve opening area for each flow path was defined as a characteristic flow rate at a corresponding pressure drop. The dynamics of the valve spool motion was

modeled as a second order linear time invariant (LTI) system, characterized by the natural frequency and the damping ratio. By default, an under-damped system was assumed.

The last module was a hydraulic linear actuator. The model includes two parts: the mass and the hydraulic cylinder. Both orientation and mechanical friction properties are specified in the mass parameter list. The hydraulic properties such as leakage, dead volume, and the frictions associated with the cylinder can be defined in the cylinder's parameters. The module in AMESIm also includes a hard stop at the ends of the stroke.

These hi fidelity modules are integrated in the HHEA and the excavator model in AMESim in order to validate the energy saving potential of HHEA. As baseline models, two popular architectures: a load-sensing system and s a negative flow control (NFC) system architecture have been modeled.

Establishing a simulation environment

To establish the simulation environment and create high fidelity simulation models, a co-simulation capability and a software-in-the loop (SIL) capability are first developed. This capability allows efficient and systematic development of control strategies for complex systems. These two capabilities enable efficient and systematic development of the control strategies. Firstly, rapid validation of the control strategies can be implemented in a high-fidelity plant model simulation before being implemented on the actual hardware. Secondly, the performance and robustness of the control strategies can be validated with different test vectors and scenarios for refinements. Finally, hardware design and controller issues that can arise from a complex system can be identified early and addressed quickly before the hardware build.

Co-Simulation means, running a software that simulates the virtual dynamic model of the physical system simultaneously with another software that simulates the test vectors and control actions on the physical system, on a single computer as shown in Fig. 2.A11.

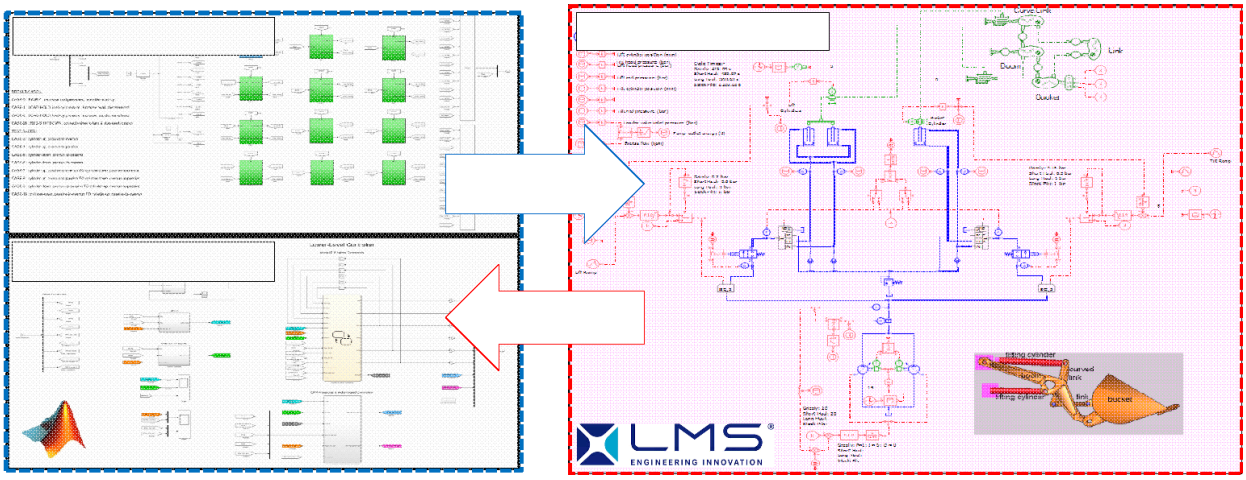

Figure 2.A11: Co-Simulation architecture

Here, LMS AMEsim™ is used to simulate the multi-domain (mechanical, electrical, fluids and thermal) physical system, and MATLAB Simulink® is used to simulate the controller. A co-simulation block is

used on both software's to facilitate the inputs and outputs between the plant model in LMS AMEsim™ and the controller in MATLAB Simulink®.

Software in the Loop (SIL) refers to an environment in which the virtual plant model developed in LMS AMEsim™ is loaded into a dSPACE™ Midsize Simulator while the test vector and hardware controller developed in MATLAB Simulink® are loaded into a dSPACE™ MicroAutoBox Controller. Both the simulator and controller will then execute the plant model and control strategies in real-time, where the communication between them are facilitated through CAN communication (Fig. 2.A12). The purpose of implementing both the virtual plant model and controller in dSPACE™ hardware's is to test the robustness and performance of the control strategies in a hardware controller in real-time using actual CAN network communication.

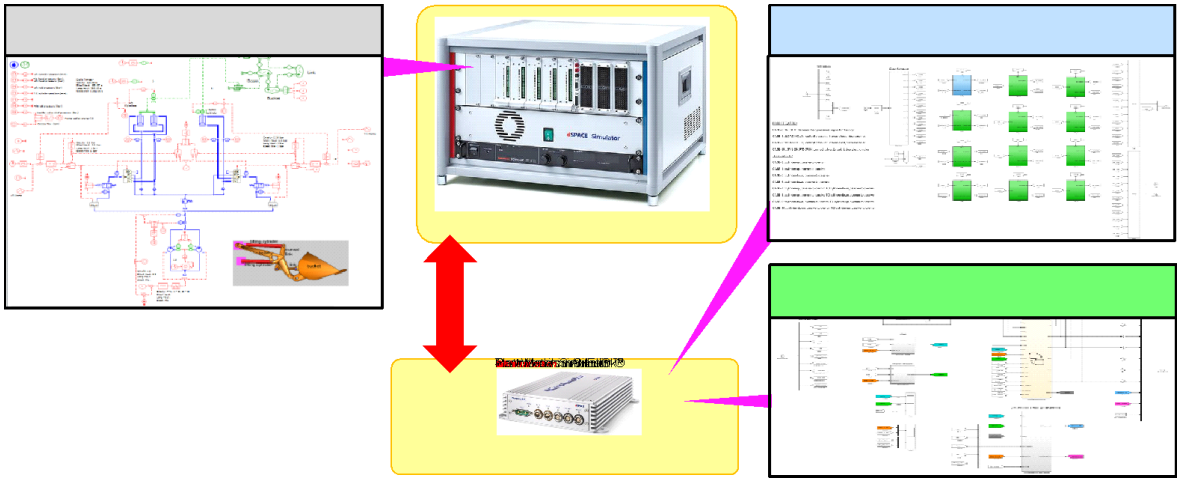

Figure 2.A12: Simulation-In-the-Loop (SIL) architecture

High Fidelity Simulation

High fidelity simulation is conducted with an actual long-haul wheel loader duty cycle. The baseline work-circuit power consumptions for lift, tilt and steering have been obtained. The engine output work is calculated to be 3.11 MJ, while the energy consumed by powering against load from lift, tilt and steering services are 0.65 MJ, 0.32 MJ and 0.32 MJ respectively. The overall work-circuit energy efficiency is calculated to be 41.83%. This is similar to that obtained from our energy saving analysis using simpler models. In the baseline machine, both lift and tilt services are encountering over-running load, which produce regenerative energy that is throttled (wasted) in the baseline machine. In the HHEA architecture, regenerative energy can be recaptured and reused. Together with reducing the throttling loss associated with producing the effective power in baseline and reducing the pump loss in baseline, >65% overall work-circuit energy efficiency or >40% energy saving are expected.

Modeling and simulation of the HHEA and control algorithm was performed in the AMESim-Simulink co-simulation framework for the wheel-loader. The high fidelity simulation was configured with both the baseline load-sensing architecture and the HHEA. In the HHEA case, the nominal passivity based backstepping control algorithm was also applied to track the desired trajectory. The models were exercised to obtain energy usage data. Actual duty cycles of the wheel loader collected through experiments including the operator joystick commands, actuators displacements and actuator loads are used as test vectors to calibrate and validate the model.

The major difference between the static model and the high fidelity model are summarized in Table 2.A3.

Table 2.A3: Key differences between static model analysis and high fidelity model

	Baseline (LS)	**HHEA**
Static model	● Incompressible ● Single pressure compensated pump ● No throttling loss ● Regen flow	● Incompressible ● Fixed displacement main pump @2000rpm ● No throttling loss
High Fidelity model	● Compressible ● 2 pressure compensated pumps (more efficient) ● Valve dynamics throttling loss ● Regen flow	● Compressible ● Fixed displacement main pump @2000rpm ● Valve dynamics and throttling loss

Baseline (Loadsense) comparison

The assumptions used in modeling the baseline loadsense system in the static model (which we relied on for most of the energy saving analysis) and in the high fidelity model differ in various key manners. The most important one being that the static model assumes one pressure compensated pump whereas the high fidelity model assumes two pressure compensated pumps in tandem is used. The tandem pump allows one pump to be unloaded while the other operates at higher displacement (and efficiency). Other differences include assumptions about fluid compressibility and how throttling losses are treated.

The efficiencies (as defined as the ratio between positive output work to input work) for the baseline load sensing system for the static and high fidelity models are summarized in Table 2.A4. The main reason why the high fidelity model has a higher efficiency is because of the use of tandem pressure compensated pumps whereas in the static model, only 1 pressure compensated pump is assumed. Consequently, the pump in the static model operates at lower displacements which tend to be less efficient. Other differing assumptions play relatively minor roles in the difference in the overall efficiency.

Table 2.A4: Efficiencies of baseline LS system

	Static model	High Fidelity
Efficiency	35.5%	46.61%

HHEA comparison

The CPR rail flow pattern during a sample high fidelity simulation of the wheel loader configured with HHEA is shown in Fig. 2.A13. Notice that the spikes at the various discrete instances which occur during rail transitions and are consequences of fluid compressibility.

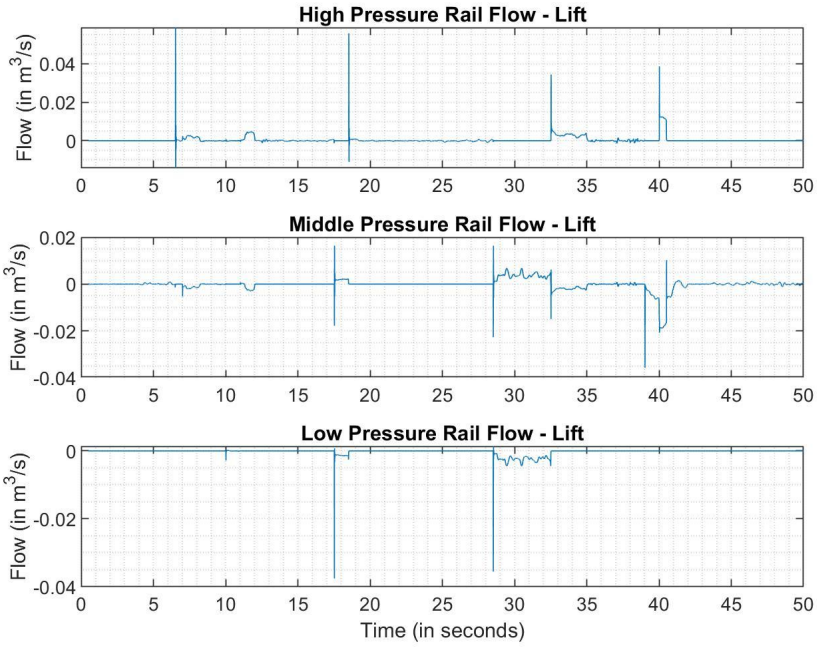

Fig. 2.A13: Common Pressure Rail flow consumption

The energy usage characteristics using a static analysis and the high fidelity simulation are shown in Table 2.A5 and Fig. 2.A14. Both analyses show similar overall efficiencies of 95.8% and 93.7% Both are higher than the target efficiencies of 65%, and represent more than 50% reduction in energy consumption compared to load sensing.

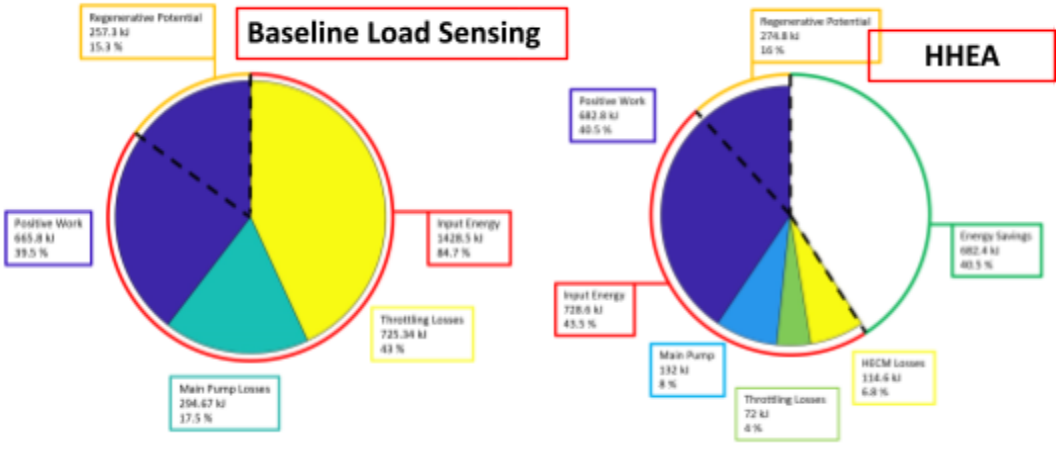

Fig. 2.A14: High fidelity simulation results: energy use comparison between the baseline load sensing case and the HHEA case.

Detailed comparisons between the static analysis and high fidelity model results show that the distribution of the losses are also similar with main pump losses being the highest, followed by HECM losses and valve switching losses. The hi-fi simulation does show a slightly higher energy loss due to throttling which can be attributed to the compressibility of the fluid, which is not directly considered in

the static model.

Table 2.A5: Comparison of Energy Characteristics for the two simulation methods

Parameter	**Static Simulation**	**High Fidelity Simulation**
High Rail - Energy Contribution (kJ)	778	807
Middle Rail - Energy Contribution (kJ)	-178	-192
Low Rail - Energy Contribution (kJ)	0	-4
Main Pump Losses (kJ)	122	131
HECM Losses (kJ)	117	114
Switching/Throttling Losses (kJ)	46.6	71
Regen Potential (kJ)	257	257
Positive Work (kJ)	668	682
Efficiency (%)	**95.8**	**93.7**

The high-fidelity simulation supports the prediction that HHEA can provide at least 65% efficiency or 40% energy saving. Specifically, the efficiency of 93.7 is achieved and an energy saving of 51%. Therefore, the energy saving criteria of this BP's Go/No-GO criteria is satisfied.

2.2 Thrust B - Control Performance

Task 2.B1 – Develop HIL bench-top control setup (200 bar):

In BP1, a control strategy consisting of a nominal control and a transition control was proposed. The goal in BP2 is to test this control strategy in a Hardware-in-the-Loop (HIL) testbed. Task 2.B1 involves the construction of the HIL testbed consisting of:

a) design of the experimental platform;
b) specify, source and obtain components;
c) fabricate experimental platform;
d) conduct tests to validate the experimental platform.

The testbed design is shown in Fig. 2.B1a. To specify and size the components, scaling rules are developed to accommodate the various duty cycles that have been obtained for the 5-ton and 22-ton excavators and the 20-ton wheel-loader. Whereas our initial idea was to use a virtual actuator in which we physically emulate the pressure dynamics, our final design utilizes a physical actuator, and an actual physical emulated load. The virtual actuator approach is more flexible allowing different size actuators to be emulated. On the other hand, the physical actuator and load approach is more realistic. The test actuator and the load actuator are mechanically connected to each other in an opposing configuration. The

position of the actuators are monitored using an optical linear quadrature encoder. The cap and rod side pressures of both actuators are also monitored.

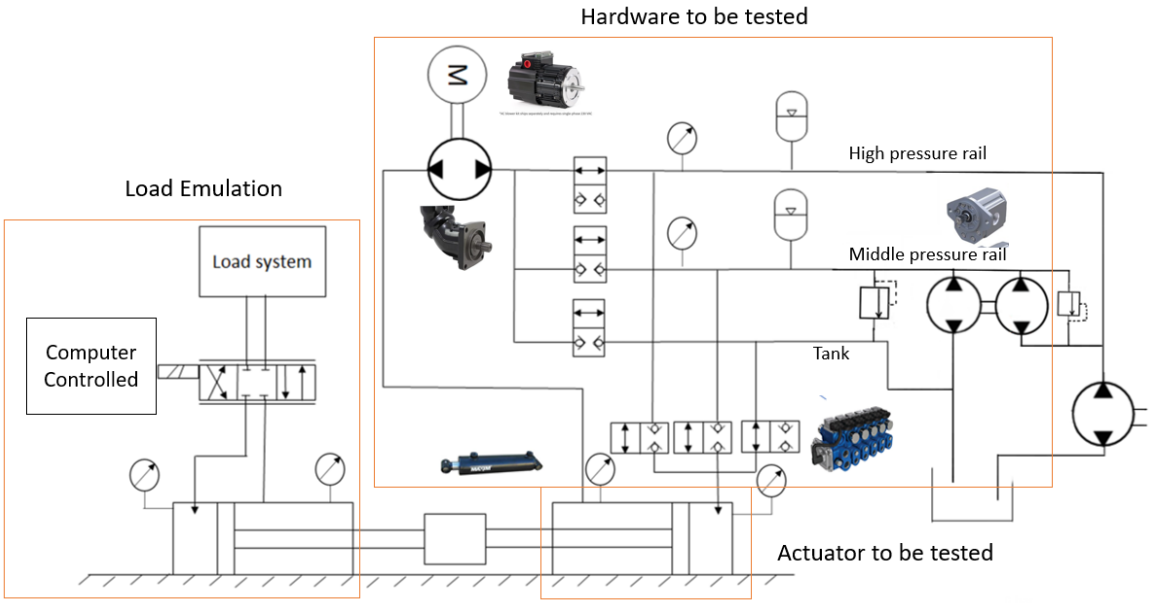

Fig 2.B1a: Schematic of the Hardware-in-loop (HIL) Control Testbed

The Hydraulic-Electric Control Module (HECM) consists of a 5kW Clearpath Teknic PMAC motor with integrated power electronics and a 10cc gear pump/motor. The electric motor can be controlled in either velocity or torque mode. When velocity mode is used, an on-board velocity control loop is utilized.

The 200bar capable testbed is equipped with 3 common pressure rails. The highest pressure rail pressure (200bar) and tank lines are directly supplied by a hydraulic power supply in the lab. A hydraulic transformer setup (a set of equal displacement hydraulic pump/motors connected mechanically and hydraulically connected in a input-shared configuration) is used as an energy efficient means to create the middle pressure rail. With an additional pressure-reducing-relief valve, the output pressure of the transformer is regulated. The 3 common pressure rails are set at 200 bar, 100 bar and 0bar (all gauge). The pressurized rails are equipped with accumulators.

Two sections of Eaton CMA-90 valves are used as switching valves for the pressure rails. Each CMA valve section consists of two independent metering spools and are used for connecting one of the two pressurized rails (fixed to each bank) or tank to either side of the test actuator. Since they are programmable, their response speeds can be adjusted in order to test the effects. Communication between the CMA valve and the control system computer is via CAN bus facilitated using an Arduino bridge.

The load actuator is controlled via a MTS servo-valve to mimic any desired load to be applied on the test actuator. For this, a backstepping nonlinear controller uses the cap and rod side pressures to infer the output force.

The control system is implemented using Matlab Simulink Real Time (SLRT) deployed on a dedicated target PC with data acquisition card and encoder card for various pressure and position measurements and deploying signals. Further description of the hardware-in-the-loop testbed can be found in [7].

Due to Covid-19 pandemic and the consequent laboratory closure and supply chain backlogs in 2020, the construction of the testbed was delayed for several months. It was subsequently completed and commissioned in November 2020 as shown in Fig. 2.B1b.

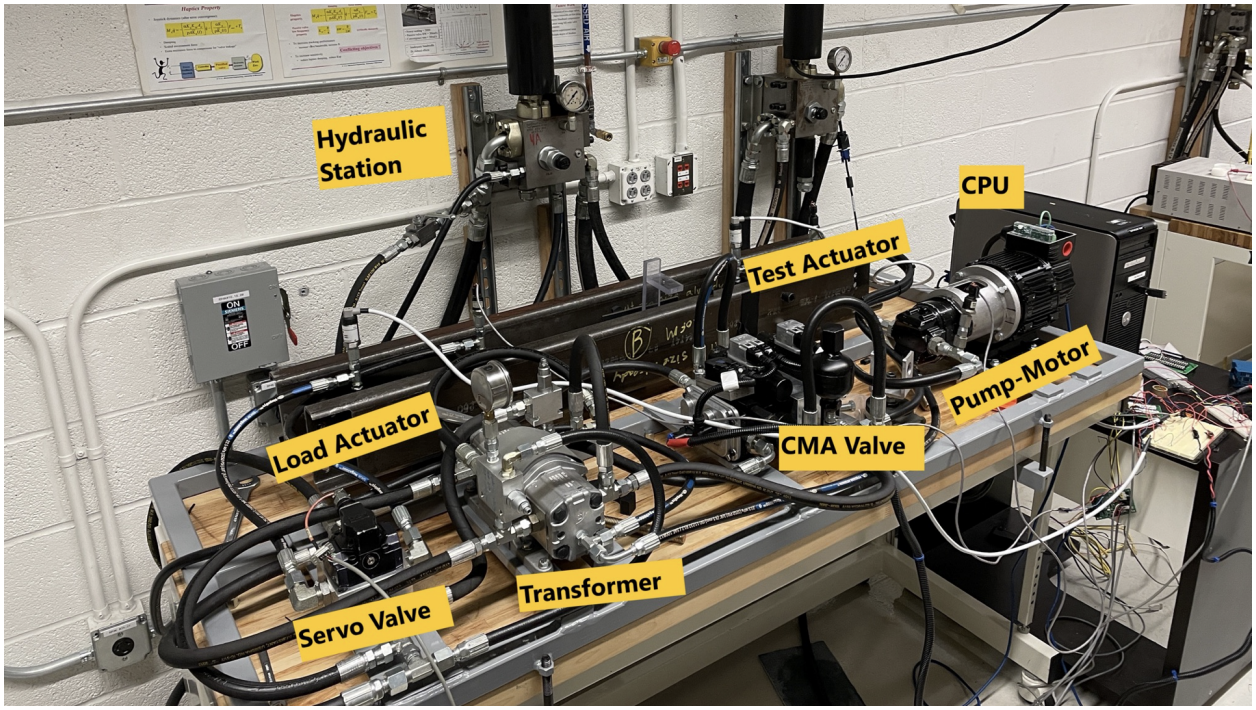

Fig 2.B1b: Hardware-in-loop (HIL) Control Testbed.

Task 2.B2 – Verify single-axis control on HIL bench-top setup (200 bar):

Least norm transition control

At the conclusion of BP1, the control strategy was identified to consist of a nominal control and a (pressure rail) transition controller (Fig. 2.B2). Both use the electric motor torque as the control input. The nominal controller is a passivity based backstepping controller, whereas the transition controller was a bang-bang control. Although the bang-bang control can be effective and ensures a short transition period, it is difficult to generalize for arbitrary transitions the timings must be designed specifically for each rail switching condition, including pressures, actuator speed, and fluid volume etc. To enable easy computation of the transition controller, a least-norm controller was proposed instead to handle the transition events in the presence of electric motor torque limitation [9].

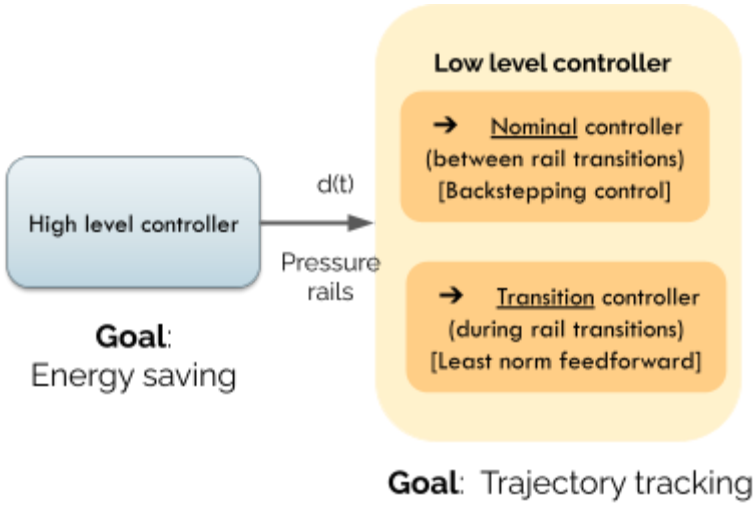

Fig. 2.B2: Control strategy of the HHEA

The concept of least-norm control is that of disturbance cancellation using a feedforward controller. By linearizing the system dynamics, linear system dynamics can be written as:

$$\dot{X} = AX + B_P \begin{bmatrix} F_L(t) \\ P_{cap}(t) \\ P_B(t) \end{bmatrix} + B_U T_M(t)$$

where $X = [x, \dot{x}, P_{rod}, \omega]^T$ is the state vector of position, velocity, actuator rod side pressure and electric motor speed, T_M is the electric motor torque input, $[F_L, P_{cap}, P_B]$ are the disturbances due to external load, and pressure rail switching. The idea of the feedforward control is to use the motor torque T_M to cancel, as much as possible, the effect of the disturbance due to pressure rail switching.

In the case of the least norm transition control, realizing that with electric motor torque limitation, it may not be possible to completely cancel out the effect of disturbance. Instead, the problem is to find a feedforward electric motor torque control such that the actuator and pressure trajectories return to the desired state a short time (e.g. 20-40ms) *after* the rail switching event. Thus, we explicitly acknowledge that there will be a non-zero effect within the first 20-40 ms due to the pressure rail switch. Since there will be many T_M trajectories that can satisfy this constraint, we choose the one that minimizes the L2 norm of the control. Hence, the least norm transition control problem is formulated as:

$$min \left[\int_{t_0}^{t_f} T_m{}^2(t)\, dt \right] \text{ such that } X(t_f) = X^d(t_f)$$

Two versions of the least-norm controller have been devised: one is completely open-loop and the other uses valve timing in a feedback loop as a secondary control. A very useful feature of the least-norm transition control is that scaling rules can be defined to generalize the least-norm controls for arbitrary rail transitions and duty cycles have also been developed. Figure 2.B3 illustrates the process. Here, the term Δx can be obtained by measurements at the beginning of each rail transition. It is then applied by premultiplying by a precomputed kernel to obtain the desired feedforward controller.

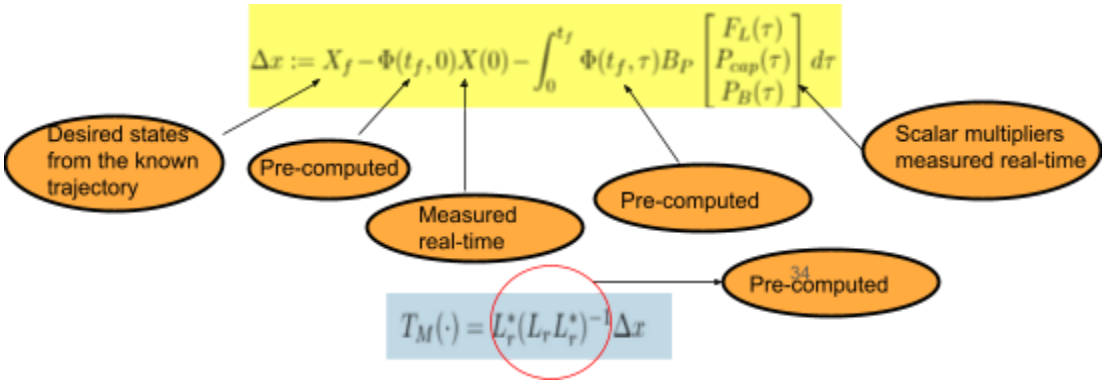

Fig. 2B3: Scaling of the least-norm transition controller for different pressure rail switching conditions

Refinement of the control to take into account finite time valve dynamics for rail switching has also been made. In coordination with the design of the HIL testbed, test vectors which are scaled versions of the duty cycles obtained from OEMs have also been completed. For details of the development of the least norm transition controller, please see [9].

Control experiments

Sample initial experimental control performance results are shown below.

Constant load, no CPR switch

Fig. 2.B4 the case where the load force and CPR selections are not changing, the maximum error is 0.57mm and the RMS error is 0.28mm. We found that stiction in the actuator plays a significant role in the control performance. This is evidenced from the worst error occurring when the velocity switches direction. As a consequence the controller has incorporated stiction compensation. This shows that the system with a backstepping controller is able to successfully track a desired position command under a constant load.

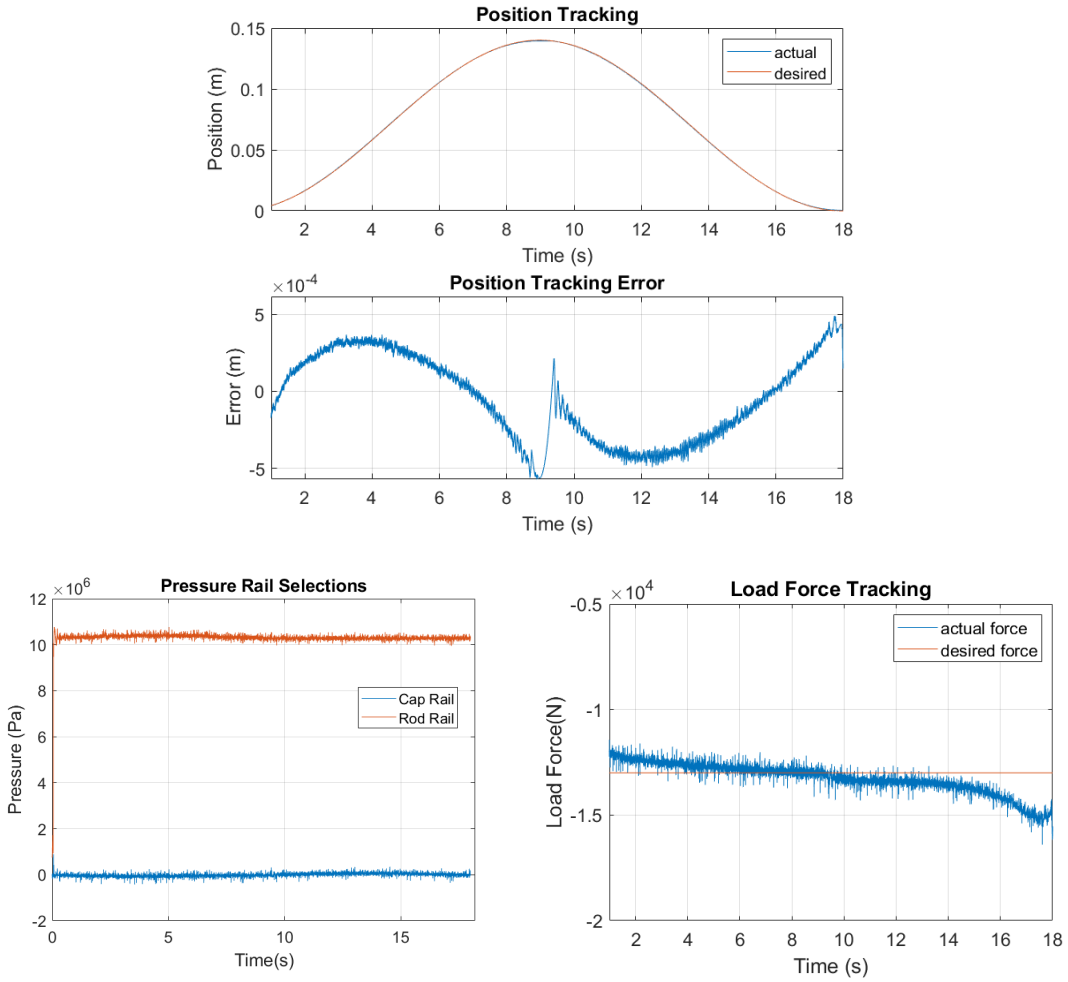

Fig. 2.B4: Constant load, no CPR switch results (max error = 0.57mm)

Load force variation and CPR switch

In the second example, both load force and rod side CPR switch occur. This simulates the situation that when the load force increases, a different set of CPRs are needed to produce the hydraulic rail force to counteract. Without the switch, large torque will be demanded of the electric motor in the HECM (which is intended to be small). In this case, Fig. 2.B5 shows that the maximum position tracking error is increased slightly to 087 mm which is still quite satisfactory.

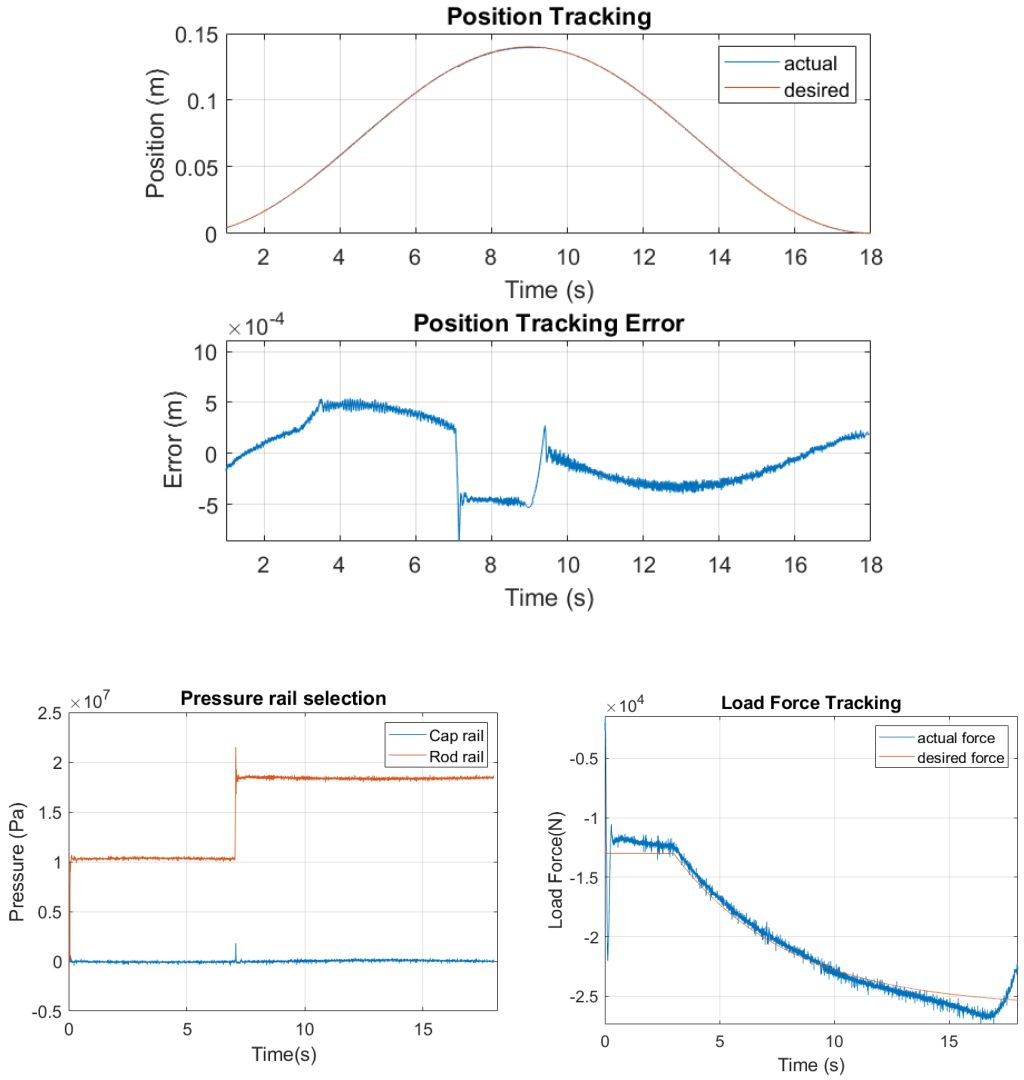

Fig. 2.B5: Varying load, rod side CPR switch results (max error = 0.87mm)

The control strategy has also been refined to further improve performance:

1) Stiction and the damping effect on the hydraulic actuator are accounted for. Stiction is found to be a major cause of position tracking error when the velocity of the actuator becomes zero.
2) The back-stepping controller is refined by adding an integral term to eliminate steady state error.
3) The gains of the controller were further tuned to place the poles more suitably to reduce pressure ringing and to improve tracking performance.
4) The controller for the load emulation has also been significantly improved.
5) A relatively long switching delay of the CMA valve of 50ms has been reduced to 25ms. Instead of using inner loop closed loop control (within the valve's firmware) for valve opening, an open-loop PWM control strategy for opening and closing the CMA valves are used instead. This allows the valve to open as fast as possible.
6) The least norm transition controller has been implemented and tested.

With these refinements, position error has been decreased by 50%. This controller has been used to study the effect of the controller on the energy saving potential of the architecture. Improved control performance can be seen in Figs. 2.B6-B10.

The updated backstepping controller was tested under nominal conditions where both the pressure rails are not switching. The load emulation module ensures that the desired load force is emulated precisely (Fig. 2.B6). Fig. 2.B7 shows the nominal performance of the controller when there is no rail switching. The peak error is just 0.35 mm which is 0.22 percent of the (~15cm) stroke.

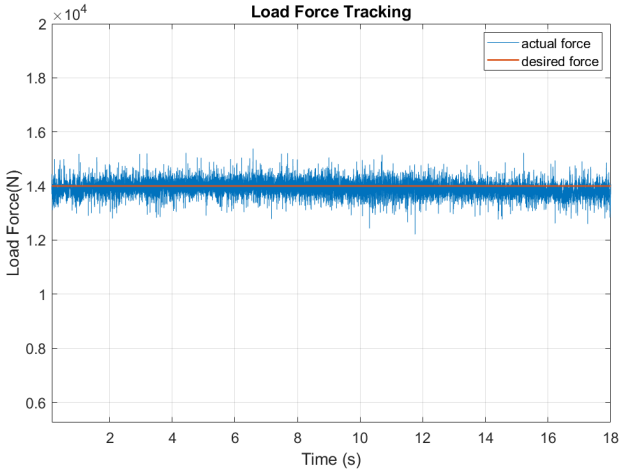

Fig 2.B6: Load applied on the actuator

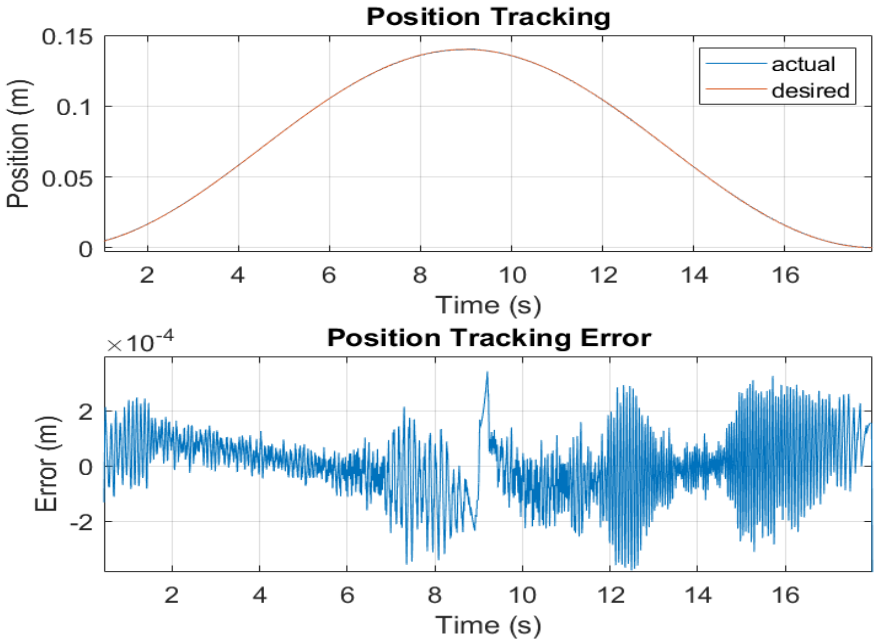

Fig 2.B7 Tracking Performance (no switching): Maximum error is 0.35mm.

A transition controller has been implemented to take care of the pressure rail switching cases. Fig. 2.B8 shows the case with pressure rail switching on the rod side in anticipation of an increase in load force. Despite the pressure rail switch, the maximum tracking error is 0.8mm (and rms error is 0.4mm).

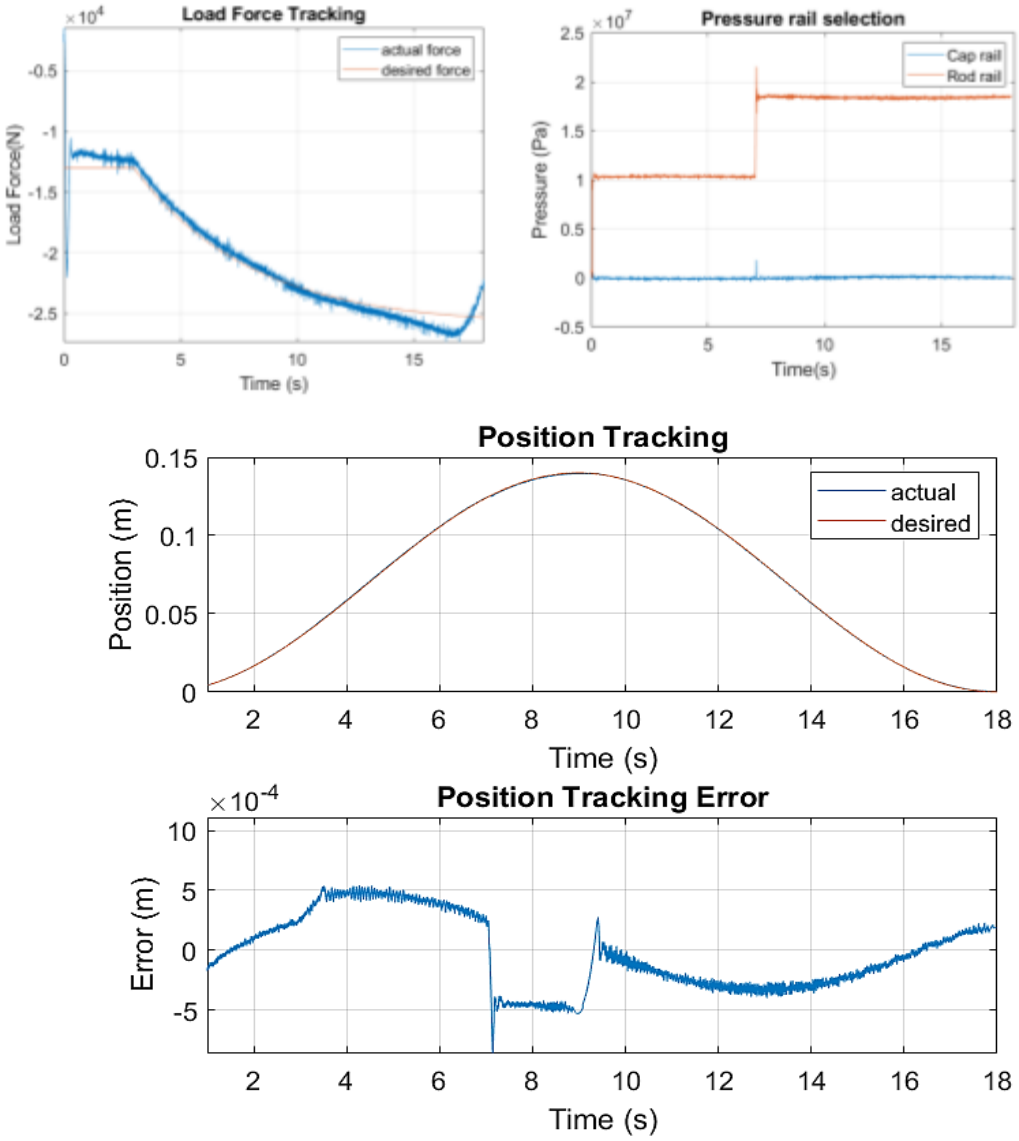

Fig. 2.B8: Top: Load force variation and subsequent pressure rail switch from medium to high on the rod side. Bottom: Tracking performance (max error = 0.8mm, rms error = 0.4mm)

Next we consider a pressure rail switch on the capside in Fig.2.B9. Here, the cap side pressure rail is switched from high pressure to medium pressure as the load force is reduced. Despite the pressure rail switch, the maximum error is 1.8mm and the rms error is 0.8mm.

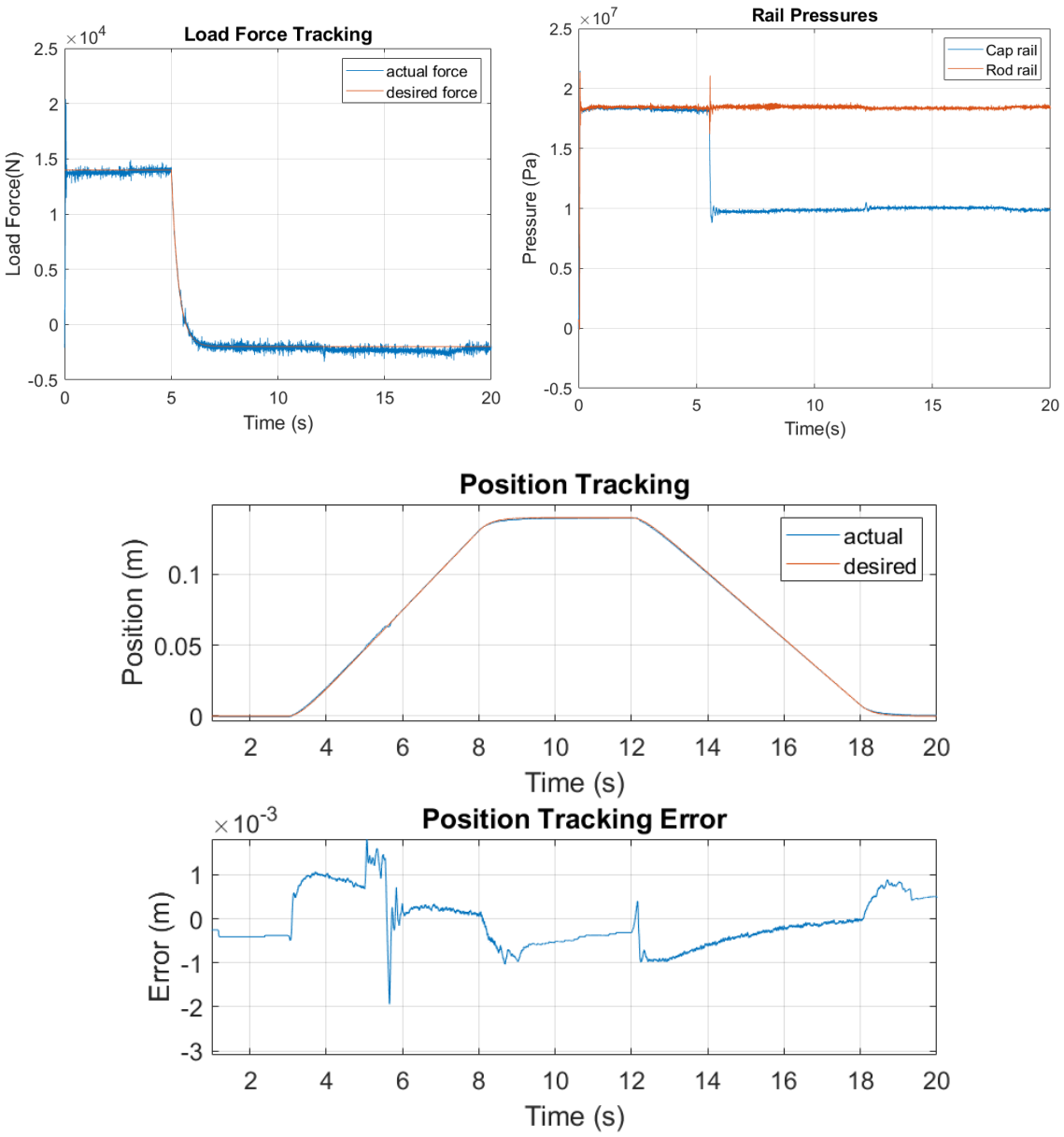

Fig. 2.B9: Top: Load force variation and subsequent pressure rail switch from high to medium on the cap side. Bottom: Tracking performance (max error = 1.8mm, rms error = 0.8mm)

Figs. 2.B10 is an example of a case where the pressure rails on *both* sides of the actuator switch simultaneously (from middle pressure rail to high pressure rail). This is the most challenging as far as control performance is concerned. It shows that with the open loop least norm transition control is quite effective in taking care of the rail switching events. The maximum error is 1.8 mm which is 1.16% of the stroke. In this case the transition control was deployed for 100 ms from 5.5 sec to 5.6 sec.

Note that Figs. 2.B7-2.B10 also demonstrate the load emulation capability of the HIL testbed for both constant and time varying desired load forces.

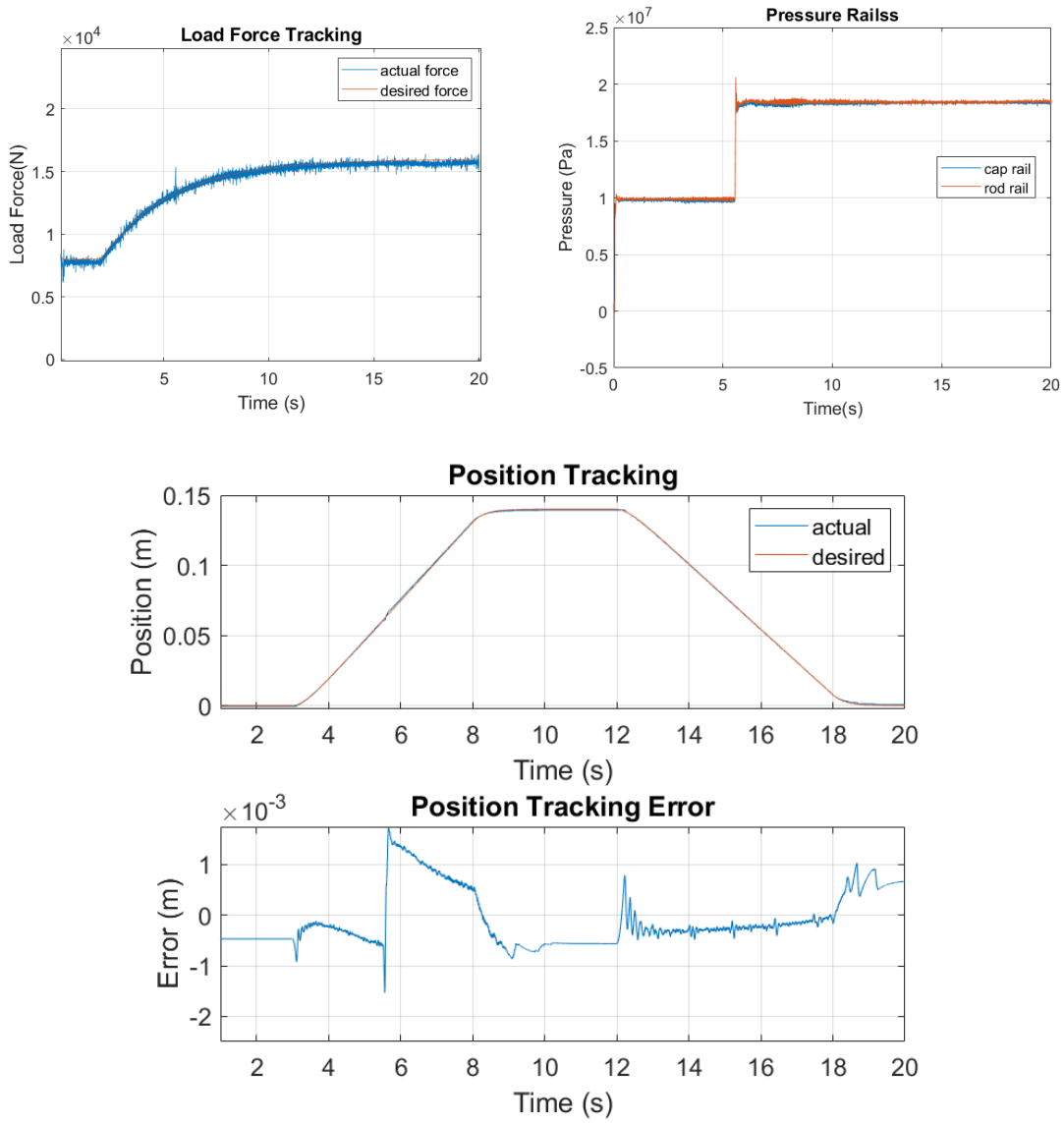

Fig. 2.B10: Top: Load force variation and subsequent pressure rail switch from medium to high on both the cap and rod sides. Bottom: Tracking performance (max error = 1.8mm)

Fig. 2.B11 shows a comparison of the control performance with the nominal control and with and without the transition controller. The transition controller reduces the error from 6.5mm (with only the nominal controller) to 1.8 mm (with the transition as well).

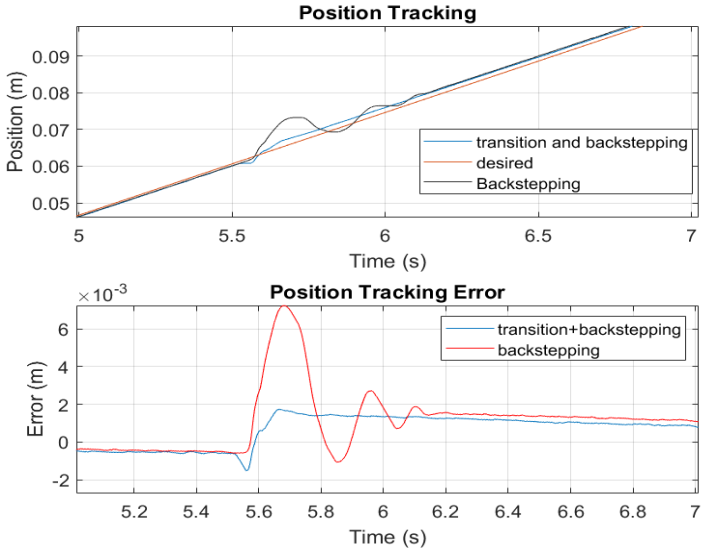

Fig. 2.B11 Comparison of the nominal controller only and transition and nominal controller in the event of pressure rails on both sides switching simultaneously.

Finally, we show the HIL testbed tracking an arbitrary duty cycle (both position and force) with multiple pressure rail switches. These results are shown in Figs. 2.B12.

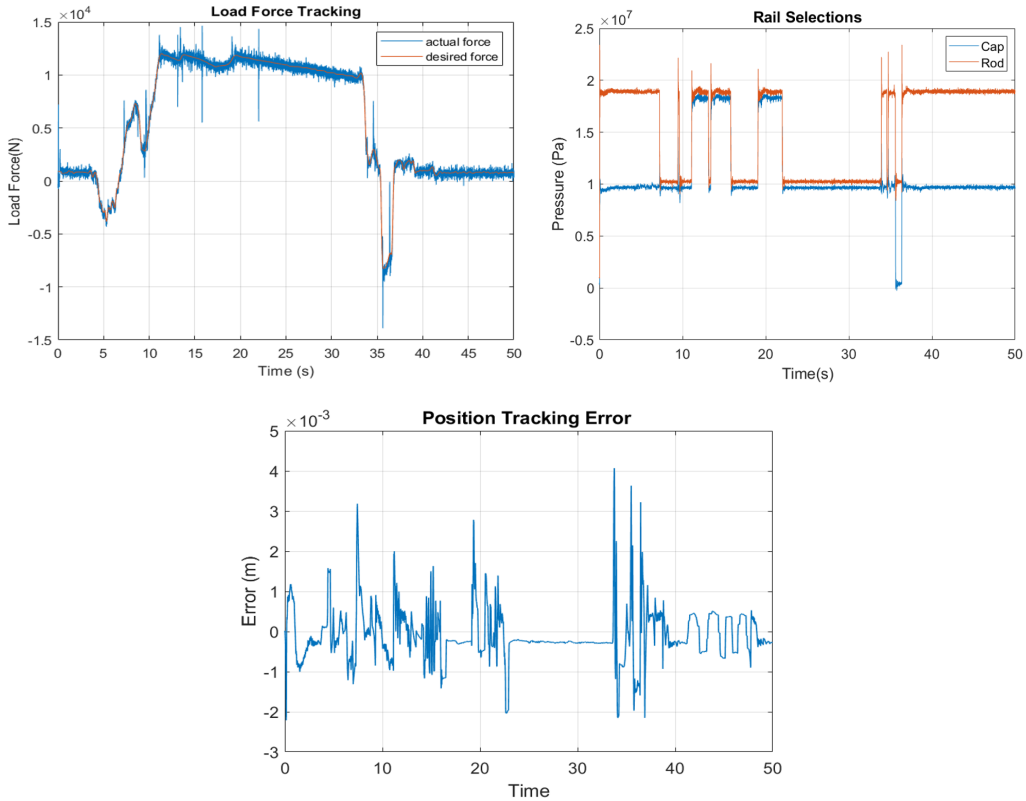

Fig. 2.B12: (Top) Load force variation and subsequent pressure rail switch for an arbitrary OEM provided duty cycle; (Bottom) Control tracking error for the duty cycle

With the successful control of the actuator motion with and without pressure rail switches, the control strategy is deemed validated on the medium pressure (200bar) hardware in the loop testbed. Therefore, the control performance criterion for the end of BP2 Go/No-Go decision is deemed satisfied.

2.3 Thrust C - Integration

Thrust C focuses on the hydraulic-electric integrated control module. In BP2, the focus is on: 1) analyzing and validating electric and hydraulic subsystem models, 2) developing and exploring design space in a multi-physics optimization framework, 3) creating a final design of the prototype.

Task 2.C1: Analyze and validate subsystem models:

- **Electric subsystem:**

1. For the electrical system, analytical sizing equations were developed and three promising axial flux machine variants (Yokeless and Segmented Armature (YASA), Coreless machine, and Single rotor machine) were analytically sized. Different slot-pole configurations were explored for these machines to determine the most suitable machine to achieve the project objectives. It was observed that as the number of slots and poles increase, the machines are predicted to achieve better gravimetric power densities and lower rotor moments of inertia. It was concluded that a single rotor machine with a slot-pole combination of 16 poles and 24 slots is most favorable for our application.
2. An electrical machine testbed capable of operating the final prototype in BP3 was developed. The electric machine testbed consists of two subsystems: a) Controller b) Power stack. Each of these subsystems is briefly described in this section.
    a) **Controller:** The controller subsystem is responsible for controlling the motor by generating suitable gating signals for the power stack. It is based on custom control hardware being developed by the PI at University of Wisconsin. The control hardware is referred to as the Advanced Motor Drive Controller (AMDC). The AMDC comprises an FPGA, a dual core DSP, and several I/O and PWM ports. Custom firmware libraries for motor control are also available in the AMDC in an open source GitHub repository, which makes it easy to implement and test various control algorithms. More information on the AMDC can be found in[2] [3]
    b) **Power Stack:** The proposed prototype electric motor ratings are summarized in Table C1. A 250 V DC bus was chosen for safety reasons. The power stack utilizes wide-bandgap Silicon Carbide half-bridge power modules from Cree Wolfspeed that are rated for 1200 V and 250 A[4] . Gate driver boards[5] designed by Cree are used to translate

[2] AMDC Hardware repository <https://github.com/Severson-Group/AMDC-Hardware> (Accessed on 04-20-2020)
[3] AMDC Firmware repository <https://github.com/Severson-Group/AMDC-Firmware> (Accessed on 04-20-2020)
[4] Datasheet for CAS325M12HM2 SiC power module <https://www.wolfspeed.com/power/products/sic-power-modules/cas325m12hm2> (Accessed on 04-20-2020)
[5] Datasheet for CGD15HB62LP gate driver board <https://www.wolfspeed.com/power/products/gate-driver-boards/cgd15hb62lp> (Accessed on 04-20-2020)

the control signals from the AMDC to the expected signal levels at the power module. Heatsinks installed on the power stack enable air cooling of the drive.

The power stack ratings were oversized to enable testing the final prototype motor over the extreme operating conditions typical of the off-highway vehicle drive cycle. The electric motor drive system with the power stack and controller is shown in Fig. 2.C1.

Table 2.C1: Motor prototype ratings

Parameter	Specification
Rated power	20 kW
Rated speed	15000 RPM
Line-line voltage	160 V_{RMS}
Current	72 A_{RMS}

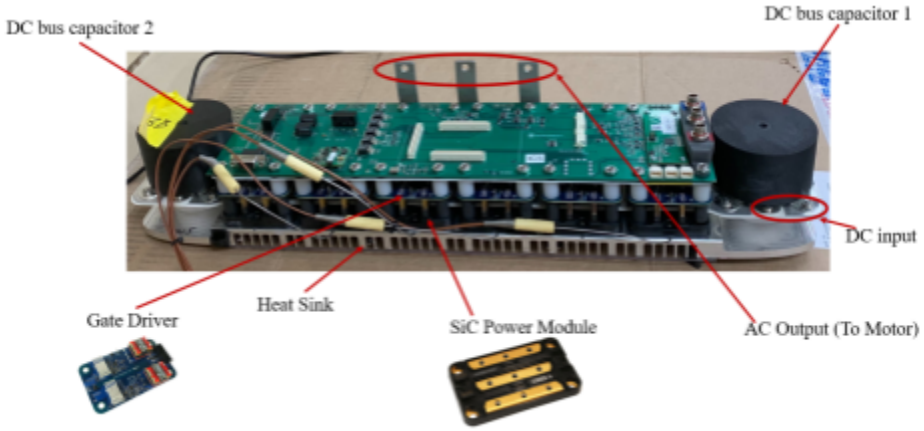

Fig 2.C1: Electric machine testbed - Power stack

3. The electric steel to be used in the final prototype was experimentally characterized. Emphasis was placed on constructing electric steel samples using processes similar to how the final machine will be fabricated (i.e., laser-cut or tape-wound laminations) and characterizing the steel samples at the expected operating points (frequency and magnetic saturation) of the prototype. The characterization results were used to create material models (core loss and B-H curves) in the FEA tool. Experimental results were compared with manufacturer provided data for two of the materials and it was found that although they follow similar trends, significant quantitative differences are observed. Fig. 2.C2 shows some B-H curves for the three materials tested, at different peak values of B fields, obtained at 2kHz frequency which is the fundamental frequency of the electric machine.

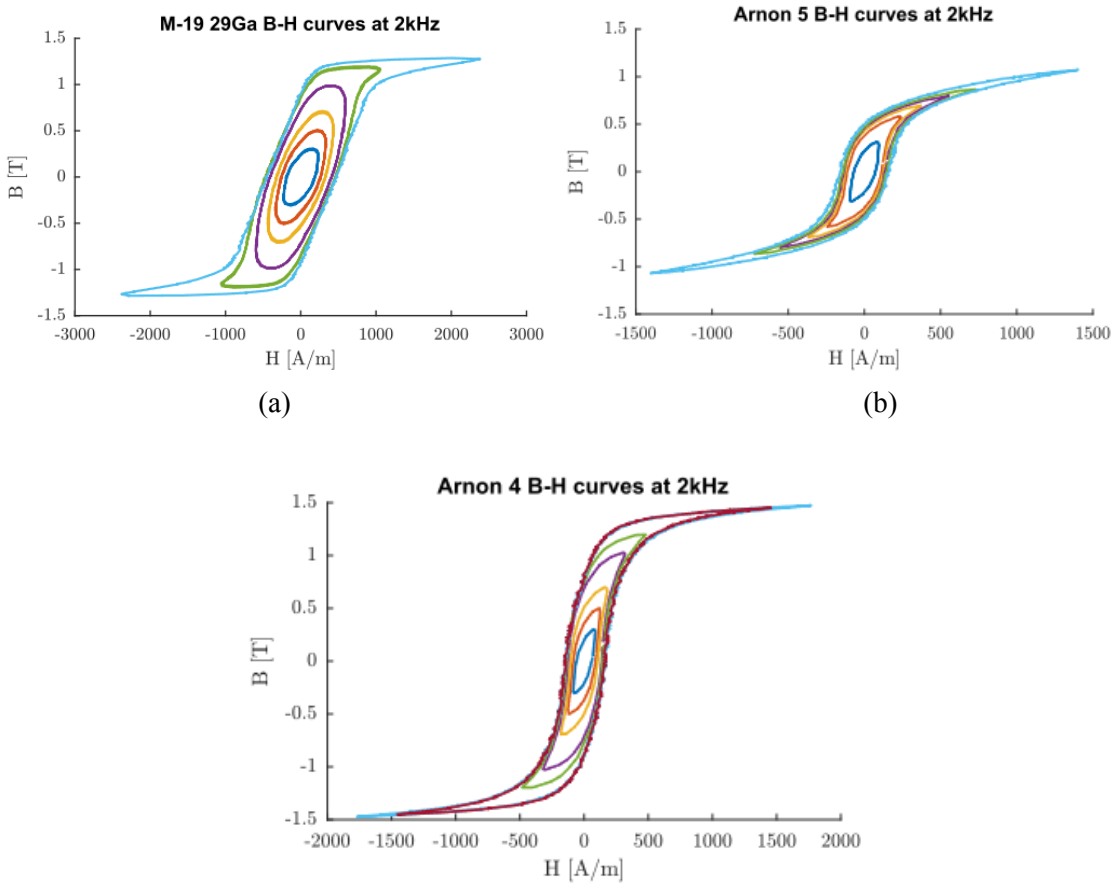

Figure 2.C2: BH curves: (a) M19 29Ga steel; (b) Arnon 5 steel; (c) Arnon 4 steel.

A new set of FEA runs with the updated material models was performed for the optimal electric machine design to accurately determine its performance. The difference in performance arising due to changes in material property is also analyzed. Some of the results are reviewed below.

The experimental data obtained can be broadly categorized as i) Material magnetization characteristics (B-H curves) and ii) Loss characteristics. For use with FEA tools, the B-H characteristic and loss characteristics need to be further processed. The material magnetization characteristics (BH curves) were obtained at several H field magnitudes that need to be corrected by the material stacking factor $k_{stack} := \frac{N_{lam} t_{lam}}{t_{core}} (1 - \frac{t_{C5}}{t_{lam}})$ where N_{lam} is the number of laminations, t_{lam} is the thickness of each lamination, t_{core} is the total axial thickness of the core, t_{C5} is the thickness of the C5 coating on each lamination. The calculated stacking factors are then obtained using in-house capabilities at UW-Madison and slightly updated upon recommendation from fabricators as listed in Table 2. C2.

Table 2.C2 : Stacking factors for the experimental cores

Material	Lamination thickness [mm]	t_{core} [mm]	Type	Stacking factor (UW/updated)
M-19 29Ga	0.36	3.77	stacked	0.94/0.97
Arnon 5	0.127	5	tape wound	0.95
Arnon 4	0.101	3.12	stacked	0.94

The core loss was also experimentally determined using the power analyzer, at several combinations of B fields and frequencies. The curve fit functionality provided by the FEA tool Infolytica MagNet® was used to determine the loss coefficients using the experimental loss data. The experimentally updated loss coefficients, used to update the material models, are compared with the default loss coefficients from the FEA tool's material library.

- **Hydraulic subsystem:**

1. A mathematical model of a radial ball piston pump was developed and validated to evaluate its performance at different operating conditions. The mathematical model included the cylinder pressure dynamics due to the piston displacement and valve timing as well as two interface models: ball piston to cylinder wall interface and pintle-rotor interface. Both interface models predict the torque loss and leakage at the relative interfaces considering the complex dynamics of the cylinder block and ball piston at each time step. Inputs to the model include the geometric parameters, valve timing, and operating conditions. The outputs are the different energy losses (torque, leakage) and efficiency of the pump.
2. The radial ball piston pump model was experimentally validated using an off-the-shelf Eaton Hydrostatic 720-001 radial ball piston pump, which is a bi-directional variable displacement unit with a speed limit of 3600 rpm (Fig. 2.C3). The pump under test was shaft coupled to a hydraulic motor, driven by a hydraulic power unit. The load on the pump was controlled with a needle valve in parallel with a relief valve. Instrumentation was used to measure the pressure differential across the pump, flow rate out of the pump, and input shaft torque and speed.

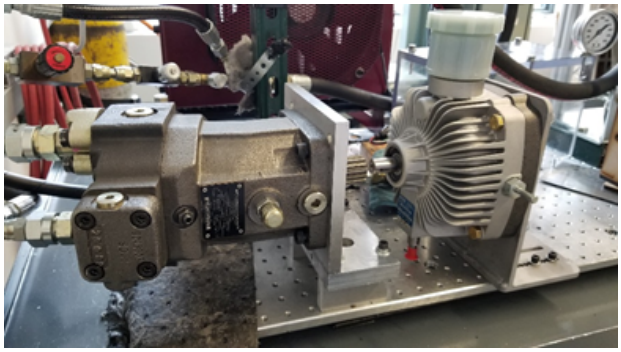

Fig. 2.C3: Radial ball piston pump used to experimentally validate the mathematical model.

A series of experiments were run across a wide range of operating speeds and pressure differentials. Port pressures, flow rate, and the temperature of the hydraulic oil were measured during the test. The Eaton pump geometrical parameters, the pressure differential, temperature of the oil and speed data were used as inputs to the pump model and the losses (leakage, torque) were estimated at the different interfaces. These model results were compared with the experimental results and any discrepancies were addressed. The overall efficiency showed reasonably good agreement for the model, although both leakage and friction losses were under predicted.

To provide more insight, experiments were performed to isolate the leakage of the pump. To measure the leakage, the case drain was connected to a beaker for a known time period. After weighing the beaker and converting to volume, the leakage could be calculated. The model simulations underpredicted the leakage significantly. As leakage has a strong correlation with the temperature, and because the bulk oil temperature was measured, it was expected that the oil temperature at the interfaces would be notably higher. The simulation was run assuming a 50 degree Fahrenheit temperature increase at the leakage interfaces. As shown in Figure 2.C3, with this change, the predicted leakage is much closer to the experimental results. In light of this finding, a heat transfer model was also developed to accurately determine the temperature in the thin gap.

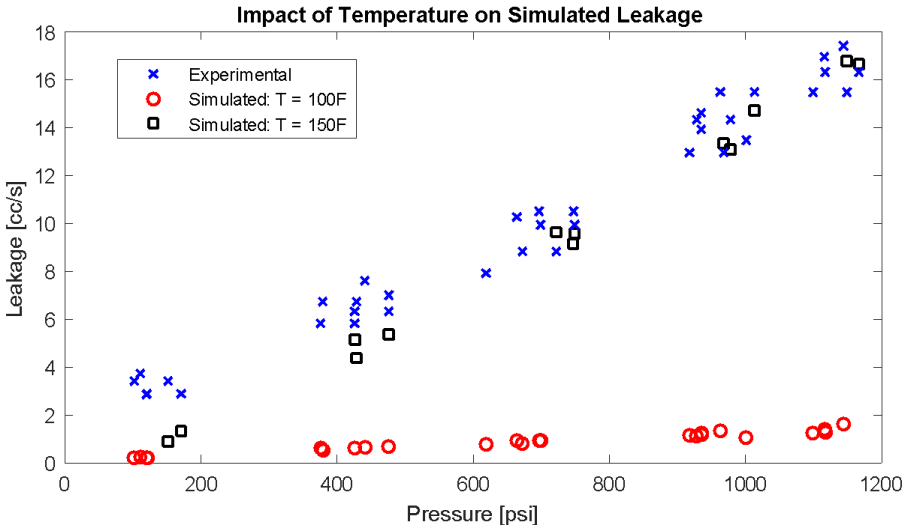

Figure 2.C3: Leakage Comparison Between Experiments and the Hydraulic Model Predictions at Different Interface Temperatures.

Simulations also predicted minimal losses at the pintle rotor interface. It was originally assumed that the rotor would stay concentric around the pintle, but this is not a reasonable assumption considering the unbalanced forces acting on it. Therefore, a model was developed to account for the unbalanced forces and predict the eccentricity at the pintle-rotor interface. After the eccentricity was known, the losses could be more accurately modeled. Fig. 2.C4 shows a fifth of a cycle (corresponding to 1 of 5 pistons) of how the losses at the pintle-rotor interface change when the eccentricity is considered.

Other adjustments to the model are considering the transition from the hydrodynamic lubrication regime to the elastohydrodynamic lubrication at the ball cylinder interface. This will cause increased

torque loss, a result the current model is underpredicting. These model adjustments are compared against the experimental results to validate the model before it is used to optimize the design of the hydraulic machine.

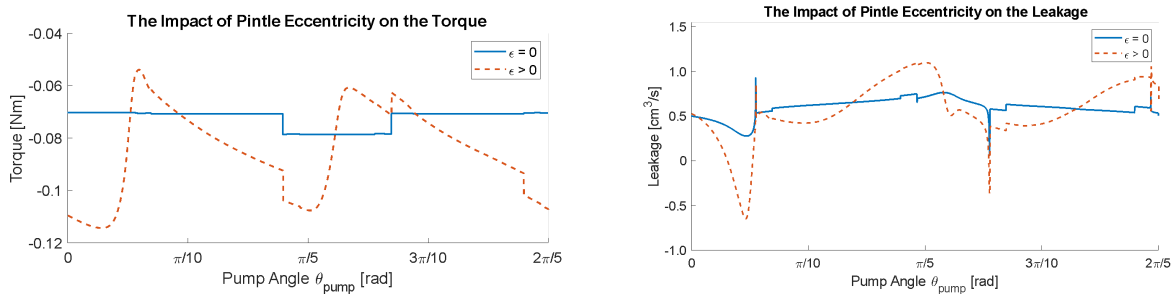

Figure 2.C4: The Impact of Eccentricity at the Pintle-Rotor Interface on the Predicted Pump Losses

3. Experimental validation of the radial ball piston pump model demonstrated that the pump efficiency can be predicted within 10%. The coupled optimization of the hydraulic pump and electric motor has shown that a rotating speed of 12,000 rpm is needed to achieve the required power density milestone. At these high speeds, the model predicts that the dynamic motion of the ball piston inside the cylinder would cause the ball to move towards the cylinder wall for most of the operating conditions. This increases both the torque loss and the leakage past the ball in comparison to a centered ball. These losses also increase in a non-linear manner with pressure and operating speed, resulting in an undesirable drop in pump efficiency at high speeds.

4. *Hydraulic pump architecture change* At these high speeds, the model predicts that the dynamic motion of the ball piston inside the cylinder causes it to move towards the cylinder wall for most of the operating conditions. This dynamic motion of the ball piston increases both the torque loss and the leakage past the ball in comparison to a centered ball. These losses also increase in a non-linear manner with pressure and operating speed, resulting in an undesirable drop in pump efficiency at high speeds.

   To avoid the losses created by the ball piston, the pump architecture was revised from a ball piston to a cylindrical piston to reduce losses at high operating speeds. In the selected pump architecture, a cylindrical piston is attached to a slipper pad, which works as a hydrostatic bearing where pressure from the cylinder is used to maintain a thin liquid gap between the slipper and cam to reduce the shearing loss at the slipper. In the new design, the cam is allowed to rotate, resulting in low frictional losses during steady-state operation. The old ball piston and new cylindrical hydrostatic piston design are shown in Fig. 2.C5a. The package size of the cylindrical piston pump is slightly smaller than the ball piston design, allowing it to still package within the rotor of the electric motor.

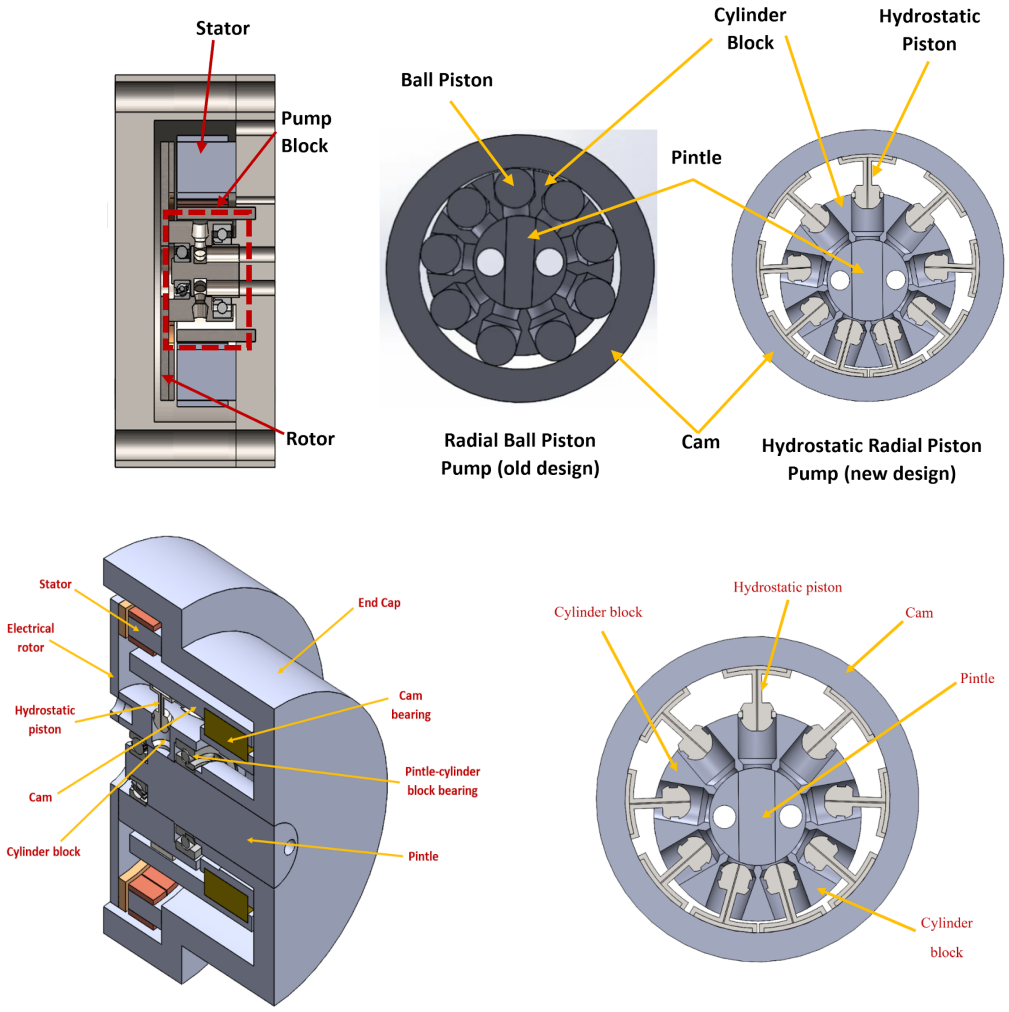

Fig. 2.C5a: Top: CAD renderings of the radial ball piston (old) and the radial hydrostatic cylindrical piston pump/motors (new). Bottom: CAD model of the integrated electric motor and radial hydrostatic cylindrical piston pump

A comparison of the predicted losses with the initial concept of radial ball piston pump and the updated concept of radial hydrostatic cylindrical piston pump is shown in Fig. 2.C5b. This shows that the large leakage and friction have been significantly reduced, and the total losses is reduced to 86%.

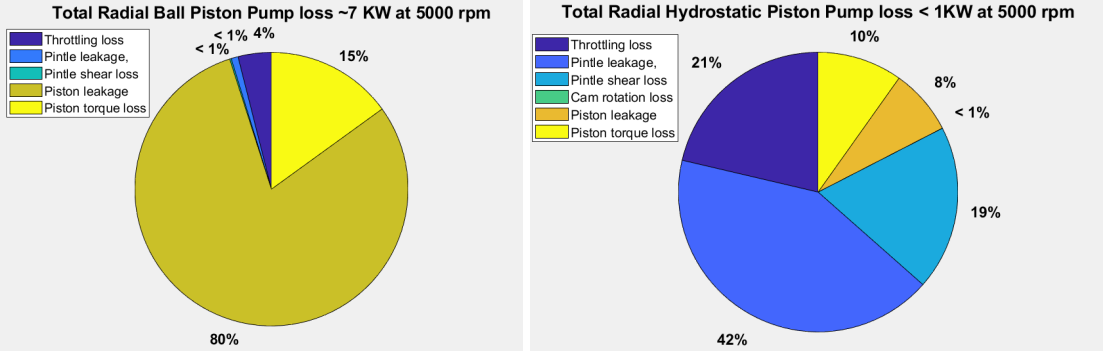

Fig. 2.C5b: Losses in a radial ball piston pump and a radial hydrostatic cylindrical piston pump.

- **Thermal subsystem:**

- A lumped-parameter thermal model has been developed for the integrated pump-motor design to analyze the cooling performance of the hydraulic oil at different operating (speed, torque) conditions considering the electric machine as a heat source. Excessive heat can melt the insulation between stator and coil and also creates permanent magnet demagnetization resulting in the inferior performance of the electrical machine. Frequent overheating also shortens machine life. Figure 2.C6 shows heat generation at different segments of the electric machine (AF-PMSM). The inputs to the thermal models are the pump/motor geometry, material properties, and convection heat transfer coefficients at the solid-oil interfaces. The outputs include the different temperature distribution in the various components at steady state operating conditions.

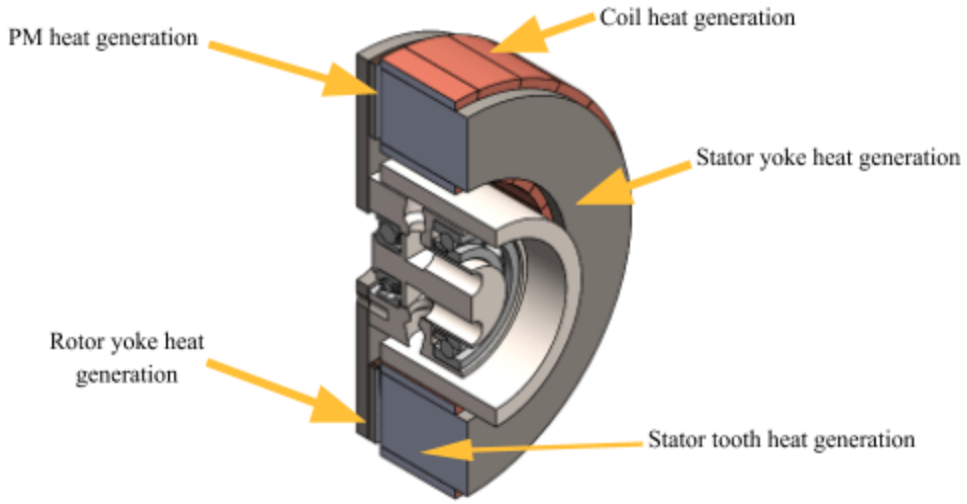

Fig. 2.C6: Heat generation in the electric machine.

- To perform thermal analysis, a lumped parameter model has been constructed for evaluating the integrated pump motor design. Lumped parameter model is a thermal network-based model that splits the electrical machine into different component-nodes and connects that with heat sources as well as the thermal (conduction and convection) resistances to perform thermal analysis. Component geometry, material properties and convection heat transfer coefficients (at the solid-liquid interface) etc. information are required to calculate these conduction and convection

resistances. To conduct lumped parameter thermal analysis for the integrated pump-motor model, only a segment of the total design has been considered. The segment is then split into nine component nodes shown in Fig. 2.C7 (except rotor and PM). Including those, a total 21 node thermal network has been developed to account for both axial and radial directional heat transfer from each component.

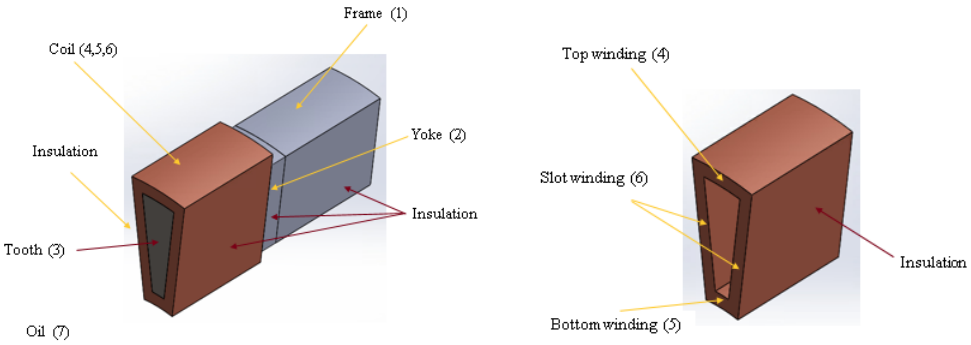

Fig. 2.C7: Electrical machine segments

- By applying energy equation to each nodes the following matrix equation can be constructed to solve for nodal temperatures: $[R][T] = [G]$ where R represents the thermal resistance matrix, T is the column matrix of nodal temperatures, and G is the column matrix of heat generation. In the process of (hydraulic and electric model) optimization, the thermal model is simultaneously fed with data from interconnected electrical (motor/generator) and hydraulic (pump/motor) models. The electrical model provides motor geometric parameters and component-wise heat generation information and the hydraulic model provides pump speed, oil temperature, and leakage rate information to the thermal model. The motor geometric parameters as well as the material properties from the electrical model are then used to calculate the conduction resistances at the thermal network. The convective cooling of the electrical components is influenced by the hydraulic oil properties, component geometry, and the rotational speed of the electrical rotor. Considering these parameters, the standard empirical correlations are used to calculate the convection heat transfer coefficient at different locations of the integrated pump-motor model.
- The model predicted a safe cooling performance within 2500~15000 rpm operation, however, at low speed (<2500 rpm) operation, the heat transfer coefficient was reduced, causing potential overheating. To address this issue, an external source of oil supply through the stator-cam gap was designed, creating a short oil flow path between the stator-teeth, drastically improving the cooling performance at the low speed.

Milestone 2.2: Electrical and hydraulic subsystems in the HECM analyzed

As task 2C.1 is complete, Milestone 2.2 which calls for the analysis of subsystem models for the HECM is satisfied. We summarized some of the key findings below.

Milestone 2.2 - Electrical subsystem analysis

For the BP1 Go/No-Go decision, the axial flux permanent magnet (AFPM) and linear electric machines were compared, and the rotary machine topology was identified to meet all the project requirements.

Therefore, three promising design variants of the rotary topology were further analyzed in Subtask 2.C1.1, and the analysis results are presented to identify the most promising design variant. It is found, through analytical sizing, that the single rotor-single stator design variant outperforms the other design variants. Optimization results indicate that it can potentially meet all the project requirements.

To improve model accuracy, FEA analysis was also performed using material models updated from experimental electrical steel characterization data acquired in Subtask 2.C1.4 and compared with the FEA results using models for the same materials in the FEA tool's library (provided by the material manufacturer). The results indicate that the electric machine can potentially meet the project requirements. Other analyses performed on the optimal design were i) impact of using segmented magnets, and ii) impact of using a solid rotor yoke. The results are briefly presented below:

a) **Analytical sizing and comparison of electric machine design variants:** Our analysis has shown that the single rotor AFPM design variant outperforms the coreless machine and the yokeless and segmented armature (YASA) machine. The 3D rendering of the design variants compared are shown in Fig. 2.C8. Using the analytical sizing equation, the design variants were compared at different slot-pole combinations using two practically important metrics a) Gravimetric power density and b) Rotor moment of inertia and the results are shown in Fig. 2.C9. A detailed presentation of these results is provided in [6]. It is seen that machines with larger number of slots (Q) and pole pairs (p) offer higher gravimetric power density and lower moment of inertia, and the single rotor machine outperforms the other two design variants. Therefore a single rotor design with p=8 pole pairs, Q = 24 stator slots was selected for further analysis.

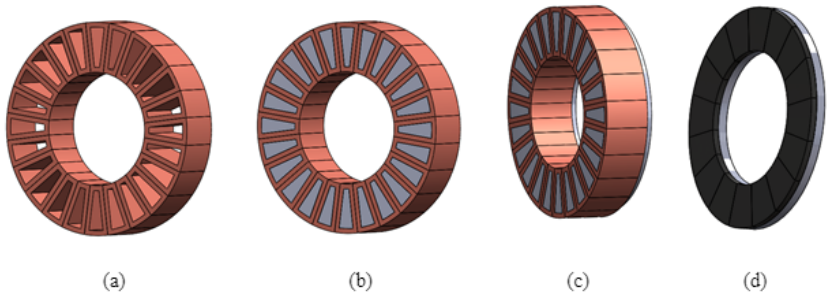

Figure 2.C8: Electric machine design variants: (a) Coreless stator; (b) YASA stator; (c) Single rotor-stator; (d) PM rotor (Common for all designs).

[6] F. Nishanth, A. Khamitov, and E. L. Severson, "Comparison of linear and rotary electric machine topologies for a hybrid hydraulic electric architecture of off-highway vehicles," in 2020 IEEE Transportation Electrification Conference and Expo (ITEC), Chicago, IL, 2020, pp. 1–6.

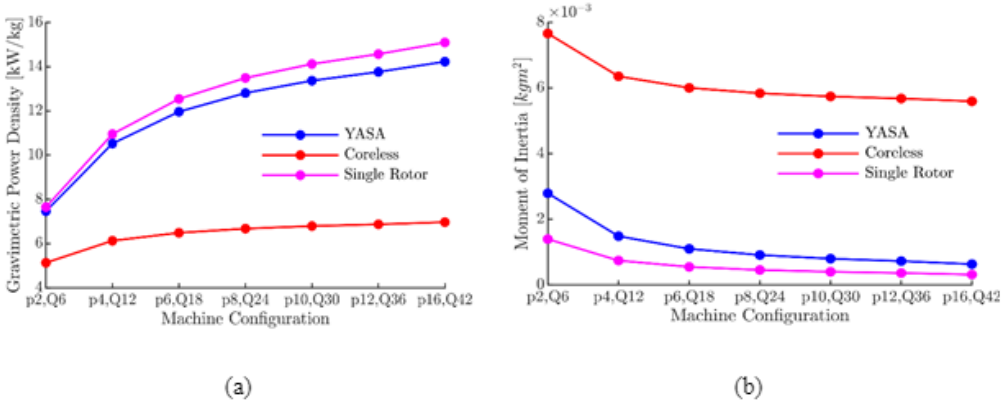

Figure 2.C9: Performance comparison [4]: (a) Gravimetric power density (Higher is better); (b) Rotor moment of inertia (lower is better). The horizontal axis shows the number of rotor pole pairs (p) and stator slots (Q). For example p4Q12 is an 8 pole (4 pole pair), 12 slot design.

b) Design optimization of the single rotor machine: An FEA based design optimization study was performed on the single rotor axial flux machine, with objectives of maximizing the power density, efficiency, and minimizing the torque ripple. A computationally efficient 2D FEA technique, used in [2] was used for design evaluation. The 2D projections of pareto fronts from the final generation of the optimization run are shown in Fig. 2.C10.

The optimization results clearly show that the single rotor AFPM machine can potentially achieve power densities well beyond 9.5 kW/kg and several pareto optimal electric machine designs achieve efficiencies over 95%, indicating a high potential to meet the project requirements (integrated system power density > 5kW/kg and efficiency > 85%).

A design with a power density of 10.5 kW/kg and efficiency of 96 % was selected for further analysis. This design has an active material cost of 5.5 $/kW, clearly offering enough headroom to remain within the target cost (<20 $/kW) for the electrical system (motor + power electronics). An exploded view of the selected design is shown in Fig. 2.C11.

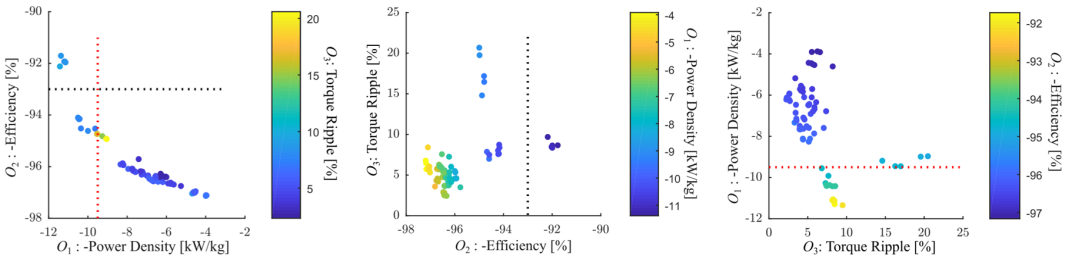

Figure 2.C10: Pareto front projected onto different 2D surfaces. The dotted lines indicate the electric machine power density and efficiency values to potentially meet the project targets.

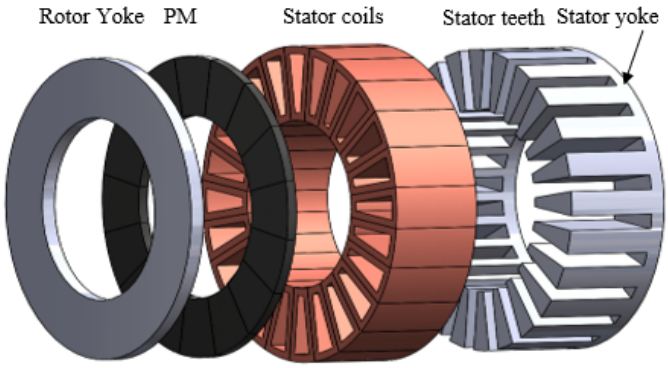

Figure 2.C11: Exploded view of the selected p=8, Q=24 single rotor machine design

c) **Investigation of magnet segmentation:** This analysis indicates that machine efficiency can be improved by segmenting the magnets. To accurately determine the effects of magnet segmentation, the selected design was analyzed using 3D FEA. Two 3D FEA models of the optimal machine, the first using unsegmented magnets and the second using segmented magnets were analyzed and the results are reported in Table 2.C3. It is evident that the segmented magnets reduce the total magnet losses by approximately 45%. The reduced losses are extremely desirable from system efficiency, thermal management, and magnet selection standpoints (elevated temperatures due to higher losses can demagnetize NdFeB magnets). Segmentation also permits replacing large custom made magnets (expensive) with smaller, commercially available magnets (comparatively inexpensive)

Table 2.C3: Magnet loss comparison

Pole structure	**Total magnet losses [W]**
Unsegmented	255
Segmented	138

d) **Impact of using a solid rotor yoke:** A rotor yoke is typically constructed with electrical steel laminations. However, at operating speeds of 15,000 RPM, it is challenging to ensure the structural integrity of the tape wound rotor yoke (a lamination stack cannot be used for an AFPM). Hence, a solid steel rotor yoke was considered. Two 3D FEA models of the optimal design were created, one of which used a rotor yoke made of tape wound electrical steel (Arnon 5) while the other used a solid steel rotor yoke. The rotor yoke losses computed from FEA are listed in Table 2.C4. The rotor yoke losses increase by approximately 30W when a solid rotor yoke is used. At the 20kW output power level, the additional losses in the solid rotor yoke would result in a 0.1% reduction in efficiency, which can be overlooked considering the advantages of better structural integrity and ease of fabrication.

Table 2.C4: Rotor yoke loss comparison

Rotor yoke	Rotor yoke loss [W]
Tape wound Arnon 5	20
Solid steel	49

e) **Axial forces:** The single rotor machine inherently has unbalanced axial forces due to attraction between the rotor magnets and the stator core, whereas in the double rotor variants, these forces are canceled by the symmetry of having equal and opposite forces on each side of the stator. The average force over one rotor rotation for the selected single rotor design is 775 N, which must be supported by the bearings of the machine. It is estimated that this force is modest compared to the expected bearing ratings, and therefore is not viewed as being particularly problematic.

f) **FEA analysis using updated material models from Subtask 2.C1.4:** FEA analysis of the optimal motor design with experimentally tuned material models from subtask 2.C1.4 has been performed. The performance of the optimal design when using three different experimentally characterized electrical steel materials (Arnon 5, Arnon 4, M-19 29Ga) and the default material property (available in the FEA tool for Arnon 5 from the manufacturer) is compared. It is found that the FEA models utilizing experimentally obtained material characteristics show significantly lower efficiencies compared to the default model. Model 3 with M-19 29Ga teeth had the lowest efficiency among all models. This is primarily due to the thicker M-19 29Ga laminations having higher losses at operating frequencies of this machine (2kHz). The ultra-thin gauge steels (Arnon 4 and Arnon 5) have similar performance as both have similar lamination thickness. However, Arnon 4, being a thinner lamination than Arnon 5, has marginally lower losses than Arnon 5. It can be concluded that the ultra-thin gauge laminations are preferable for our application.

The loss breakdown of the models are graphically displayed in Fig. 2.C12. The majority of losses (~ 70%) in all the models (irrespective of electrical steel used) is in the stator teeth and coils. This is an important input for designing the thermal management system. More on this will be explored using the multiphysics optimization framework developed in Subtask C2.2.

Conclusions:

- The single rotor AFPM design variant best meets the project requirements on gravimetric power density, efficiency, and cost among the axial flux machine variants considered.
- Using segmented magnets can offer efficiency improvements by reducing eddy current losses, and cost benefits by permitting use of commercially available magnets (custom magnets otherwise needed are expensive).
- The marginal reduction in efficiency due to using a solid rotor yoke can be overlooked for the benefits it offers in retaining structural integrity and relative ease of fabrication.
- The unbalanced axial forces in a single rotor AFPM are minimal compared to the bearing ratings and are not viewed as being problematic
- Accuracy of FEA models can be improved using experimentally tuned material models.

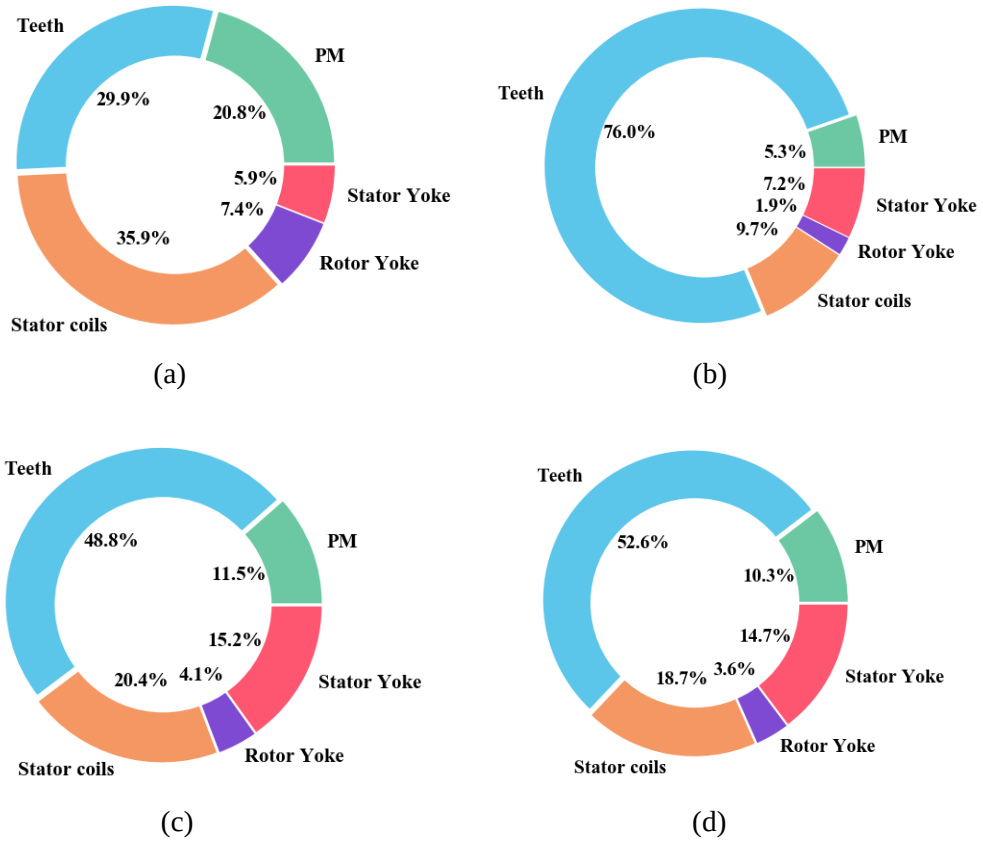

Figure 2.C12: Loss breakdown for (a) Default model; (b) Model 1; (c) Model 2; (d) Model 3.

Milestone 2.2 - Hydraulic subsystem analysis

Hydraulic subsystem model for the radial ball piston pump/motor was extensively analyzed in BP1. In BP2, experiments were performed on a commercial unit to validate the initial analytical model. Several improvements have been made to the model as a result of the experimental validation step. These include: temperature effect of leakage; uncentered piston ball; heat transfer; and hydrodynamic lubrication. The most significant finding is that at high speed, the piston ball of the radial ball piston pump will not stay in the center of the bore. The eccentricity will greatly increase the friction and leakage losses, thus making the design not possible to reach the efficiency. Having discovered this issue, an alternate piston design - in the form of cylindrical piston, was proposed and analyzed, and is expected to meet the desired efficiency.

Task 2.C2: Develop multiphysics optimization framework

This task involves developing a multiphysics framework to optimize the integrated hydraulic-electric machine. The multiphysics framework was created in the MATLAB environment and evaluates the hydraulic pump, electric motor, and thermal management system. The framework involves iterating design generation, evaluation and optimization.

It was decided that there are not many parameters that are coupled between the hydraulic subsystem and the electric one. The main system wide parameters were the maximum speed and the geometric constraint of fitting the hydraulic machine inside the electric one. Therefore, the optimization of the hydraulic and electrical subsystems could be done relatively separately.

Since the hydraulic optimization runs much faster than the electrical one, as a part of the optimization framework, a lookup table of Pareto optimal hydraulic system designs was created. The speed and number of pistons are chosen in the electric motor optimization to pick which hydraulic design to couple with the electric one. This lookup table (Tab 2.C5) allows an optimal hydraulic design to be precomputed for the electric motor optimization and ensures that the designs can be integrated together.

Table 2.C5: Optimized Hydraulic Designs

	7 Pistons	**9 Pistons**	**11 Pistons**
5000 RPM	Ploss = 276.43W Eff = 95.50% Rcam = 5.99 cm	Ploss = 284.58W Eff = 95.57% Rcam = 9.11 cm	Ploss = 462.48W Eff = 92.44% Rcam = 9.09 cm
7500 RPM	Ploss = 354.20W Eff = 94.37% Rcam = 5.46 cm	Ploss = 383.95W Eff = 94.11% Rcam = 7.73 cm	Ploss = 390.33W Eff = 94.14% Rcam = 6.10 cm
10000 RPM	Ploss = 431.37W Eff = 93.27% Rcam = 5.25 cm	Ploss = 644.30W Eff = 89.22% Rcam = 6.51 cm	Ploss = 498.26W Eff = 92.64% Rcam = 7.62 cm
12500 RPM	Ploss = 575.34W Eff = 91.07% Rcam = 6.36 cm	Ploss = 541.46W Eff = 92.00% Rcam = 5.91 cm	Ploss = 551.08W Eff = 91.97% Rcam = 5.72 cm
15000 RPM	Ploss = 645.65W Eff = 90.15% Rcam = 6.35 cm	Ploss = 648.27W Eff = 90.07% Rcam = 5.81 cm	Ploss = 648.00W Eff = 90.58% Rcam = 5.61 cm

Task 2.C3: Explore the design space of the optimization framework

This task involves using the multi-physics optimization framework developed in Task 2.C2 to explore the design space of the integrated hydraulic-electric machine. The project targets a power density over 5kW/kg, efficiency over 85% and cost under 20 $/kW for the entire system comprising the pump, motor, and the power electronics. As power electronics is not a part of the multi-physics framework, suitable assumptions were made based on past experience and published hardware test data. From the assumed power electronics power density, efficiency, and cost, it was determined that the remaining HECM components (pump + motor) must have a power density over 6.2 kW/kg, efficiency over 86.7% and cost under 15$/kW to meet the project requirements. The optimization results for the Pareto front designs for these combined components are plotted against the project objectives of power density, efficiency, and cost in Fig. 2.C13.

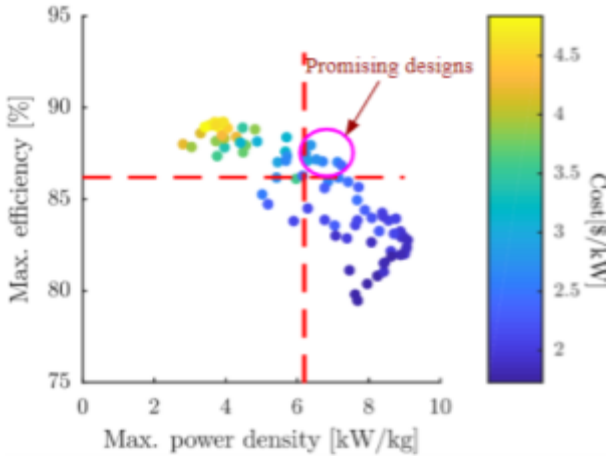

Fig. 2.C13: Project objectives for Pareto front designs - with indication of promising designs.

We now provide some details of this design optimization process. The multi-physics optimization framework developed in subtask 2.C2 is used to explore the design space of the integrated hydraulic-electric machine. The flow chart for design evaluation in the multi-physics optimization framework is shown in Fig. 2.C14.

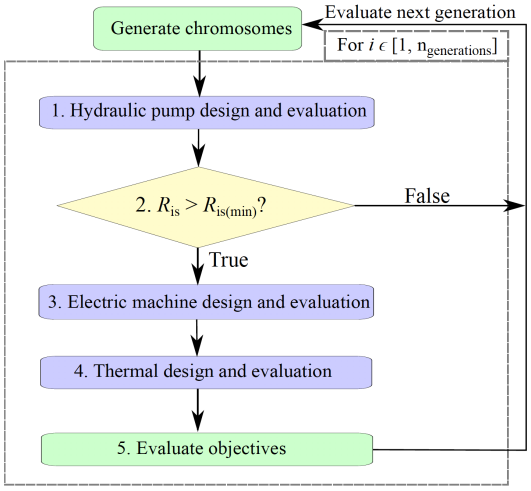

Figure 2.C14: Flow chart of the multiphysics optimization framework

Initial optimization attempts considered designs with maximum rotational speeds from 5,000 RPM through 15,000 RPM. In these results it was observed that only designs with maximum rotational speeds higher than 10,000 RPM were able to meet the project target on power density. For this reason, subsequent optimization efforts focused on maximum operating speeds between 10,000 RPM and 15,000 RPM. It was observed that the designs with higher maximum operating speeds tended to be more power dense, while designs with lower maximum operating speeds tended to be more efficient.

The project targets a power density over 5kW/kg, efficiency over 85% and cost under 20 $/kW for the entire HECM system comprising the pump, motor, and the power electronics. As power electronics are not included in the multi-physics framework, reasonable values for power density, efficiency, and cost were assumed based on past experience and published hardware test data. From the assumed power electronics power density, efficiency, and cost, it was determined that the remaining

HECM components (pump + motor) must have a power density over 6.2 kW/kg, efficiency over 86.7%, and cost under 15$/kW to meet the project requirements.

The Pareto front versus optimization objectives and how these Pareto front designs perform with respect to the project power density, efficiency, and cost targets are provided in Fig. 2.C15.

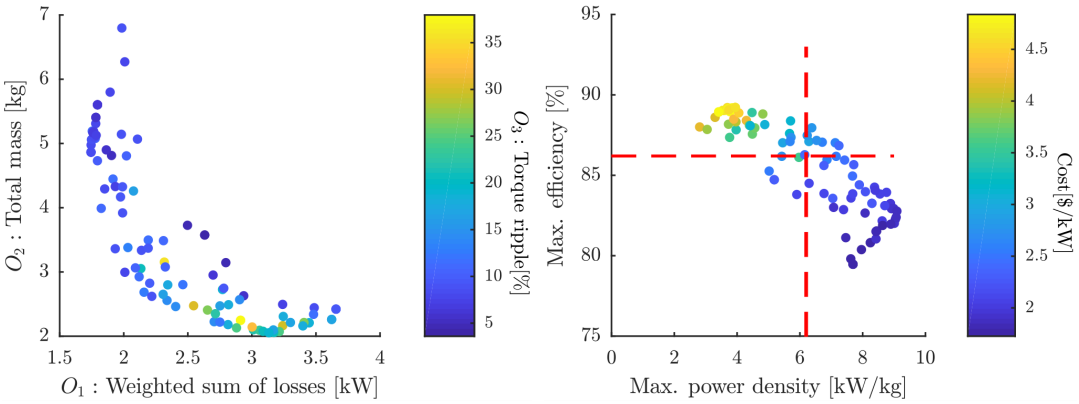

Figure 2.C15: Pareto front designs plotted against the optimization objectives

The performance targets for the HECM (pump + motor) are indicated by the dashed red lines. It is evident that the efficiency and the power density show a trade-off relation and that several designs are able to meet the project targets. The optimization free variable distribution for the Pareto front designs is shown in Fig. 2.C16. The free variable bounds set for the optimization are indicated by red horizontal lines. It can be observed that the free variables are distributed well within the bounds.

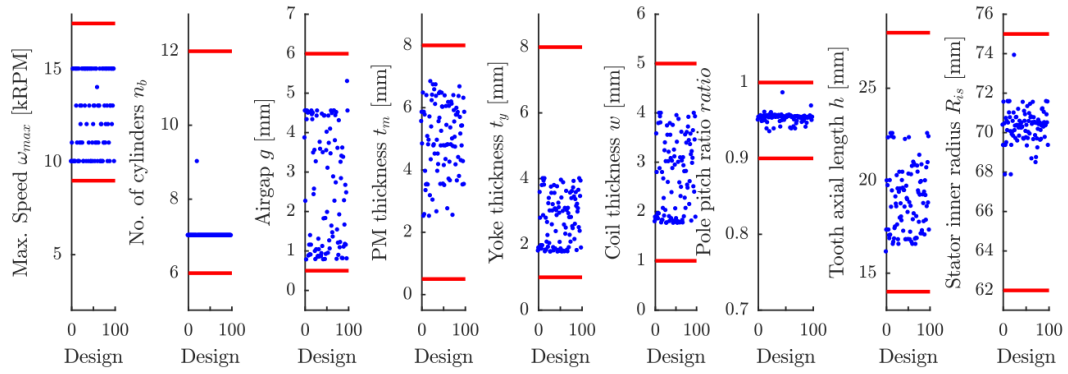

Figure 2.C16: Free variable distribution

The electric machine power density and efficiency are plotted against the maximum operating speed in Fig. 2.C17. It is observed that electric machines in several HECM designs have power densities in excess of 10 kW/kg, which is the range reported in literature for high performance electric machines.

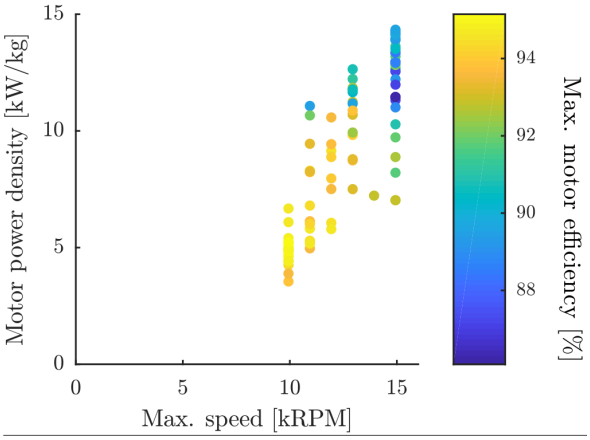

Figure 2.C17: Electric machine power density and efficiency v/s operating speed

A candidate design that best meets the project targets has been selected for detailed design, prototype and experimentation.

Milestone 2.3: Design space explored

With the completion of task 2.C3: Explore design space, Milestone 2.3 is also complete. We review the key findings here.

Milestone 2.3 requires the design space of the HECM (hydraulic pump + electric machine) to be explored using a multi-physics optimization framework. Therefore, completion of Tasks 2.C2 (developing of the multi-physics optimization framework) and 2.C3 (explore design space) also completes this milestone. This exploration has led to various design changes as well as a set of design parameters expected to meet power density, efficiency and cost requirements. These main points can be noted:

- The design of HECMs must navigate design trade-off between high power density and efficiency
- The increased efficiency of HECMs designed for low rotational speeds is due to reduced pump losses and iron losses in the electric machine.
- HECMs designed for high rotational speeds are more power dense. This is due to increased power density of the electric machine at higher operating speeds, as observed in Fig. 2.C15.
- HECMs designed for maximum rotational speeds between 11,000 RPM and 13,000 RPM showed the most promise to meet the project objectives of power density and efficiency. Designs with speeds greater than 13,000 RPM featured high power density, but failed to meet the efficiency targets.
- Refined hydraulic loss model indicates that the radial ball piston design would incur significant friction and leakage losses at high operating speed and no parameters can avoid this situation. As a consequence, the design was transitioned to radial cylindrical pistons instead.
- Exploration of the thermal model suggests that at low speed, there will not be enough leakage flow for heat transfer. This prompted an alternate design that utilizes an external source of oil supply through the stator-cam gap to create a short oil flow path between the stator-teeth. This has been shown to improve cooling performance at the low speed drastically.

Task 2.C4: Create detailed final design of the prototype

A candidate design that meets the project objectives was identified from the multi-physics optimization results presented in Fig. 2.C13. Fig. 2.C18 shows the CAD model of the design.

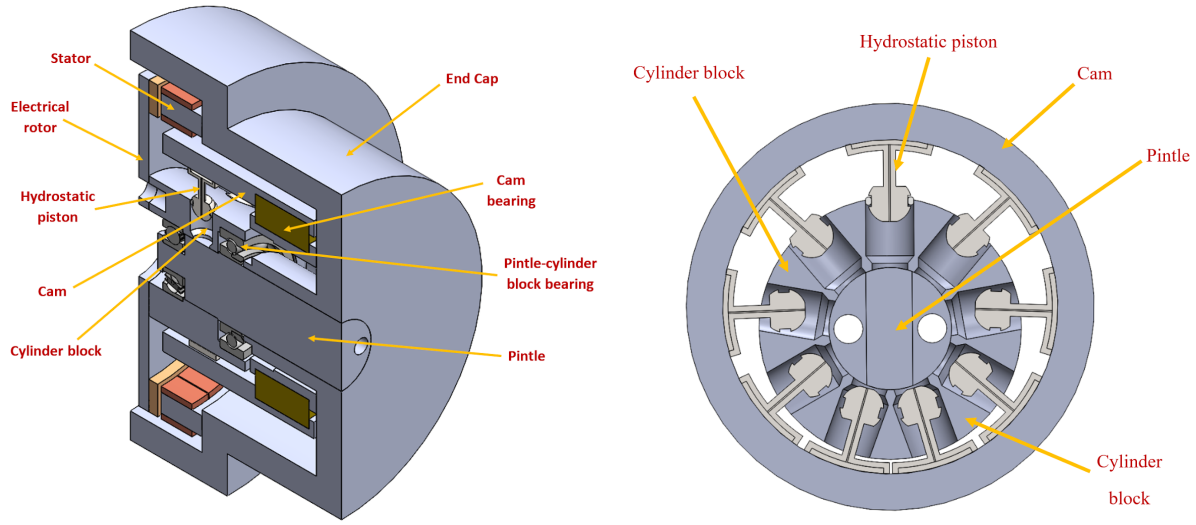

Figure 2.C18: CAD model of the integrated electric motor and cylindrical piston pump.

The materials used for different electrical components and hydraulic components are listed in Table 2.C6.

Table 2.C6: a) Electrical components with materials used in the integrated machine

Component	**Material**
Permanent magnets	NdFeB (N45)
Rotor yoke	Electric Steel
Stator yoke and teeth	Tape wound Arnon 5 (3% Si steel)
Windings	18AWG Copper wire

b) Hydraulic components with materials used in the integrated machine

Component	**Material**
Pintle	4340 Steel
Cylinder Block	4340 Steel
Cam	4340 Steel (hardened)
Piston	6061-T6 Al
Piston Slipper	Brass

Detailed drawings were made for the hydraulic and electrical parts to be fabricated. Some of the drawings are shown in Fig. 2.C19 for the electric machine parts and Fig. 2.C20 for the hydraulic parts. The dimensions of the components along with dimensional tolerances are indicated in these drawings.

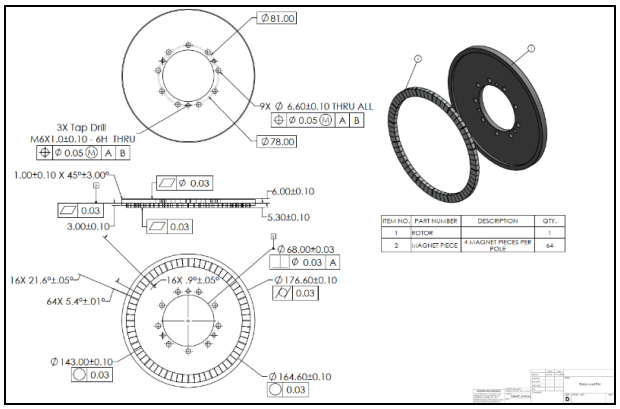

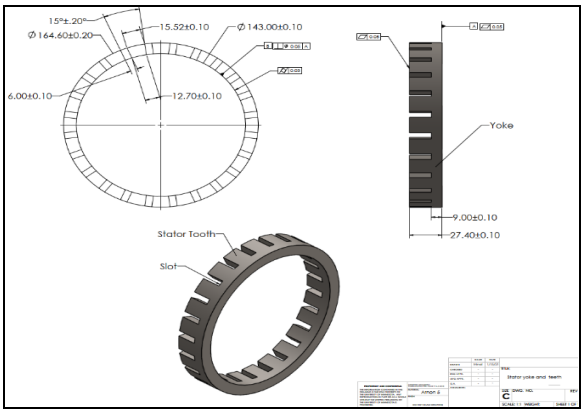

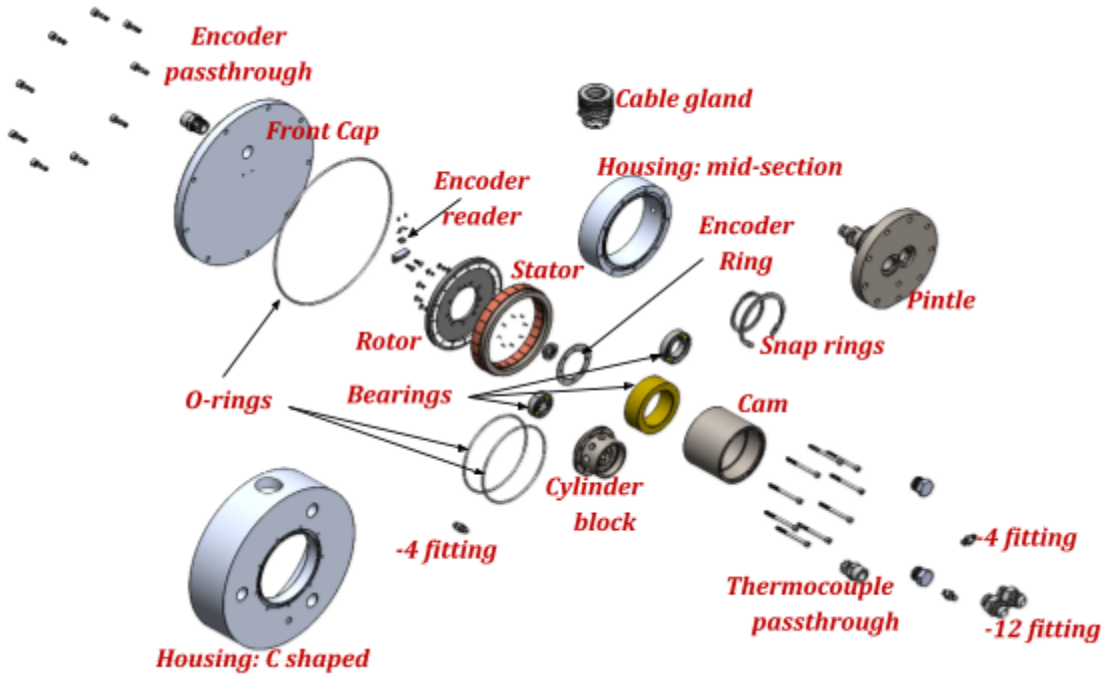

Fig. 2.C19: Electric machine parts: (a - left) Rotor; (b -right) Stator; (c - bottom) Exploded view of the prototype design

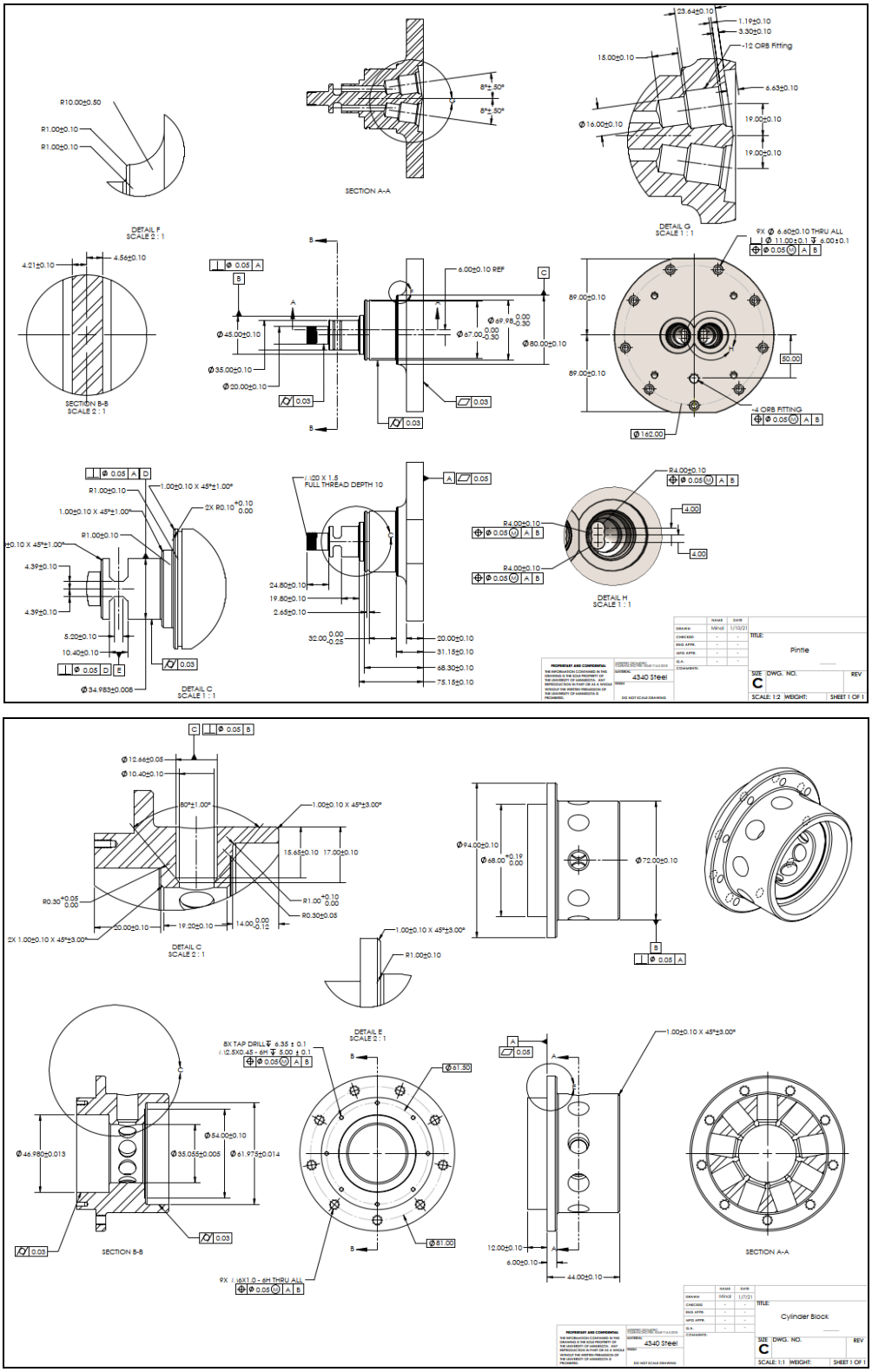

Fig. 2.C20: Hydraulic components: (a) Pintle; (b) Cylinder block.

Milestone 2-4: Prototype design: This milestone requires that detailed designs of the prototype be created. A candidate design that met the project objectives was identified from the multi-physics optimization results and details of the integrated system were refined as a part of Task 2.C4. The complete prototype design includes the electric machine components, the hydraulic components, and the auxiliary components. Some example drawings are shown above. This milestone is complete.

BP2 - Go/No-Go Performance Metric Demonstration

The criteria for the BP2 Go/No-Go decision consists of 3 preliminary validations:

1) At least one target platform verified with high fidelity simulation
2) HECM control strategy verified in Hardware-in-the-loop (HIL) experiment
3) Detailed analysis of integrated HECM predicts gravimetric power density of 5kW/kg and conversion efficiency of 85%.

Criteria 1: At least one target platform verified with high fidelity simulation

The target efficiency/energy saving requirement is that at least one representative platform has an efficiency (ratio of positive output work to engine output) of at least 65% or an energy saving compared to the baseline load sensing architecture of at least 40%. In BP2, various Pareto optimal analysis on a wheel-loader, a 5-ton mini-excavator, and a 22-ton excavator have consistently shown efficiency and energy saving above this requirement. High fidelity simulation performed for the wheel-loader shows that efficiency defined as positive output work to input energy is 93.7% compared to 46.6% for the baseline. Thus, this go/no-go criterion is satisfied.

Criteria 2: HECM control strategy verified in Hardware-in-loop setup

Control experiments have been conducted on the 200 bar HIL testbed. Using the control strategy of the nominal controller being a passivity based, backstepping controller, and the transition controller being a least norm feedforward controller, the position tracking control performance with or with pressure rail switches are small. The maximum error is 4mm but in most cases, the error is less than 1mm. This level of accuracy is acceptable.

Criteria 3: Detailed analysis of integrated HECM predicts gravimetric power density 5kW/kg and conversion efficiency of 85%

In BP1 it was shown that a coreless axial flux machine with two rotors can just meet these targets. Task 2.C1 showed that the single rotor axial flux machine variant shows promise to offer significant power density improvements over the coreless axial flux machine. So, the electric machine design was updated to the single rotor variant. The project targets a power density over 5kW/kg, efficiency over 85% and cost under 20 $/kW for the entire system comprising the pump, motor, and the power electronics. As power electronics are not a part of the multi-physics framework, suitable assumptions were made based on past experience, and the HECM (hydraulic pump + electric machine) performance targets were found to be gravimetric power density over 6.2 kW/kg, efficiency over 86.7% and cost under 15$/kW to meet the project requirements. A multi-physics optimization framework was developed in Task 2.C2 and used in Task 2.C3 to optimize the integrated HECM based on the single rotor axial flux machine. For accurate performance prediction, the optimization relied on high-fidelity FEA models for the electric machine. Results in Fig. 2.C13 indicate several promising HECM designs that meet the requirements of gravimetric power density (>5kW/kg), efficiency (>85%), and cost. The detailed design of the prototype is based on one of these designs and is therefore expected to meet these requirements. The detailed design of this integrated electric-hydraulic machine has been completed. It will be constructed in BP3.

3. Budget Period 3 (BP-3) Technical Progress

Budget Period 3 spans the 29th-44th months (16 months) of the project, from January 1, 2021 to April 30, 2022. The main focus of Thrust A is to explore interactions between thrusts and further refine the analysis of the energy saving potentials. Thrust B focuses on testing the control on a high pressure (300+bar) HIL experimental platform. In Thrust C, a prototype of an integrated electric-hydraulic machine is constructed and characterized.

3.1 Thrust A - Energy Saving

Task 3.A1 - Evaluate Effect of Controller on Energy Saving

The effect of the controller on energy saving has already been partially evaluated with the high fidelity simulation conducted in Task 2.A2 as validation of the energy-saving potential of HHEA. There, the nominal backstepping controller was already used to track the OEM provided duty cycle. The high fidelity simulation has demonstrated over 50% energy saving and a positive work to engine output ratio (i.e. an efficiency measure) of 94%, satisfying the project goal. Throttling loss due to valve switching was included in the simulation although it was not included in the optimization phase of the static energy saving analysis when the pressure rails were selected. To conclude the evaluation of the effect of the controller on energy saving, the high fidelity simulation is updated to use a controller that utilizes both the nominal backstepping controller and the transition least norm controller for dealing the rail transition events. In addition, the valve coefficient of the switching valves is reduced by 12 times (i.e. more throttling is expected) to understand how valve sizing affects energy usage.

Figure 3.A1 shows the difference in control performance with and without the transition controller in high fidelity simulation. Notice that the maximum error has been reduced from 8 mm to 1 mm with the use of the transition control, which is consistent with our previous analysis. From the energy use perspective, reducing the control valve size by 12 times decreases the positive work to input energy ratio from 94% to 86%. This indicates a tradeoff between cost and efficiency. The use of the transition controller increases energy consumption by 0.9% from 775kJ to 782kJ, which is fairly insignificant.

In summary, if switching valves are sized and operated appropriately and switching losses are considered in the energy analysis, the effect of the controller on energy saving is minimal.

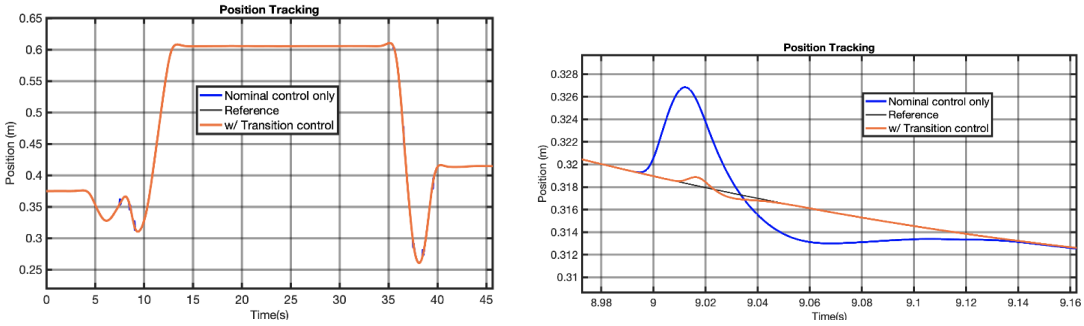

Fig. 3.A1: Tracking control performance with and without transition controller (Left: zoom in)

Milestone MA 7: Controller effects on energy saving evaluated:

- With the above results, this milestone is 100% complete.

Task 3.A2 - Evaluate Effect of Integrated HECM on Energy Saving

The goal of this task is to understand how the integrated hydraulic pump/motor and electric machine, being developed in Thrust C, intended to be used with the Hydraulic-Electric Control Module (HECM) would impact the efficiency of the system. A study was conducted comparing the old pump map for a 107cc conventional bent-axis pump motor from the literature and an electric machine with 90% efficiency that are discretely combined, with the new map for the integrated electric-hydraulic machine modeled in Thrust C. The study involved evaluation of our dynamic programming optimization algorithm, which is able to incorporate switching losses (to be described later) into the cost function. Two optimizations were conducted, each on the CNH wheel loader short cycle. The new pump was used as the HECM pumps, while the main pump is still a scaled old 107 cc pump motor.

In the past, we have sampled the drive cycle every 100 milliseconds and constructed the cost matrices from this sampled drive cycle. Now, the cost matrices are constructed by considering the most finely sampled drive cycle, constructing a cost matrix, then summing entries appropriately so that the cost matrix includes entries which reflect losses over a period of 100 milliseconds. The time 100 milliseconds was chosen because that is how quickly our switching valves can reasonably actuate.

The old and new maps are shown in Fig. 3.A2 which shows that the integrated component generally has a higher efficiency.

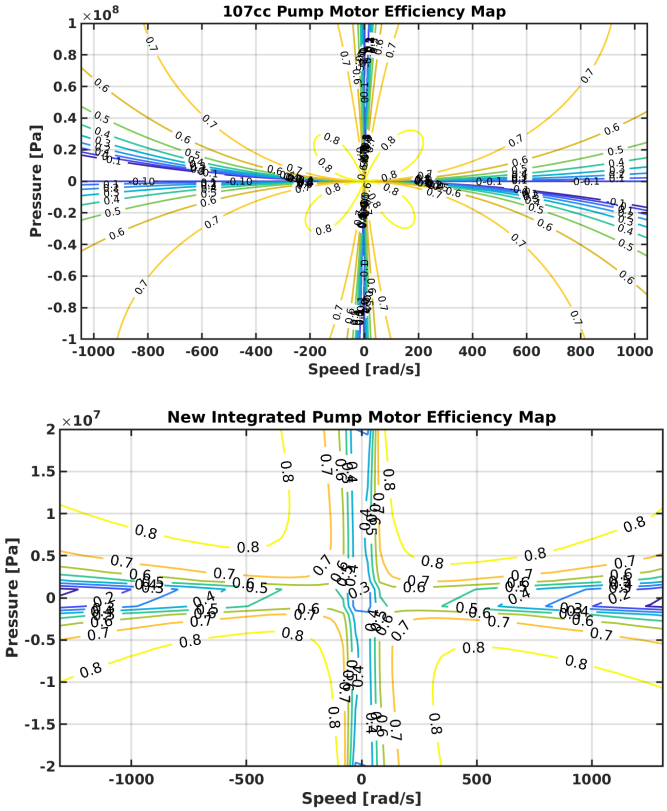

Fig. 3.A2: Efficiency contours of hydraulic pump/motor - electric machine: (Top) - old map for the conventional hydraulic pump/motor and electric motor; (Bottom) -New map for the Integrated Hydraulic Pump/Motor & Electric Machine

Fig. 3.A3 shows the energy input and consumption pie chart when throttling loss at the switching valves are neglected. It shows that the ratio of positive output work to input work from the engine has increased from 97% to 112%. As a reference, this ratio for the baseline load-sensing system is 42%. The energy reduction is due to the reduction in losses within the HECM by 55%.

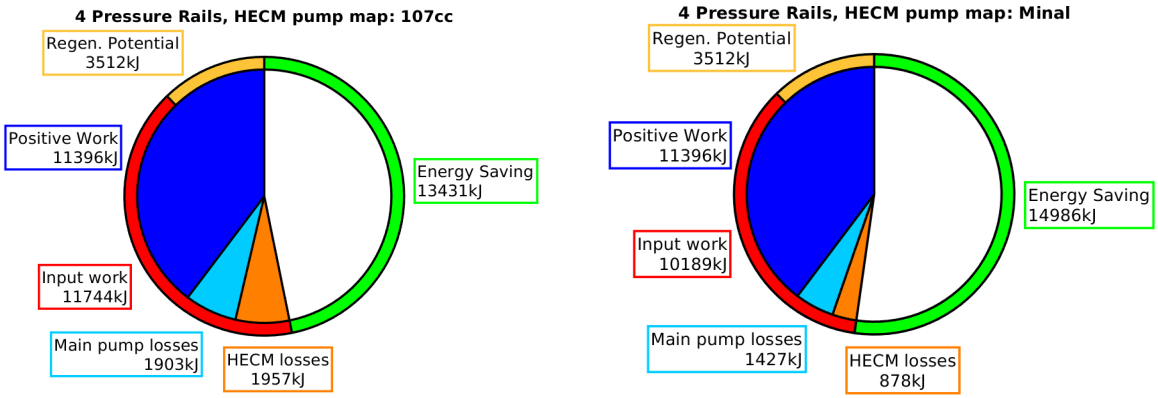

Fig 3.A3: Energy input and consumption for a wheel-loader neglecting throttling losses. (Left): Using the conventional bent-axis pump/motor and electric machine. (Right): Using the proposed integrated electric motor - hydraulic pump.

Fig. 3.A4 shows the comparison when the throttling losses are also included in the optimization. Similar trends are observed. The ratio of positive output work to input work has increased from 84% to 93%. The HECM losses are also reduced by 55%. Interestingly, when switching losses are included, the pressure rail selections when the more efficient HECM is used result in 20% higher throttling losses which offsets a portion of the reduced HECM losses.

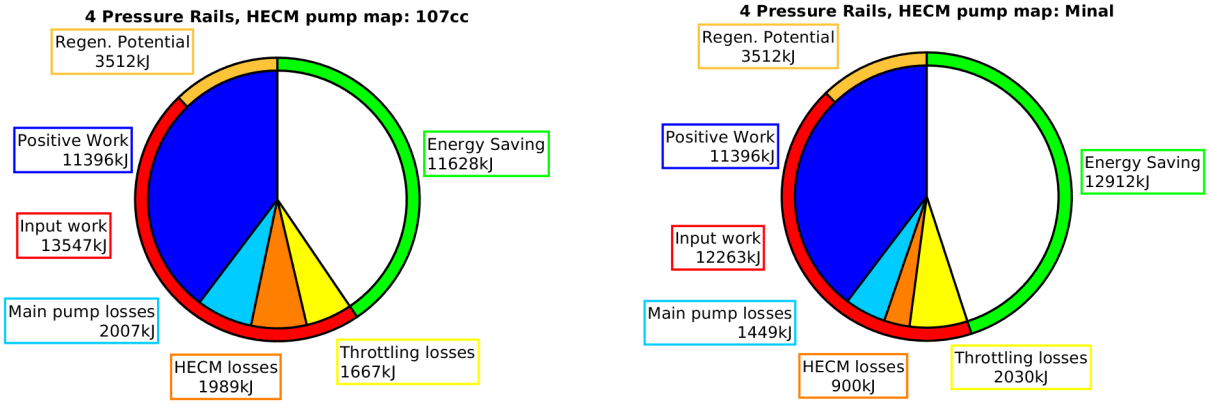

Fig 3.A4: Energy input and consumption for a wheel-loader *with consideration of throttling losses*. (Left): Using the conventional bent-axis pump/motor and electric machine. (Right): Using the proposed integrated electric motor - hydraulic pump.

Figs. 3.A5-A6 show the operating points of the HECM with the conventional pump/motor and electric machines and the integrated machine respectively. Notice that with the integrated machine, the operating points are such that the machine speeds are much higher. This results in the electric motor torque being lower.

In summary, we expect that the integrated HECM hydraulic-electric machine will save an additional 10-15% of energy over conventional bent-axis pump/motor and off-the-shelf electric machine.

A benefit that is not captured by this comparison is that the integrated machine is also much more compact than the conventional discrete machines.

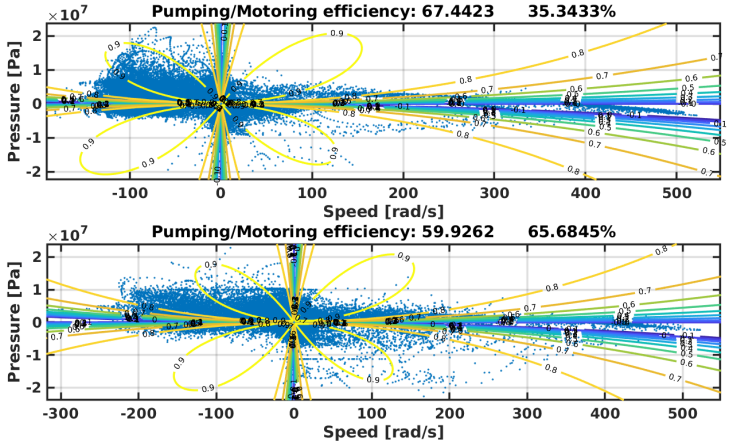

Fig 3.A5: HECM operating points & efficiency of the conventional discrete hydraulic and electric machine

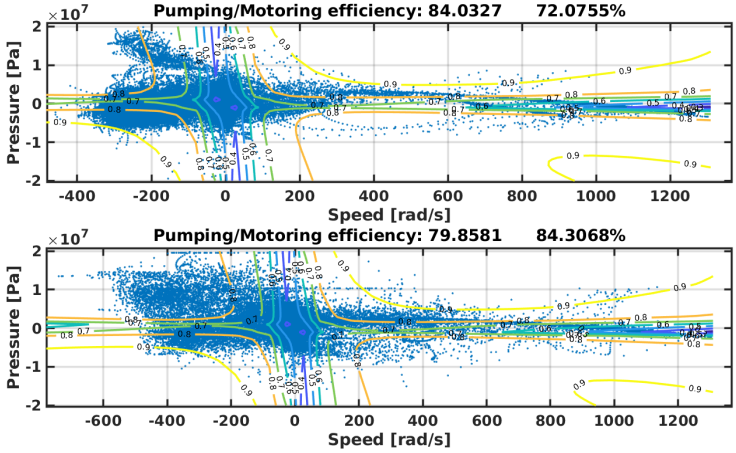

Fig 3.A6: HECM operating points & efficiency of the integrated hydraulic-electric machine

In addition to the two tasks specified above, Thrust A has provided more detailed analysis of 1) pressure rail switching loss; and 2) accumulator sizes. These are described below.

Incorporating switching losses into energy-saving optimization

In the early phase of the project, the energy-saving analysis tool did not take into account the throttling losses through the switching valves during pressure rails switching events when optimizing the pressure rail decisions. Only if the valves are large and valve transition times are very short throttling losses during switching can be negligible. While the losses can be added back on to evaluate the impact of the switching losses, the pressure rail selections that neglect switching losses will no longer be optimal. A major upgrade of the optimization algorithm is to take switching losses into consideration. The details can be found in [10]. The procedure is briefly described here.

When switching occurs from one pressure rail and another, the valve connected to the previously connected rail has to be closed and the valve connected to the rail to be switched to has to be opened (see Fig. 3.A7).

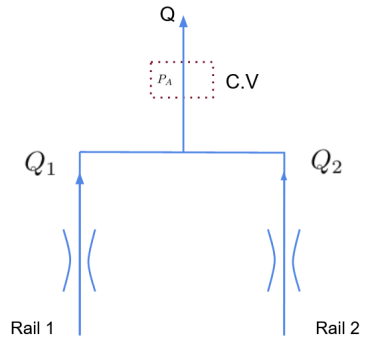

Figure 3.A7: Parameters defining pressure change at valve outlet

The effect of switching on energy saving analysis and optimization can be addressed in two phases.

- In the first phase, switching losses are added to the optimized rail selections that do not take into account switching losses.
- In the second phase, the switching losses are incorporated into rail selection optimization as well. This will generate rail switching sequences that are optimal.

Developing a switching loss map

In both phases, we need to quantify the energy losses associated with each pressure rail switch in an easy to use way. To do this, we create a dynamic model taking into account the valve dynamics, valve delay (between closing a valve and opening another), actuator flow requirements, chamber volume, fluid compressibility, and pressure dynamics within that volume. The model is then simulated to obtain the total energy losses for each combination of scenarios. The energy losses for the different scenarios are stored as a map that can then be interrogated. For example, the pressure dynamics are simulated with flow determined by the valve opening the flow demands:

$$\dot{P}_{out}(t) = \frac{\beta}{V}(Q_1(t) + Q_2(t) - Q_{out})$$

where, P_{out} is the pressure at the outlet of the valve, Q_1 and Q_2 are the flows associated with the two rails between which the switch happens, Q_{out} is the flow demanded at the outlet of the valve, $V$is the volume at the outlet of the valve and βis the bulk modulus of the working fluid. Furthermore, the rail flows are given by:

$$Q_i(t) = k_i x_i(t)\text{sgn}(\Delta P_i)\sqrt{|\Delta P_i|} \text{ for i} = \{1,2\}$$

where, k_i is the ratio of the maximum flow rating for the i^{th}inlet port and the allowable pressure drop across the valve at that flow rate, $x_i(t)$is the fraction of orifice that is open for the i^{th}inlet port and $\Delta P_i$is the pressure difference between the rail pressure and the outlet pressure.

For a certain representation of valve spool dynamics and k_i ratio, a switching loss "map" could be obtained for a range of outlet flows for all the different switches possible for the HHEA. For example, for a HHEA with 3 CPRs, there were 6=3x(3-1) different unique switches possible.

Figure 3.A8 (Left) shows the trajectories of orifice opening/closing for a valve defined by a second order underdamped transfer function with a damping coefficient of 0.8. Notice that there is a delay of 13ms between one inlet port starting to close and the other inlet port starting to open. This minimizes the undesired cross-port flows. Figure 3.A8 (right) shows how the outlet pressure varies if such a valve is used for a switch from a rail at 35MPa to a rail at 17.5MPa.

With the valve dynamics defined, the switching losses were calculated by:

$$E_{Loss} = \int_0^{t_f} (Q_1 \Delta P_1 + Q_2 \Delta P_2) dt$$

Figure 3.A9 shows a switching loss "map" for the valve parameters defined above which helps us find the energy lost due to switching between two pressure rails for a range of outlet flows.

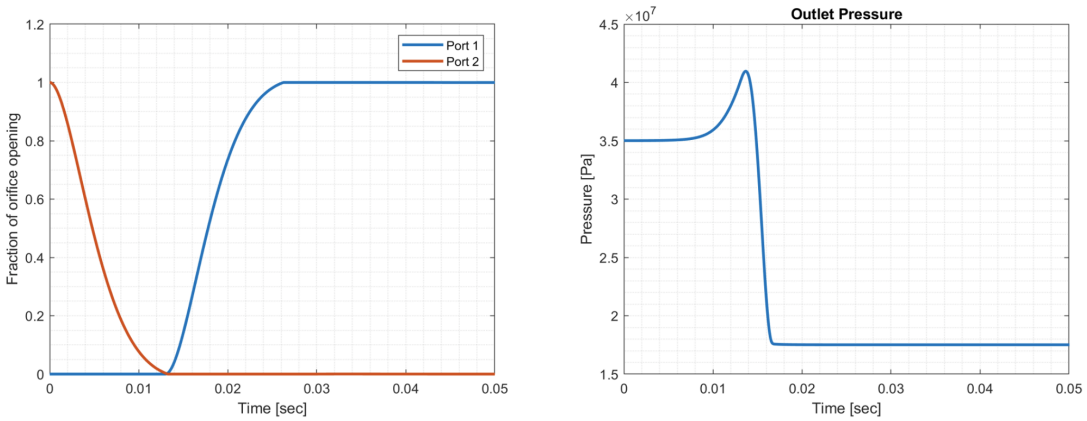

Figure 3.A8: (Left) the fraction of orifice open for a switch from Port 2 to Port 1. (Right) Variation in the outlet pressure for a switch from 35MPa to 17.5MPa.

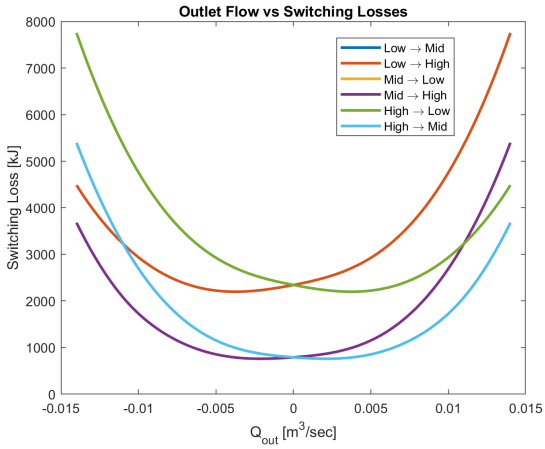

Figure 3.A9: Switching losses for a range of outlet flows for different Rail switches.

The switching loss model has also been validated by comparing it with the results from the high fidelity model for a range of switches. In Fig. 3.A10, we can see that the switching loss model agrees with the results from the high fidelity model. The small deviations can be attributed to factors such as the loss model assuming a constant bulk modulus while the high fidelity model uses a pressure dependent bulk modulus.

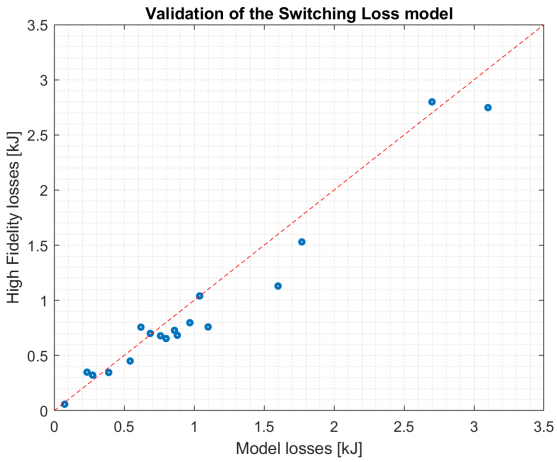

Figure 3.A10: Validating the switching loss model

This map was used to calculate and add back the switching losses for the optimal trajectories generated by optimal control / energy saving analysis tool which minimized the energy losses associated with the HECM units and the Main Pump connected to the rails but not switching losses.

Optimal control with consideration of switching losses

Beside not being optimal, another limitation of this method of adding back the switching losses without considering the switching losses when determining the rail selections is that the rail trajectories that result may involve a lot of frequent switches. Figure 3.A11 shows a small section of the drive cycle where the hydraulic force being provided via the pressure rails changes frequently. This frequent switching is not very practical, since the valves cannot switch instantaneously and switching losses are incurred. Thus, a method to make rail selections that also avoid the frequent rail switching while also minimizing the net energy lost in the system was desired.

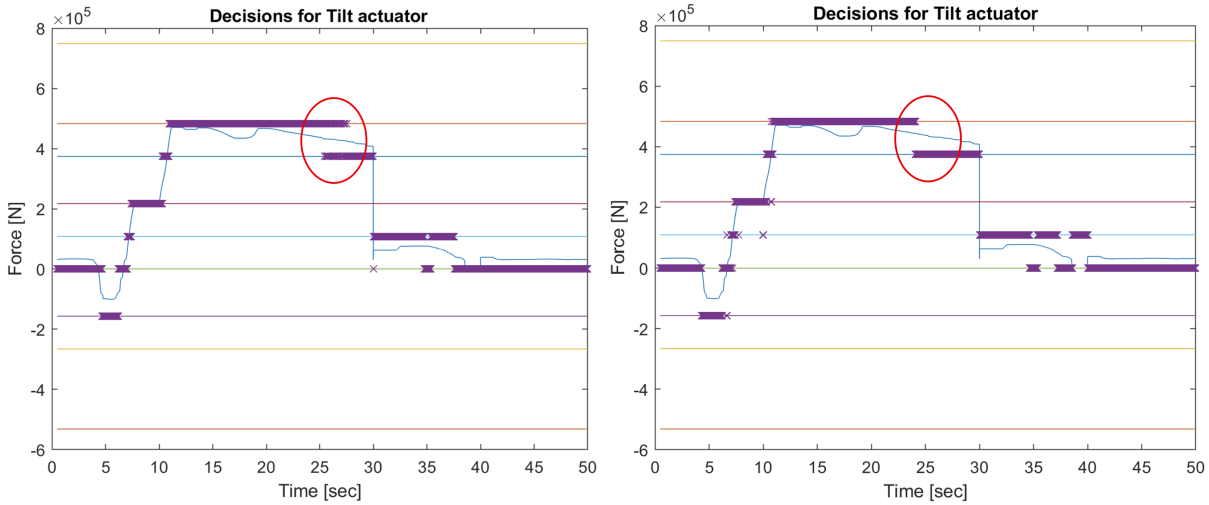

Figure 3.A11: Hydraulic force level selections for a section of the drive cycle. Left: without consideration of switching losses, and Right: with consideration of switching losses. The red circle shows a section of frequent switching (left) and that it is avoided (right).

In order to prevent frequent switching between pressure rails, the energy losses associated with switching need to be incorporated into the optimization algorithm. By penalizing the energy loss due to rail switching, it is expected that the frequent switches would be reduced.

The HECM losses and the main pump losses are dependent on the operating points of the HECM components and the main pump at each instant. However, the switching loss is dependent on the current rail selection and the next rail selection. Because of the coupling between the present rail switch and future rail switches, optimization via the Lagrange multiplier method only (method used in BP1 and BP2) does not apply here. The new optimal control problem is solved using a combination of inner loop dynamic programming and outer loop gradient flow for selecting the Lagrange multiplier instead. Figure 4 shows the hydraulic force provided by the rails for this new trajectory (see [10] for details).

As seen Fig. 3.A11 (right), with this modified optimal control, the trajectory reduces the frequent switching of the valve. The total number of valve switches is reduced by 14% when compared to the original optimal control problem.

With the decrease in the number of switches, the energy characteristics of the system when simulated with this new optimal trajectory can be compared to the energy characteristics for the original optimal trajectory. For the “original” trajectory, switching losses are added back in after the pressure rails were selected without accounting for switching losses. Table 3.A1 shows this comparison for the drive cycle of a wheel-loader assumed to have a HHEA with 3 CPRs (rails at 0 MPa, 17.5 MPa and 35 MPa).

Table 3.A1: Comparison of energy distribution for the original algorithm and the modified algorithm

Distribution of Input Energy	Original Algorithm	Modified Algorithm
Positive Work [kJ]	4260	4260
HECM Loss [kJ]	645	800
Main Pump Loss [kJ]	377	290
Switching Loss [kJ]	652	545
Total [kJ]	5934	5895

The decrease in the number of switches also results in a 16% decrease in switching losses and 23% main pump losses but at the expense of higher HECM losses. This results in the total input energy requirement for the trajectory generated by the algorithm as only slightly lower than that of the original algorithm (2.3%).

The energy-saving results for the various machines have been updated with the new algorithm that incorporates switching losses. With the incorporation of switching losses, the energy savings, compared to the baseline load sensing system, are reduced slightly (by 2-3%):

20-ton wheel loader:
SC cycle: No switching loss: 54%; with switching loss: 51.7%
LC cycle: No switching loss: 63%; with switching loss: 60%

22-ton excavator:
Trenching cycle: No switching loss: 69%; with switching loss: 67%

Accumulator size estimation

The Hybrid Hydraulic-Electric Architecture (HHEA) utilizes an accumulator for each common pressure rail. Previously, the accumulators were simply assumed to be “large enough”. Here, an algorithm was developed to find the minimum required accumulator size for each drive cycle.

It is assumed that in the architecture (Fig. 3.A12), a fixed displacement pump operating at a fixed speed was used to fill the accumulators. The inlet and outlet of the pump can be connected to any of the common pressure rails via switching valves. Switches were allowed to occur periodically (e.g. T_s =200 milliseconds). The flow demand from each rail is assumed to be known from the energy-saving potential optimization algorithm. The accumulators are assumed to be the gas charged type as shown in Fig. 3.A13 and the gas expansion/compression process is assumed to follow a polytropic relationship (i.e. PV^{γ} = constant).

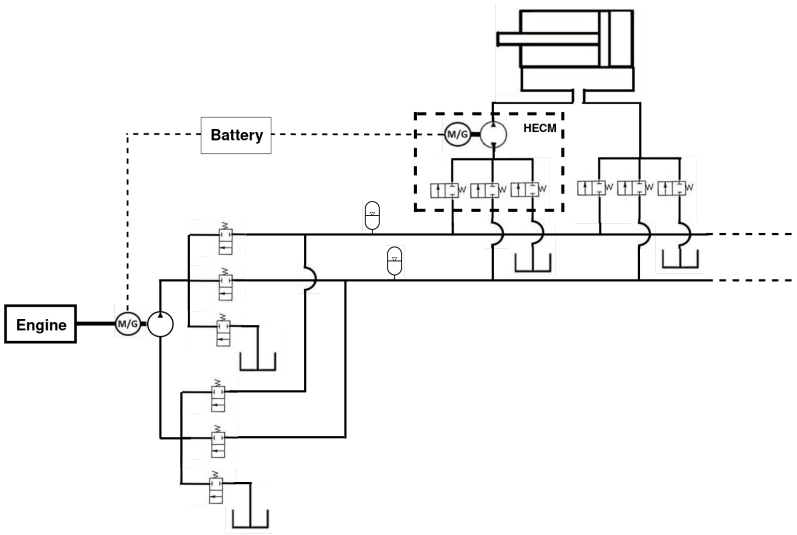

Fig. 3.A12: Railing Filling Architecture

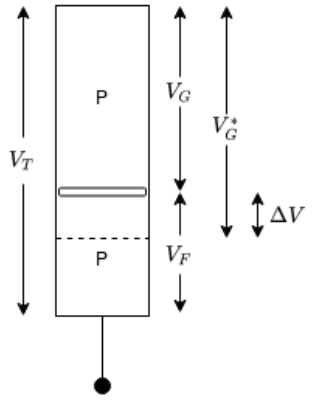

Fig. 3.A13: A gas charged accumulator

A dynamic programming (DP) algorithm is used to determine which rails should be connected to the rail filling pump's inlet and outlet to minimize the accumulators' total size. As the accumulators are charged and discharged, the pressure deviates from the nominal pressure. A constraint is placed on the optimization such that the pressure deviation is within a given limit (e.g. 10%). Deciding which common pressure rails to connect to the actuator at a given point in the drive cycle results in flow in and out of each rail's accumulator. This algorithm finds an optimal way to fill these accumulators so that the pressure in each rail does not deviate too far from its desired value.

Fig. 3.A14 shows the minimum total (of two) accumulator sizes for a 3 common pressure rail systems HHEA (designed for a 22 ton excavator executing a trenching operation) with various pump flow rates. At each valve switching period T_s , there is an optimal pump flow rate that would minimize the sum of the accumulator sizes. Also, increasing T_s requires larger accumulators. It is also found the accumulator size is about 25% smaller if the gas charging/discharging process is isothermal instead of adiabatic.

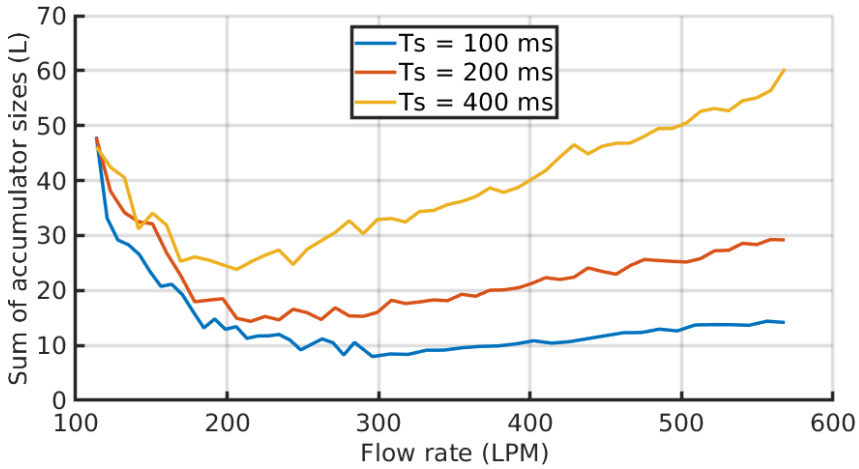

Fig. 3.A14:Minimum total size of the two accumulators for various pump flow rate and valve decision period for a 22 ton excavator executing a trenching duty cycle. The pressure was required to be within 10% of Prail , and volume changes were assumed to be adiabatic.

Sample flow volumes in and out of the accumulators (rail flow demand and filling) for a 22-ton excavator performing the trenching operation with Ts = 200ms are shown in Fig. 3.A15. Note that the rail filling algorithm aims to match the filling flow with the flow demand of the pressurized pressure rail. The closer that they match, the smaller the accumulators.

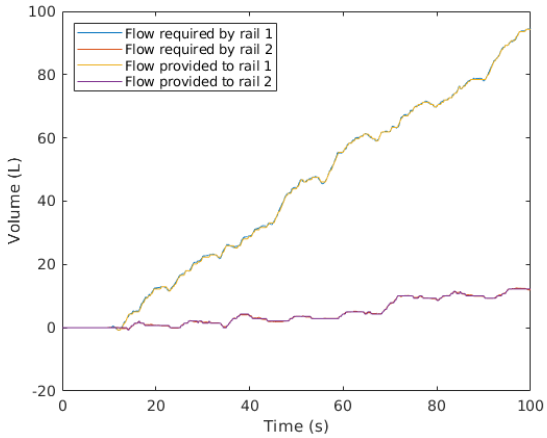

Fig. 3.A15: Flow volume demanded and filled (as determined by the DP algorithm) for each pressurized pressure rail. “Flow required by rail _” refers to flow out of the accumulator as a result of actuator motion. “Flow provided to rail _” refers to flow from the main pump, as determined by the dynamic programming algorithm. The difference is accommodated by the accumulator.

For a 3 rail HHEA, the total sizes of the 2 required accumulators (on the two pressurized rails, the tank rail does not require an accumulator) for the 3 types of machine conducting various drive cycles are:

- 22 ton excavator - 20 L of total volume.
- 20-ton wheel loader - 10 L of total volume.
- 5-ton excavator - 5 L of total volume.

For details of this topic, please see [11].

3.2 Thrust B - Control Performance

The main tasks in BP3 for the control performance thrust are:

Task 3.B1 - Verify control strategy on high-pressure test-stand (300+ bar):

- This involves designing and constructing a high pressure (350 bar) HIL testbed and testing the control algorithm on the test bed. The testbed was to be constructed at the Eaton (later Danfoss) facility in Eden Prairie, MN.

Task 3.B2 - Verify control strategy with the integrated HECM

- This involves evaluating the suitability of the integrated electric-hydraulic machine prototype being developed in Thrust C for control.

Other tasks involve adjustment and improvement of the control algorithms.

Controller modification

While the high pressure HIL testbed was being constructed, the controller was refined and improved using the medium pressure HIL testbed at the University of Minnesota that was constructed in BP2. To speed up the control design simulation process, the high fidelity simulation model that was initially implemented on AMESim was translated into Matlab/Simulink. This allows the researchers at the University to conduct high fidelity simulation without the AMESim software (that only Eaton has a license). A high level view of the model is shown in Fig. 3.B1.

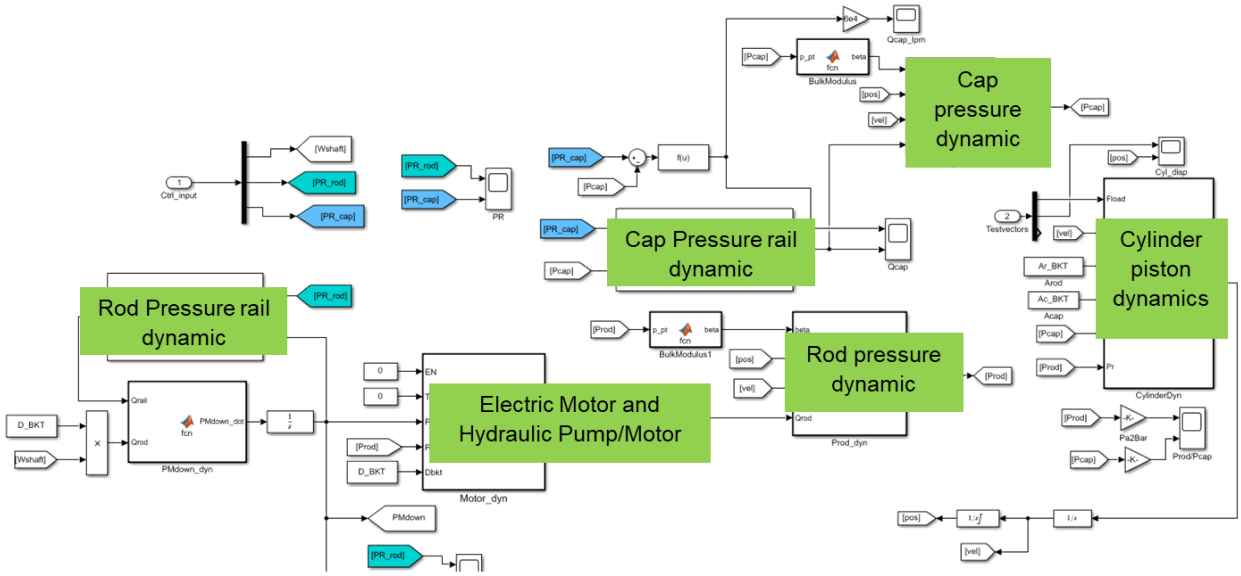

Figure 3.B1: High Fidelity mode of the HECM with one actuator in Simulink

The Matlab/Simulink model has been used to evaluate control performance and compared with LMS AMESim. The same trajectory used in the BP2 high fidelity validation task was re-used here. The trajectory was originally extracted from a duty cycle data collected experimentally from a tilt actuator on a wheel loader. Similar tracking performances are obtained from the Simulink only model compared to the AMESim model.

Adjustments to the controller implementation consists of the following:

a) Inner speed control loop: The controller was modified to utilize an inner electric motor speed control loop, and an outer loop nominal and transition controller that use desired motor speed as input. This configuration is intended to improve the robustness due to uncertain electric motor characteristics if we had used torque input to the electric motor directly as the controller input. The inner loop motor speed control, which is a P-I with feedfoward controller, is a substitute for the speed control loop provided by the motor manufacturer used in previous testing.

The reconfigured controller was first tested for a fast-sinusoidal trajectory tracking under a nominal case where a constant load force was applied. The maximum error is 0.6mm as it can be seen in Fig. 3.B2 and it occurs when the cylinder is changing direction (i.e. error is dominated by unknown friction).

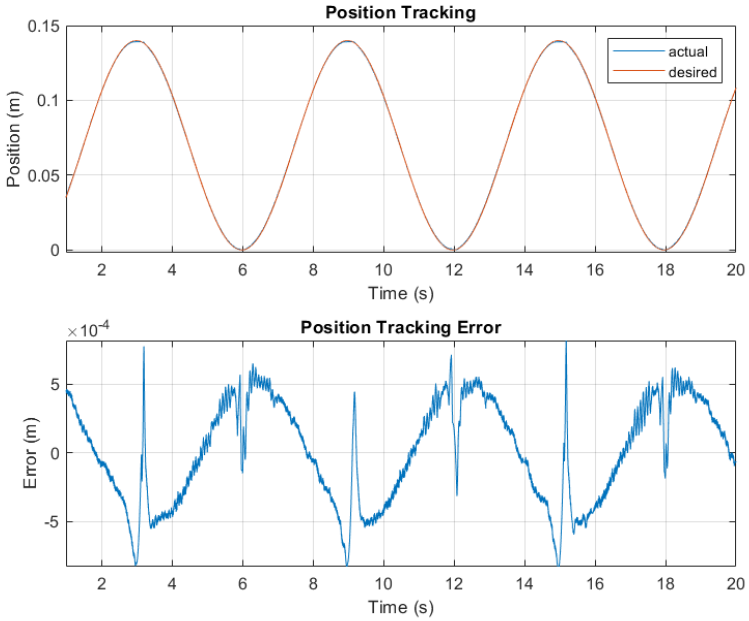

Fig 3.B2: Trajectory tracking for sinusoidal using the inner speed control loop

The reconfigured controller was used to test the tracking performance with a scaled version of a OEM provided duty cycle. Previously, the test trajectories were prototype ramp or sinusoidal trajectories. In addition, an error deadband of 0.2mm was added to the controller to prevent the controller from responding to unrealistically small errors.

Trajectory tracking results for the nominal condition where a constant load force is applied and no rail switching are required are shown in Fig. 3.B3. The maximum error is 1.1 mm and the majority of the trajectory tracking error is under 0.5 mm.

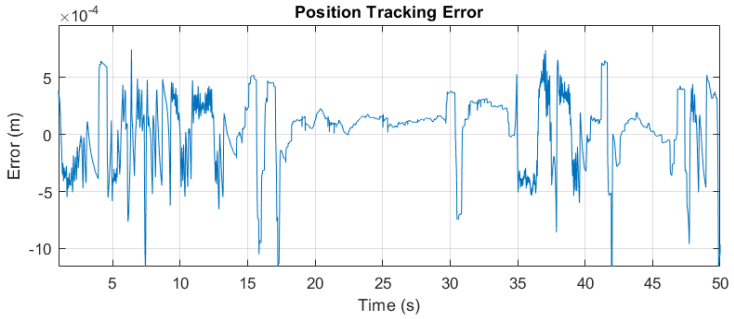

Fig 3B.3: Scaled wheel loader trajectory tracking with constant load force and no rail switching

b) Real-time rail-switching strategy: In order to test the arbitrary drive cycles provided by the OEM, we need to generate rail switching decisions in real time. To facilitate rapid control testing, it is inconvenient to determine the rail switchings using the separate off-line energy saving algorithm. Instead, we have created a generalized (not necessarily optimal) real time rail switching strategy based on the current load force. In this strategy, the absolute difference of all the rail forces and the duty cycle force are calculated and the corresponding force rail that does not cavitate and presents the smallest difference is chosen. In this way, the force provided by the pressure rails would be close to the current load and the required torque from the HECM electric motor will be minimized. Based on this, the closing and opening sequences and the desired status of each of the 6 switching valves are determined.

Testing results for a scaled duty cycle for a wheel loader are shown in Figs. 3.B4-3.B6. Fig. 3.B4 shows that the duty cycle load force can be faithfully emulated by the HIL testbed.

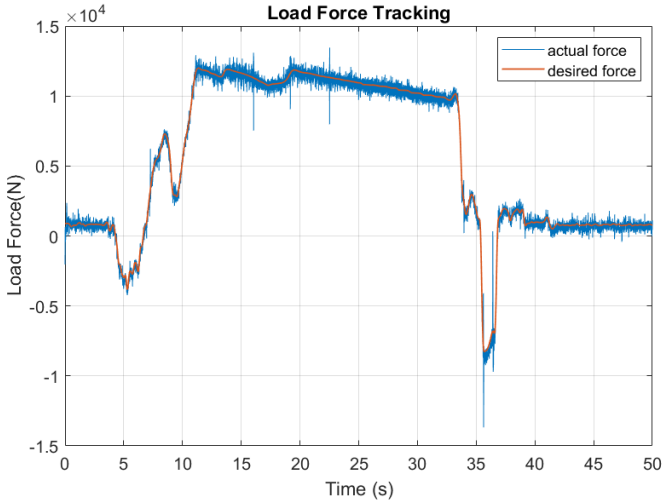

Fig 3B.4: Load force tracking on the HIL testbed

Fig. 3.B5 illustrates the execution of the real-time rail switching strategy through the duty cycle with multiple rail switchings.

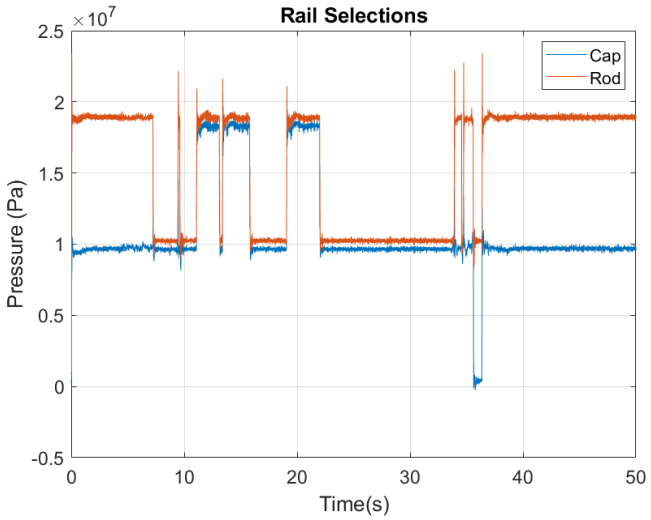

Fig 3.B5: Pressure rail selections

Figure 3.B6 shows the tracking control results using the nominal (backstepping) control only. The maximum error is 11 mm. As can be seen, the large errors occur at the pressure rail transition events and between rail transitions, the tracking error is less than 1mm.

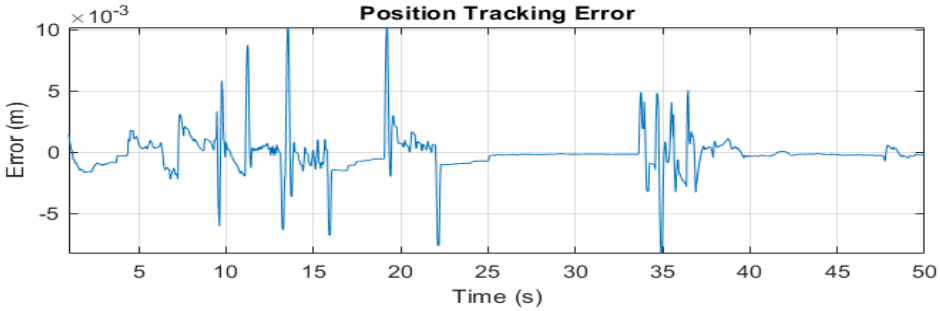

Fig. 3.B6 Position Tracking performance with *only the nominal backstepping* controller

The open-loop least norm transition control was tested next. Fig. 3.B7 shows that the maximum error has been reduced substantially. The maximum error was 3.8 mm which occurs at one switching instant and the errors at other switchings are typically at or below 2mm.

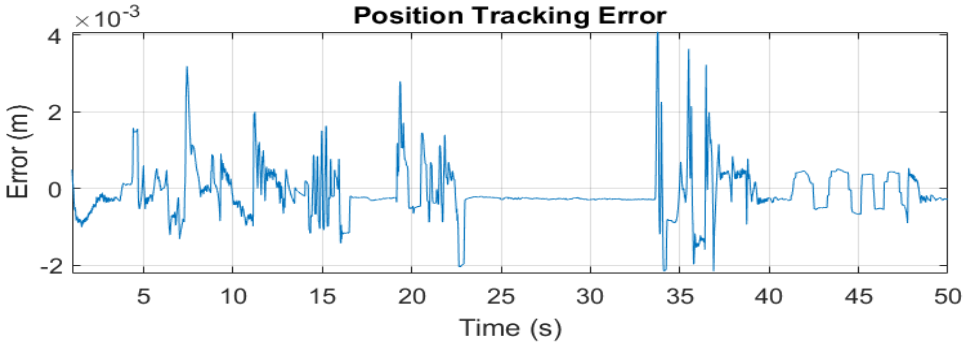

Fig 3.B7 Position Tracking performance of backstepping with transition control

***Task 3.B1 - Verify control strategy on high-pressure test-stand (300+ bar)*:**

300+ bar testbed construction

a) Test Stand Design and Hardware Selection:

The design of a high-pressure Hardware-In-the-Loop (HIL) test stand is finalized and shown in Fig. 3.B8. It consists mainly of an actuator cylinder coupled mechanically to a load cylinder, a variable displacement pump connected to an electrical motor, two proportional flow-control valves (PFV), and Eaton's CMA90 electro-hydraulic control valves as denoted by CV-1 and PV1 – PV5. The load cylinder emulates the external loading to the actuator from the test vectors. Eaton's 72400 servo-controlled variable displacement piston pump with 49 cubic-centimeters (cc) total displacement is selected as the hydraulic pump. The pump is modified to facilitate a four-quadrant operation and the axis is mechanically coupled to a 5kW electric motor, as per HECM design. The pump's inlet is connected to the HECM pressure rail and the pump's outlet is used to control the actuator cylinder's motion. During testing however, the pump displacement will be fixed, where the variability on the displacement will be used to accommodate different test-vectors.

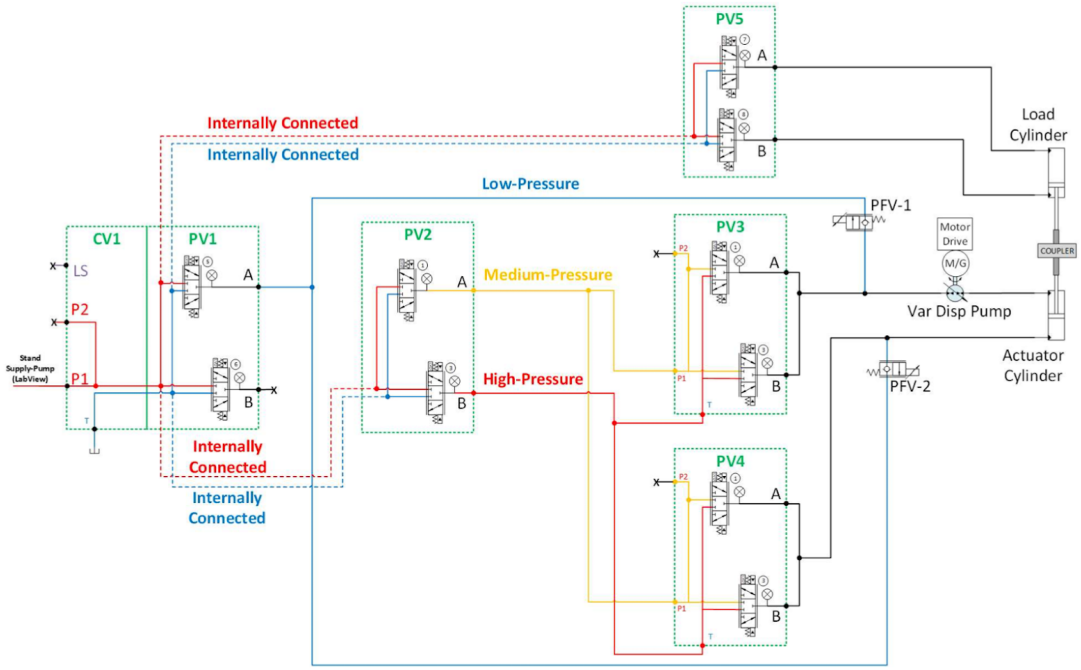

Fig. 3.B8: Schematic of the high pressure (300bar+) HIL testbed

CMA90 electro-hydraulic control valve is selected to control hydraulic pressures on the bench due to its compact and modular design, which also provide independent meter-in and meter-out capability by leveraging integrated pressure and spool position sensors and on-board electronics. The CMA valve system consists of an inlet control module CV1 that is connected to a hydraulic pressure source that controls a common inlet pressure for the work sections, denoted by PV1-PV5. Each PV section consists of a pair of three-position three-way valves, denoted by A and B, which controls the outlet pressures or flows independently. Reference pressures or flow for a specific PV section can be sent to CMA90 via

CAN J1939 communication protocols from a controller. The two proportional flow-control valves (PFV-1 and PFV-2) are utilized as On-Off valves and are controlled via analog inputs.

The three common rail pressures are controlled via PV1-A, PV2-A and PV2-B respectively. These controlled rail pressures are connected to the inlet of the variable displacement pump through six On-Off valves, namely PFV-1 (Rod-Low), PFV-2 (Cap-Low), PV3-A (Rod-Med), PV3-B (Rod-High), PV4-A (Cap-Med) and PV4-B (Cap-High). Note that PV3 and PV4 sections of the CMA are utilized as On-Off valves. The load cylinder Cap and Rod pressures are controlled by PV5-A and PV5-B. The whole setup is designed to be fitted within a 3-feet by 6-feet bench top.

b) Development of Digital Twin of HIL Test Stand

A digital twin of the HIL test stand was developed to help facilitate the actual hardware tests in a safe and efficient simulation environment. The main objectives are to (1) define the inputs and outputs (I/O) to and from the test-bench, and to streamline these I/O across the University of MN and Eaton teams, (2) design and validate a set of safe lab test vectors, and (3) to retire technical risks on motion control before the HIL tests are conducted. To this end, a co-simulation environment was developed where the HECM test stand is simulated in AMEsim™ while the control strategies and test vectors are defined in MATLAB Simulink™.

The test vectors consist of the external load force to the actuator cylinder, actuator cylinder position and actuator cylinder speed. The inputs to the HECM are the rail selections (High/Medium/Low pressure rail) for Cap-side and Rod-side for the actuator cylinder and the electrical motor torque. The feedback from the HECM test stand plant model are the actual position and speed of the actuator cylinder, the head and rod pressures of the actuator cylinder, the inlet pressure of the hydraulic pump and the actual speed of the electrical motor. Simulation is conducted with an actual duty cycle of a tilt actuator from an 18-ton CNH821E wheel loader. Parameters such as cylinder and pump sizes from the actual wheel loader are utilized. Actual test vectors for lab tests were designed with these criteria:

- Cylinder extension under passive load (up to 300 bar).
- Cylinder retraction under passive load (up to 300 bar);
- Cylinder extension under over-run load (low power).
- Cylinder extension under over-center load.
- Scaled duty cycle trajectory tracking from real vehicle duty cycle data.

c) Construction and commissioning of the 300 bar HIL teststand

The construction of the high-pressure Hardware-in-the-loop control test-stand at the Danfoss (previously Eaton) Eden Prairie facility was delayed due to delay in the execution of the subaward contract after Eaton Hydraulics was purchased by Danfoss. The test bed was completed and commissioned in Q15. Fig. 3.B9 shows the completed test-stand.

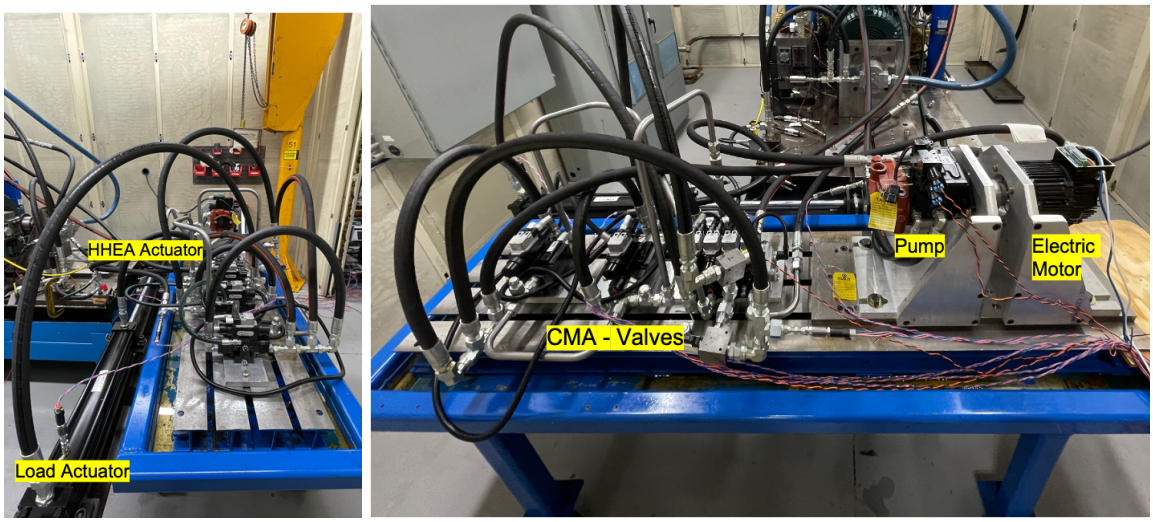

***Fig 3.B9**: High pressure (300+bar) test-stand for the HHEA*

Commissioning of the high-pressure HIL teststand

The commissioning phase tested the CAN-communication with the CMA valves, safety protocols, and the functionality of each component of the testbed. The system was also tested in all 4 quadrants of operations at low pressure (~50bar). A safety shutoff protocol was developed to shut down the system whenever unexpected conditions are encountered. Fig. 3.B10 shows a situation when a larger than expected pressure difference is observed across the pump, triggering input pressure to be relieved from the system.

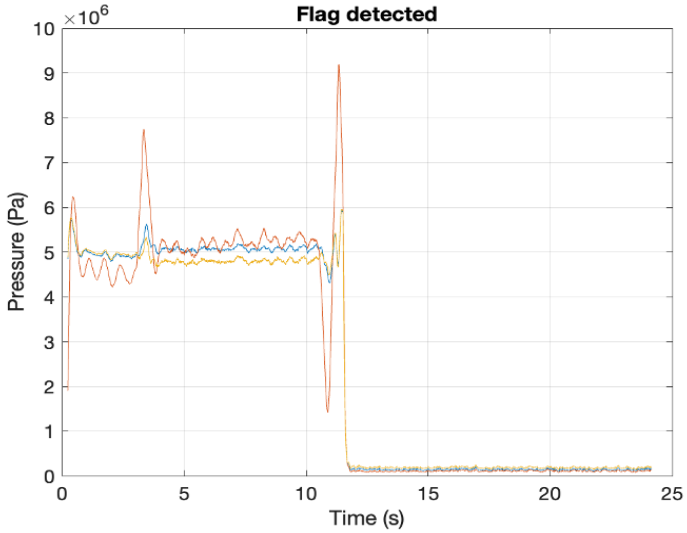

***Fig 3.B10**: Transition to a safe state after a flag (high pressure difference) is triggered*

Control testing

Successive versions of the controllers were implemented starting with the simple PID controller with no rail switches, to using the backstepping controller and the transition controller in the presence of varying load, rail switchings, and high pressure operation. A trapezoidal trajectory is used as it is common in motion planning.

The first tests were performed under a constant load of 4000N using the pressure rails set at 50 bar. The tests are to establish the performance of the baseline backstepping controllers. Sample results using a PID + feedforward controller and a backstepping controller are shown in Fig. 3.B11 where The PID controller exhibits position errors in the range of 5-10mm whereas the backstepping controller exhibits improved errors in the range of 5mm which is within the range of the sensor noise.

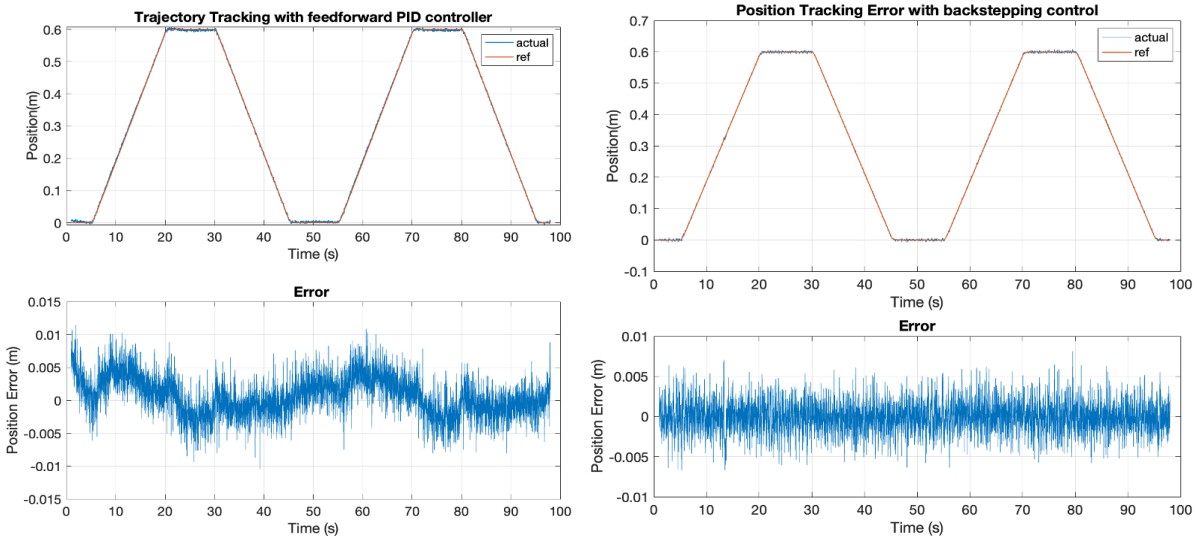

Fig 3.B11: Position tracking performance under constant load (4000N) and no rail switching (50bar) (Left): PID with feedforward controller, and (Right): Backstepping controller

The next tests involve load force variation, using the backstepping controller. Sample results are shown in FIg. 3.B12. Notice that the errors are not increased despite the load force variation.

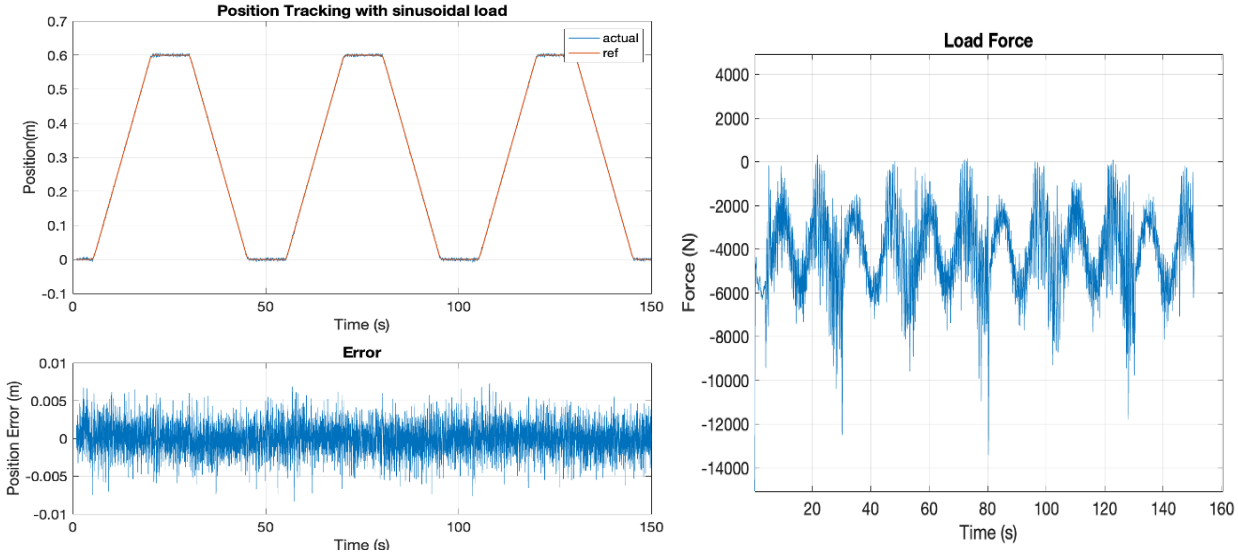

Fig 3.B12: Tracking performance under varying load force and no pressure rails switching (50bar).

Control performance with an intermediate pressure of 100 bar (the middle-pressure rail was selected on both sides of the actuator) and with a constant load of 10kN was tested next. Fig. 3.B13 shows again similar position tracking performance of 5mm.

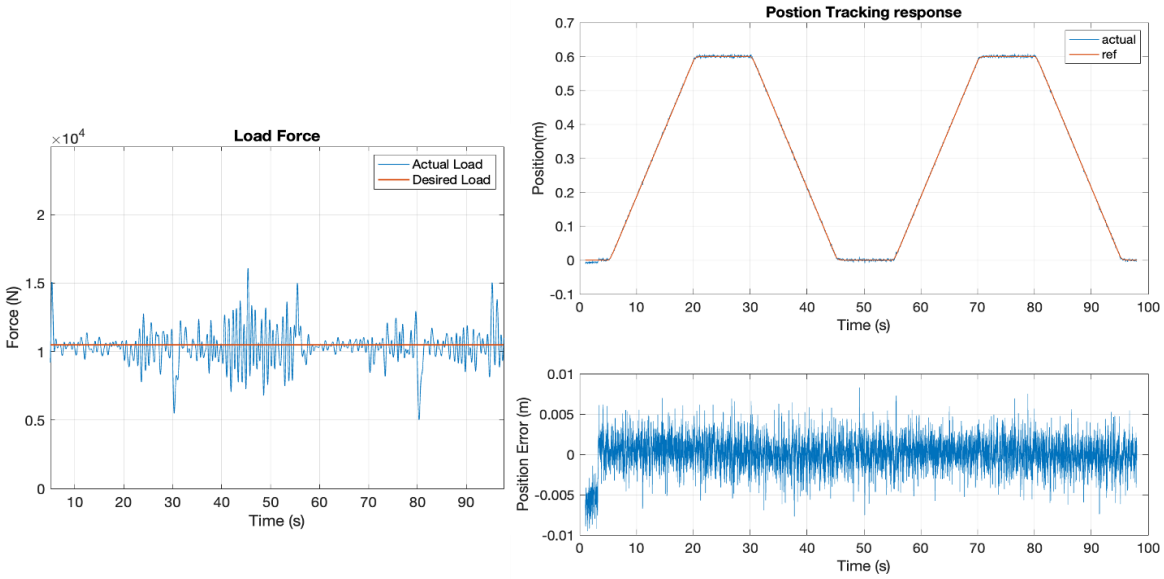

Fig 3.B13: Tracking performance with a higher constant load of 10kN and 50 bar pressures were selected on both sides of the actuator.

Having established that the backstepping controller works well when the pressure rails are not switched, the effect and mitigation of switching using the transition controller were tested next.

The first switching case is when switching on the rod side took place. To make it a more aggressive switch, the load force was kept constant.

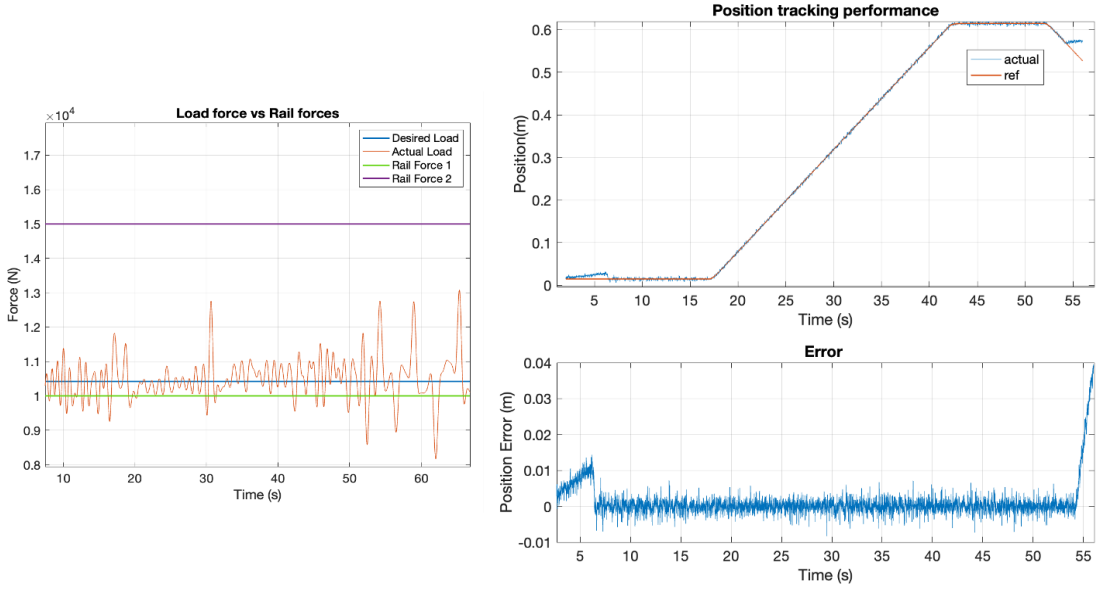

Fig 3.B14: Load force and position tracking performance for rod side switching case (electric motor was not engaged until 6 sec)

Sample results with only backstepping control and transition control are shown in Fig. 3.B14 where switching occurred at t=30 sec. After switching, a higher pressure difference across the HECM pump exists. The load is set in such a way that after pressure rail switching on the rod side, the electric motor was acting as a motor during the extension of the actuator, and was acting as a generator during retraction. with a pressure difference of 50 bar (Fig. 3.B15). As seen in Fig. 3.B14, despite the sudden pressure change, the tracking error is similar.

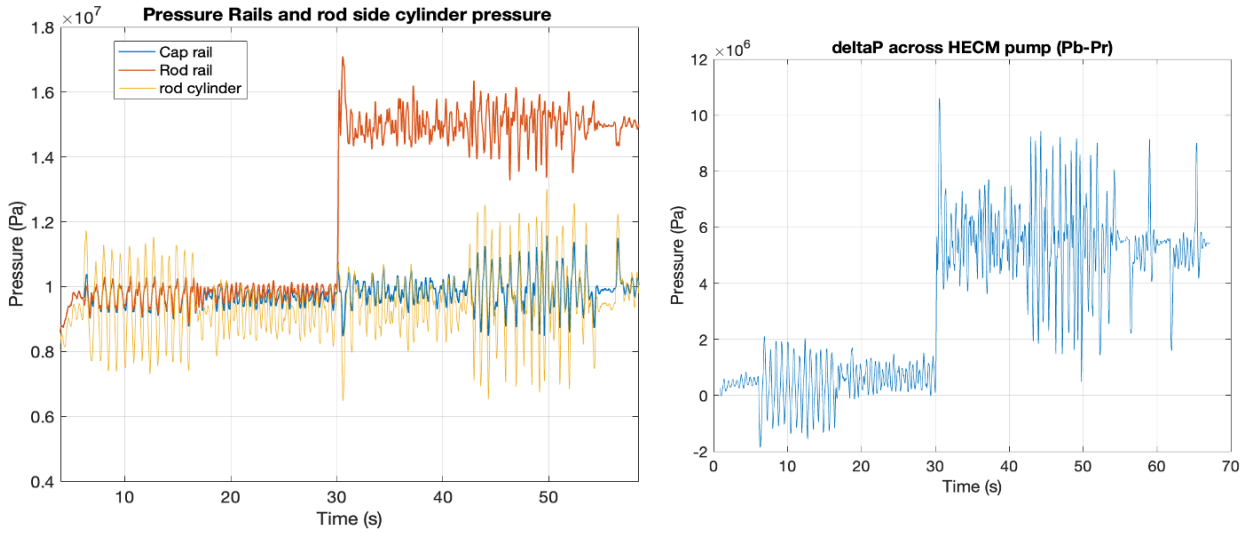

Fig. 3.B15*: Pressure rail switch on the rod side and pressure difference across HECM pump*

The next task is to demonstrate switching on both the cap and rod sides to 300 bar (highest pressure rail). Sample results are shown in Fig. 3.B16 where switching occurred at t=60sec. In this double switching case, the rail switch was designed in response to the varying load force to reduce the required electric motor torque. Between 45 to 50 seconds the load force dropped and the rod side pressure was increased to counter the drop in load. The desired trajectory in Fig 3.B17 has two parts, the first trapezoid showcases the switching at 60 seconds and the second trapezoid shows the entire duty cycle tracking with 300 bar (highest pressure rails) on both cap and rod sides. Again, tracking error is not increased noticeably despite rail switchings on both sides of the actuator to high pressure.

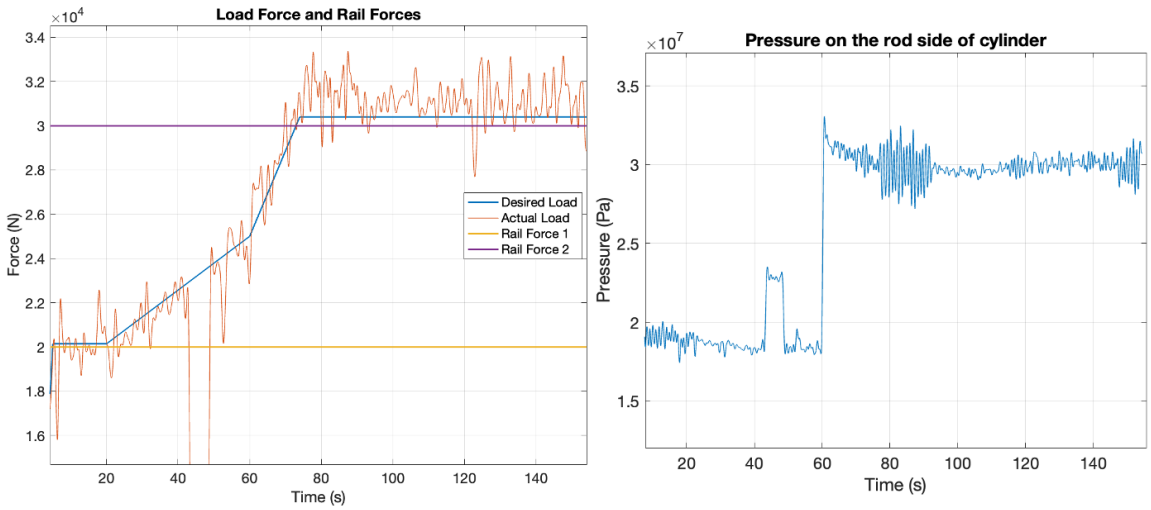

Fig 3.B16: Load force and rod side cylinder pressure for a double switching case

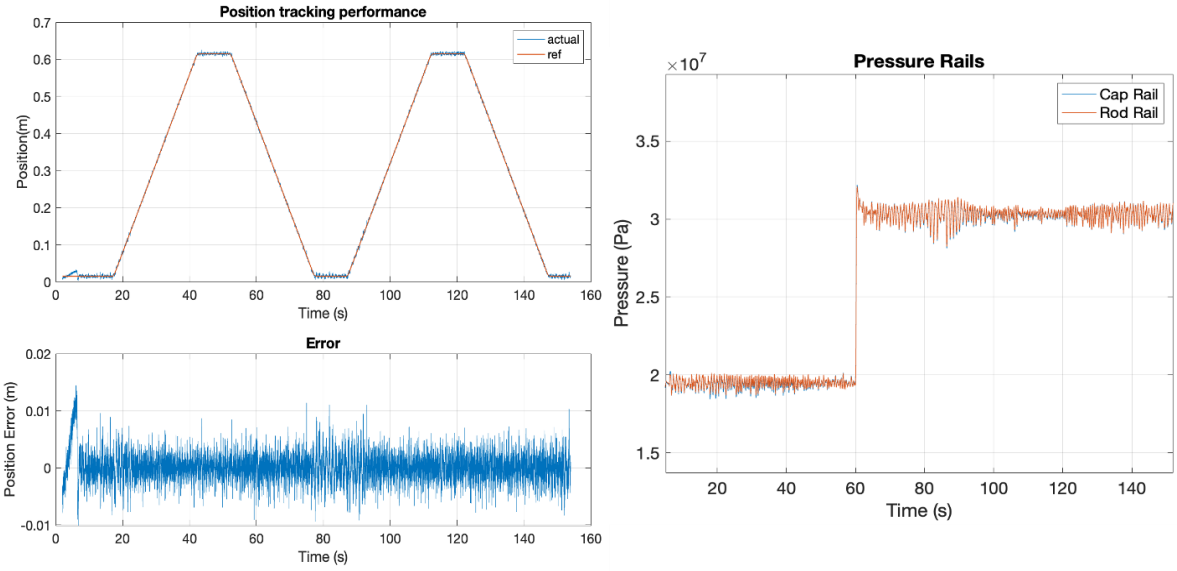

Fig 3.B17*:* Trajectory tracking performance and rail pressure for a double switching case

Finally, multiple double rail switches were tested during the retraction and extension phase of the duty cycle. In this test, rail switching from the high (300bar) to the mid-rail (200 bar) on the both cap and rod side was performed during the extension phase and rail switching from the mid to the high-rail was performed during the retraction phase. Sample results are shown in Fig. 3.B18 showing excellent tracking error and no noticeable increase in error magnitude due to the rail-switches.

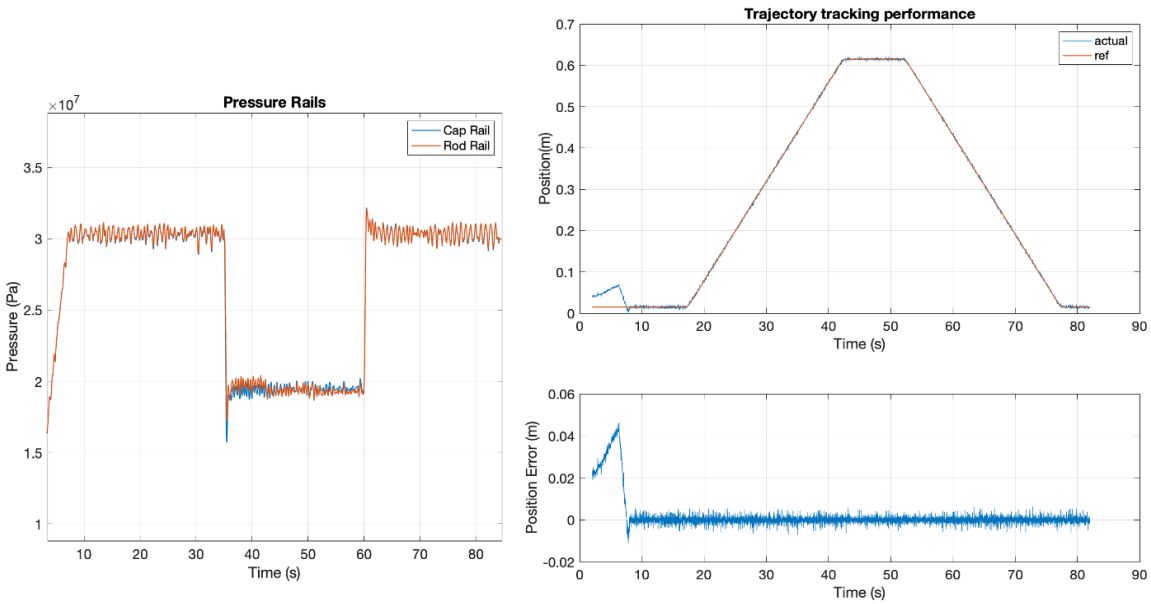

Fig 3.B18: Pressure rails and tracking performance for 2 different switches

These results have demonstrated that the backstepping and transition controllers are able to control actuator motion accurately despite load variation and rail-pressure switches, including operation at high-pressure of 300bar. Therefore, the "control at high-pressure (300bar)" milestone is satisfied.

3.3 Thrust C - Integration

In BP3, the main goal in Thrust C is to construct and characterize a prototype integrated electric-hydraulic machine. In BP2, the concept of an axial-flux electric machine integrated with a radial hydrostatic hydraulic pump/motor was determined, and a detailed design was completed. in BP3, this design is realized and tested. This work was executed under these tasks:

Task 3.C1 - Construct, test and analyze bench-top prototype integrated HECM

- Subtask 3.C1.1 Define experimentation and test-plan
- Subtask 3.C1.2 Fabricate hardware
- Subtask 3.C1.3 Experimentally characterize the prototype and analyze results

Task 3.C1 - Construct, test and analyze bench-top prototype integrated HECM

Subtask 3.C1.1 Define experimentation and test-plan

The plan is to test the prototype HECM in two phases

i) testing and characterization of the electric machine and the hydraulic pump

ii) testing and characterization of the integrated HECM.

Two separate test setups, one for the hydraulic pump and one for electric motor characterization as well as the integrated prototype will be developed. The detail plan of the test-plan is presented in Fig. 3.C1

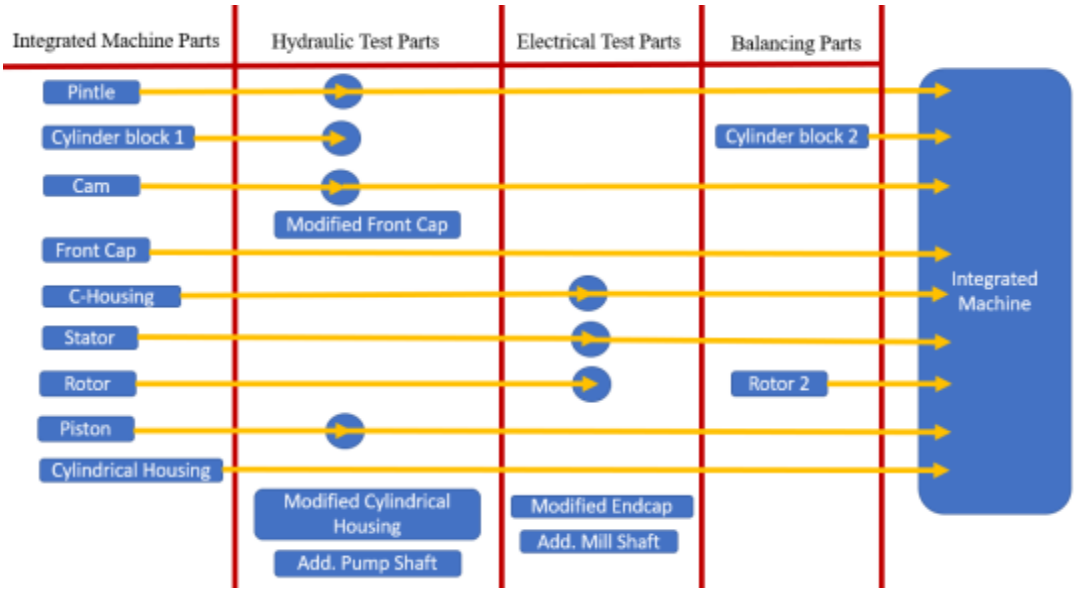

Fig. 3.C1: Test setup plan

The left most column in Fig. 3.C1 lists all the parts required for the integrated machine. Some parts of the integrated machine would be reused for the separate hydraulic and electrical test setups which are shown under the 'Hydraulic Test Parts' and 'Electrical Test Parts' column. Some additional parts would be required for these separate test setups. For instance, in the hydraulic test setup, a modified front cap, housing, and drive shaft would be required along with the other pieces shown in Fig. 3.C1.

Two cylinder-blocks and electric-rotors will be built which are shown in the 'Integrated Machine Parts' and 'Balancing Parts' columns respectively. One set of cylinder-block, and electric rotor will be sent out for balancing and another set will be used in hydraulic and electric setups. Fig. 3.C2-left shows the integrated machine that has been designed already and Fig. 3.C2-right shows the hydraulic machine setup.

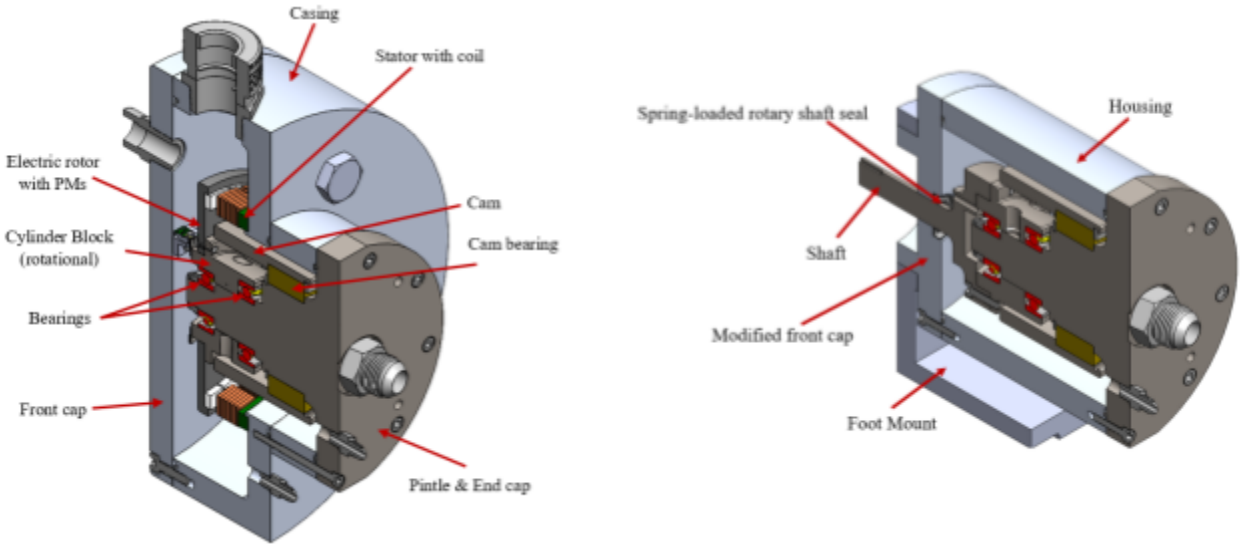

Figure 3.C2: Integrated machine (left) and Hydraulic Machine setup (right)

Testing plan for the electric machine is described next. Accurate measurement of the electric machine parameters such as the d-axis and q-axis inductances, stator resistance, back emf, torque constant etc is essential to implement effective closed loop control. These parameters, computed using finite element analysis, are listed in Table 3.C1.

Table 3.C1: Electric machine parameters from FEA

Parameter	**Value**
Stator resistance	15.3 mΩ
d-axis and q-axis inductances	52 µH
Back EMF (line-line)	150.16 $V_{(rms)}$
Torque constant	0.11 Nm / $A_{(pk)}$

Since the fabricated prototype may be different from those specified in Table 3.C1 due to non-ideal effects such as manufacturing tolerances, the characterization tests aim to experimentally measure and validate these parameters.

The following tests will be performed on the prototype. applicable standards [12]

1. Stator resistance measurement.
2. Axial force measurement.
3. Torque measurement at different stator currents and rotor angles.
4. d-axis and q-axis inductance measurement.
5. Back EMF measurement.

Test Setup: A CNC mill will be configured as a contact-free dynamometer for initial electric machine testing. A 3D rendering of the interface between the electric machine and the test fixtures is shown in Fig. C3. The stator will be mounted on a base plate attached to a load cell fixed to the bed of the mill to measure the reaction forces and torques on the stator. The rotor will be attached to the mill spindle using a custom built adapter plate. The CNC mill will be used to vary the air gap length and rotate the rotor.

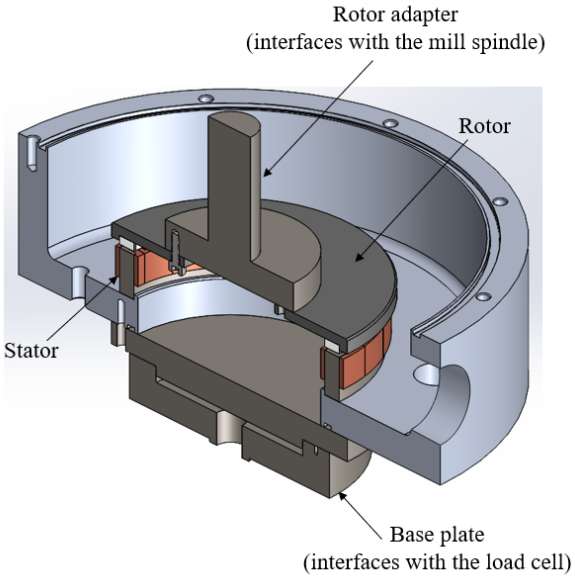

Fig.3.C3: Electric machine test fixtures

Subtask 3.C1.2 Fabricate hardware

The electric machine's rotor and the stator's manufacturing process is as follows:

1. **Rotor fabrication:** The rotor was manufactured by an outside machine shop. Since the machine is rated to operate at a high speed of 12,500 RPM, the fabricated rotor will be coupled with the hydraulic parts and balanced for a grade of 2.5G. Fig. 3.C4 shows the fabricated rotor.

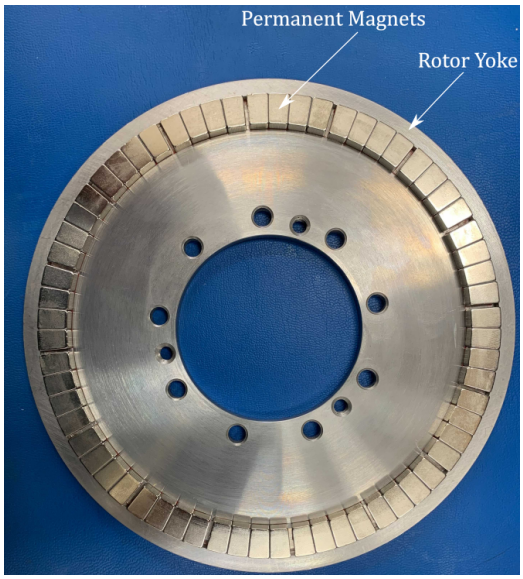

Fig. 3.C4: Fabricated rotor

2. **Stator fabrication:** The stator fabrication is divided into the following steps i) tape wound core manufacture, ii) slot machining, and stator winding. A fabricated bobbin (Fig. 3.C5) was used to wind the electric steel strip into a core. This core is bonded using an inorganic insulating adhesive 3M Scotchcast 9. The slots to accommodate the stator coils were cut into the tape wound core. This was

outsourced to an external manufacturer. Coils were wound using AWG 12 rectangular magnet wire. The complete stator with coils wound is shown in Fig. C4 (right). The stator was bonded using an inorganic insulating adhesive after winding the coils. A high potential (hi-pot) test was performed at 500V on the fabricated stator to verify the integrity of the windings. The results showed that there are no inter-phase winding short circuits or short circuits between phase windings and the stator core, indicating that the stator windings are electrically fit for experimentation. Fig. 3.C6 shows the stator core before and after winding.

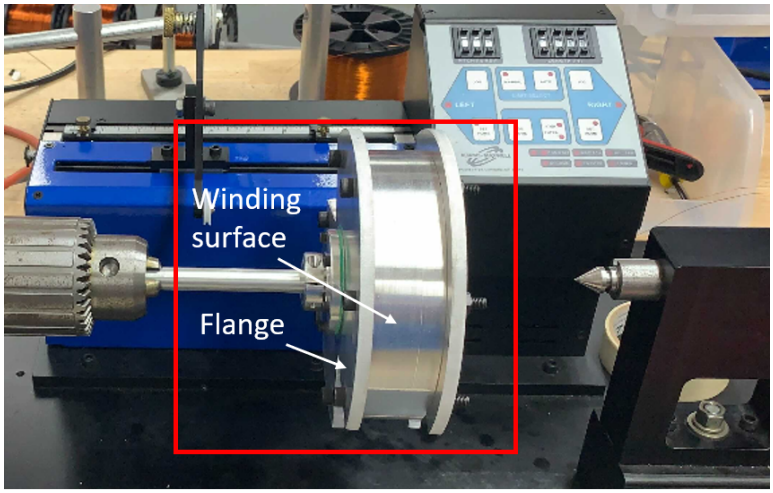

Fig. 3.C5: Bobbin for tape wound core manufacture. This bobbin is shown mounted in the chuck of a powered winding machine.

Fig. 3.C6: Electric machine stator: (left) before winding coils, (right) after winding coils.

Manufacturing of most of the components for the hydraulic machines was outsourced to a machine shop. Fig. 3.C7-3.C10 show some of the parts and the assembly process.

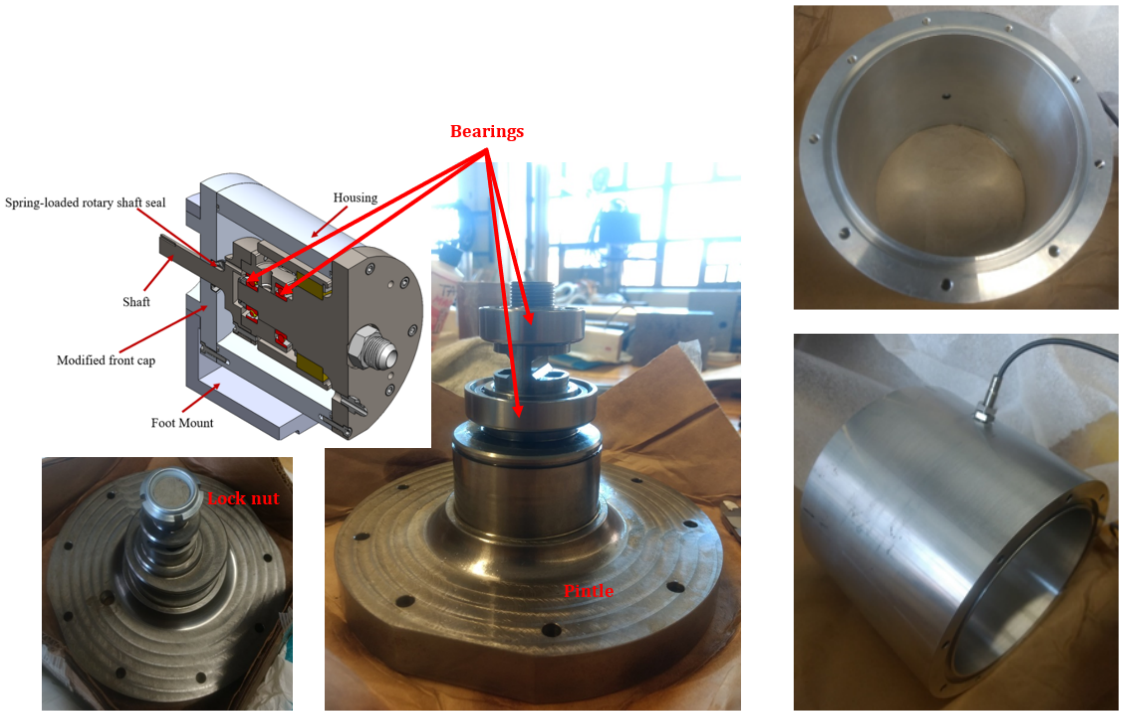

Fig.3.C7 (left): Pintle w/ bearing and locked nut; (right): Cylinder housing with proximity sensor

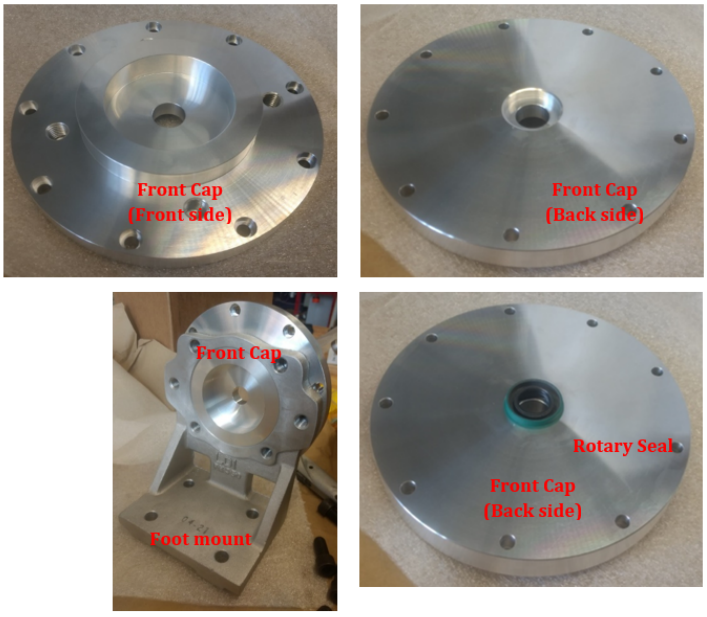

Fig. 3.C8: Front cap with foot mount and shaft seal

Fig. 3.C9: Piston and micro-orifice assembly

Fig. 3.C10: Hydraulic pump/motor assembly procedure

The assemblies shown in Fig. 3.C10 were without any pistons inside the pump. It is the case in order to characterize the unmodeled losses (primarily, churning losses) due to the moving elements inside the oil-filled casing. That experiment did not require any physical pumping; therefore, the pistons were not assembled.

Subtask 3.C1.3 – Experimentally characterize the prototype and analyze results

Electric machine side:

A CNC mill configured as a contact-free dynamometer will be used for the electric machine characterization. A 3D rendering of the interface between the electric machine and the test fixtures is shown in Fig. 3.C3. The stator is mounted on a base plate attached to a load cell fixed to the bed of the mill. This allows measuring the reaction forces and torques on the stator. The rotor will be attached to the mill spindle using a custom-built adapter plate.

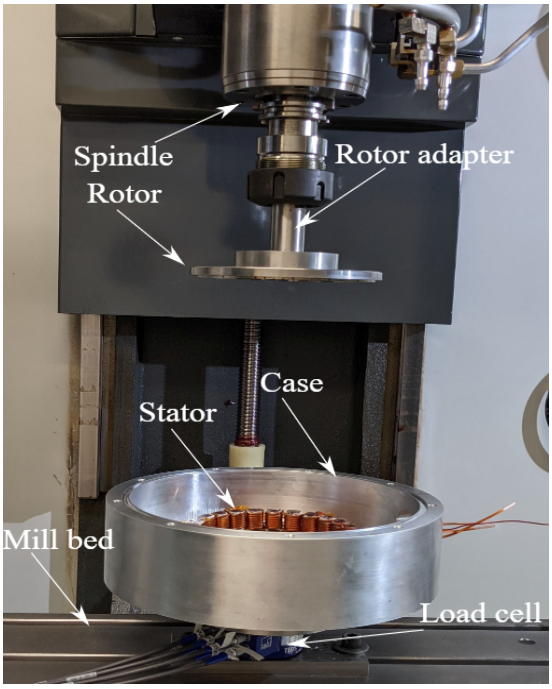

Fig. 3.C11: CNC mill configured as a contact-free dynamometer

Fig. 3.C11 shows the CNC mill configured as a contact-free dynamometer. This CNC mill was used to vary the air gap length and rotate the rotor. The stator case before and after mounting the stator is shown in Fig. C7. The stator is glued to the stator case using a chemical-resistant glue Araldite 2014.

Fig. 3.C12: (Left) Stator case; (Right) Stator fixed to the stator case

The rotor test fixture is shown in Fig. 3.C13 (left). The rotor attaches to this fixture as shown in Fig. 3.C13 (right). This fixture was mounted in the spindle of a CNC mill configured as a contact-free dynamometer.

(a) (b)

Fig. 3.C13: (a) Rotor test fixture; (b) Rotor attached to the test fixture.

Test results for cogging torque, axial forces, back EMF, and the static torque are now described (see [13]).

1. **Cogging torque and axial forces:** In the first set of tests, the cogging torque and axial forces between the stator and the rotor were experimentally measured using the contact-free dynamometer. The rotor position was varied in increments of 1 degree mechanical and the reaction torque and axial forces were measured using the load cell. These results are compared with 3D FEA calculations in Fig. 3.C14, where the average value of the experimentally measured axial force data is found to be 1.3% lower. This reduction is not considered to be significant and can be attributed to measurement uncertainty, effects of stator stacking, and deviation in the material properties from the datasheet parameters used for FEA analysis.

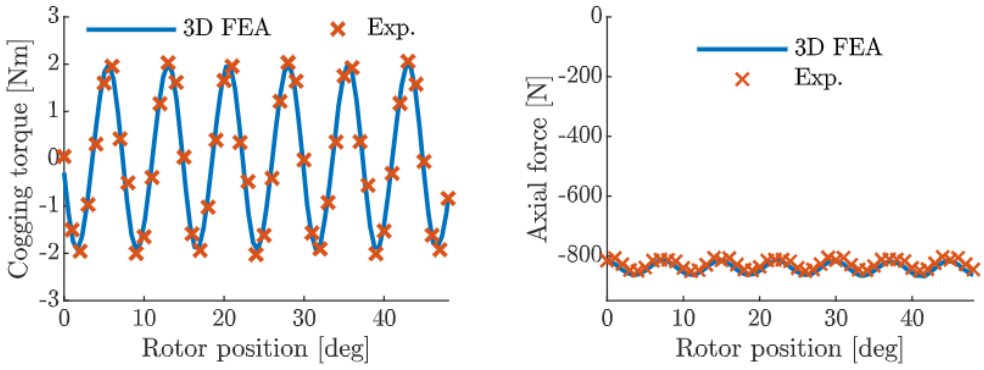

(a) (b)

Fig. 3.C14: Experimentally measured (a) Cogging torque; (b) Axial forces.

2. **Back EMF:** The back-EMF was measured by spinning the rotor using the mill spindle and measuring the voltage between the stator phase terminals and the neutral. The rotor was rotated up to 1,500 RPM, with the results shown in Fig. 3.C15a. The harmonic spectra of the experimentally measured back-EMF is compared against 3D FEA results in Fig. 3.C15b where the fundamental and harmonic amplitudes are found to have a difference of less than 1.5%.

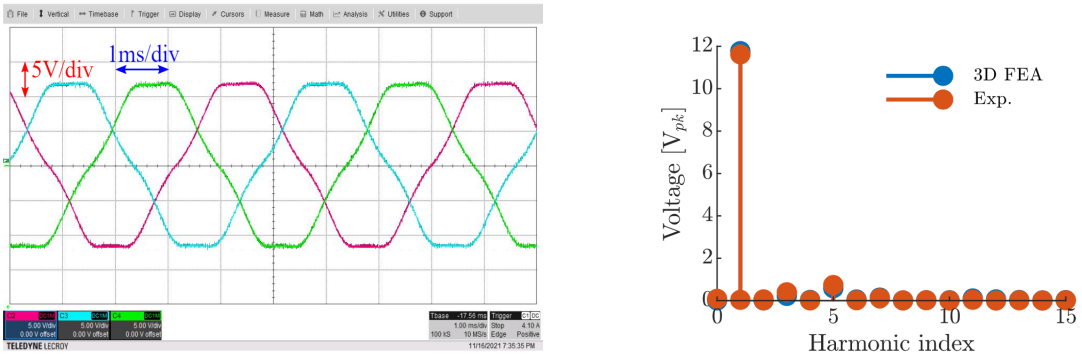

(a) (b)

Fig. 3.C15: Experimentally measured back EMF: (a) Oscilloscope waveform; (b) Harmonic spectrum at 1500 RPM.

3. **Static torque:** To experimentally determine the static torque at different rotor positions, a controlled DC supply was connected as shown in Fig. 3.C15a between phase B and phase C; phase A terminal was open circuited. The current I_{DC} was varied from 20 A to 140 A (rated peak current). At each current setting, the rotor position was varied over one electrical period and the reaction torque was measured at each rotor position. Since the machine is air-cooled for these tests, only the peak torque points were noted at current excitation of I_{DC} = 120 A and 140 A to keep the winding temperature within safe limits. The peak torque measured at the rated current I_{DC} = 140 A is 17.6 Nm resulting in a torque constant of K_t = 0.126 Nm/Apk. The experimental results are compared with 3D FEA results in Fig. 3.C15b and are seen to be in agreement, thereby validating the electromagnetic models used to analyze the AFPM.

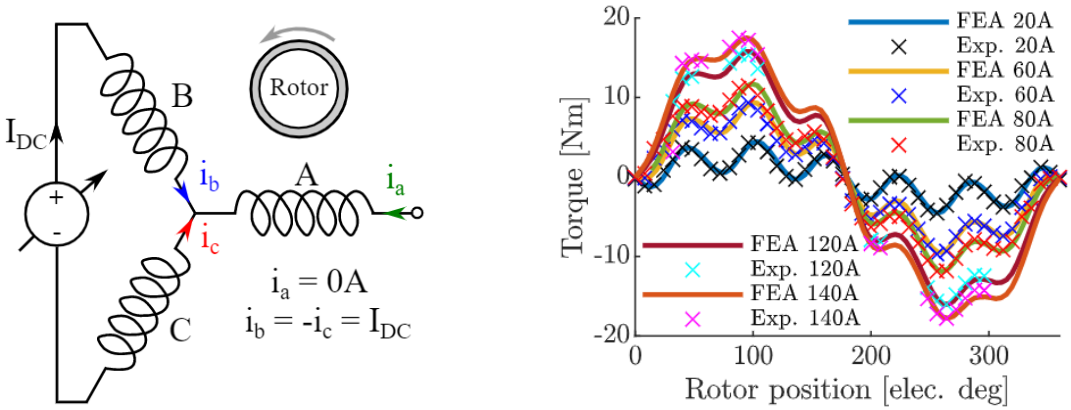

(a) (b)

Fig. 3.C15: (a) Circuit connection for static torque measurement; (b) Measured torque v/s rotor position at different current excitation.

The experimentally measured electric machine parameters are compared with analytical and FEA calculations in Table 3.C2. The measured parameters are seen to be in agreement with the calculated values, thereby validating the electromagnetic models used to analyze the electric machine.

Table 3.C2: Prototype electric machine parameters

Parameter	Calculated	Experimentally measured
Peak torque at rated current	17.53 Nm	17.60 Nm
Torque per ampere (K_t)	0.125 Nm/A_{pk}	0.126 Nm/A_{pk}
Inductance L_d, L_q	53.9 µH, 52.5 µH	65.58 µH, 61.69 µH
Stator phase resistance	21 m**Ω**	28 m**Ω**

To conduct dynamic characterization, similar to the static tests above, the CNC mill was configured as a contact-free dynamometer to characterize the electric machine with the stator mounted on a base plate attached to a load cell that is fixed to the bed of the mill. The electric machine's rotor was attached to a fixture and mounted in the CNC mill spindle which enables precise control of the air gap and rotor position and also allows rotating the rotor at different speeds. The electric machine stator was attached to a load cell mounted on the mill bed to measure the reaction forces and torques on the stator. Tests were performed to measure i) the stator iron losses, ii) the average torque, and iii) the viscous losses in the air gap.

1. **Torque and stator iron losses:** In the first set of tests, the average torque and iron losses were experimentally measured using the contact-free dynamometer. The schematic of the circuit connections is shown in Fig. 3.C16. The electric machine was run as a generator at speeds up to 5000 RPM (limited by the dynamometer and load ratings). The fabricated motor drive was used to control the q-axis current (and hence torque). The contact-free dynamometer was used to

control the motor speed, ω. The reaction torque T was measured using the load-cell, and the output electrical power P_e was measured using a power analyzer. The stator resistance R_s which was previously measured was used to compute the stator ohmic losses. Using the measured data, the stator iron losses were calculated as follows:

$$P_{Fe,s} = T\omega - P_e - 3I_{rms}^2 R_s$$

A polynomial was fit to express the iron-loss as a function of q-axis current I_Q [A] and speed ω [rad/s]. An amplitude invariant transformation was used to compute I_Q from 3-phase currents.

$$P_{Fe,s}(I_Q, \omega) = 13.75 - 0.2492 I_Q - 0.126\omega + 0.00179\omega I_Q + 4.03 \times 10^{-4}\omega^2$$

This polynomial is used to plot the iron loss as a function of current at different speeds and a function of speed at different q-axis currents in Fig. 3.C17a and 3.C17b respectively.

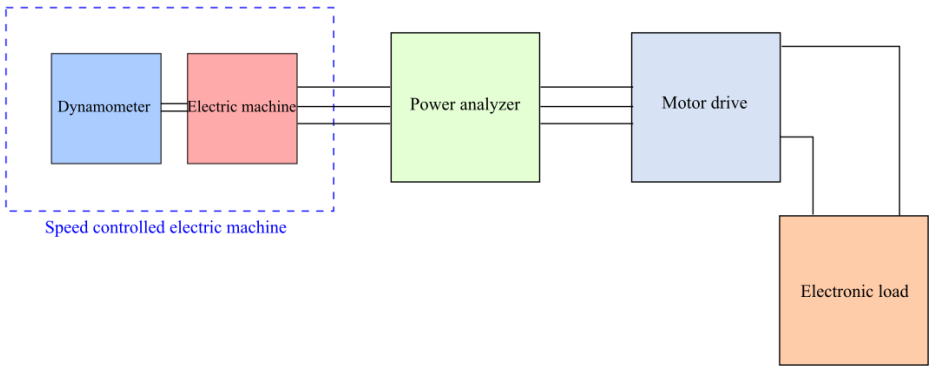

Fig. 3.C16: Schematic of the test setup to measure iron losses

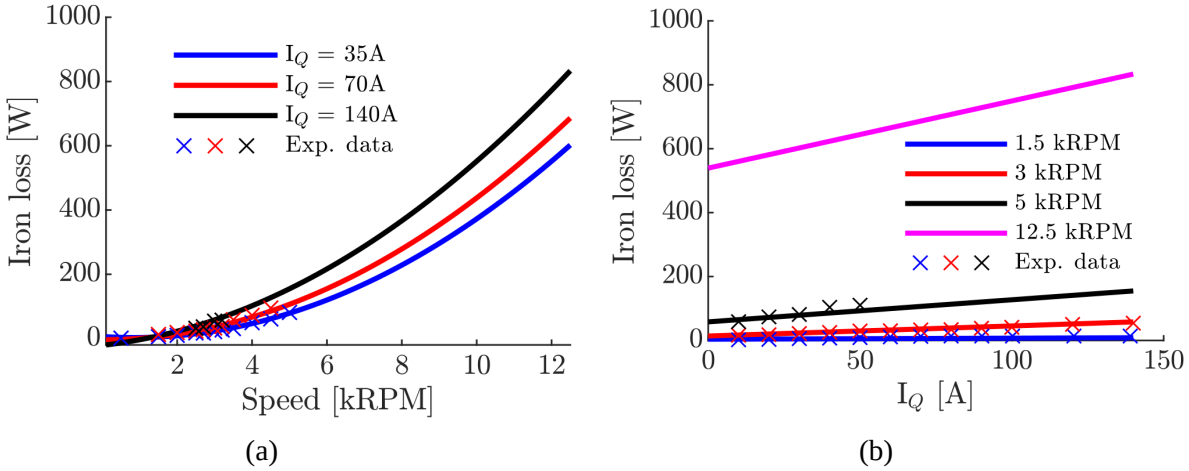

Fig. 3.C17: Iron losses as a function of: (a) speed and (b) q-axis current.

A plot of the measured iron loss versus speed is shown in Fig. 3.C18a, along with a curve fit for average iron losses. The losses estimated from FEA are also plotted in Fig. 3.C18a. It can be seen

that the fabricated machine is estimated to have higher iron losses than computed using FEA. This can be attributed to effects of manufacturing which impact the losses in the electric steel. The torque measured is plotted as a function of the q-axis current in Fig. 3.C18b. It can be seen that the measured torque is in good agreement with the FEA calculations.

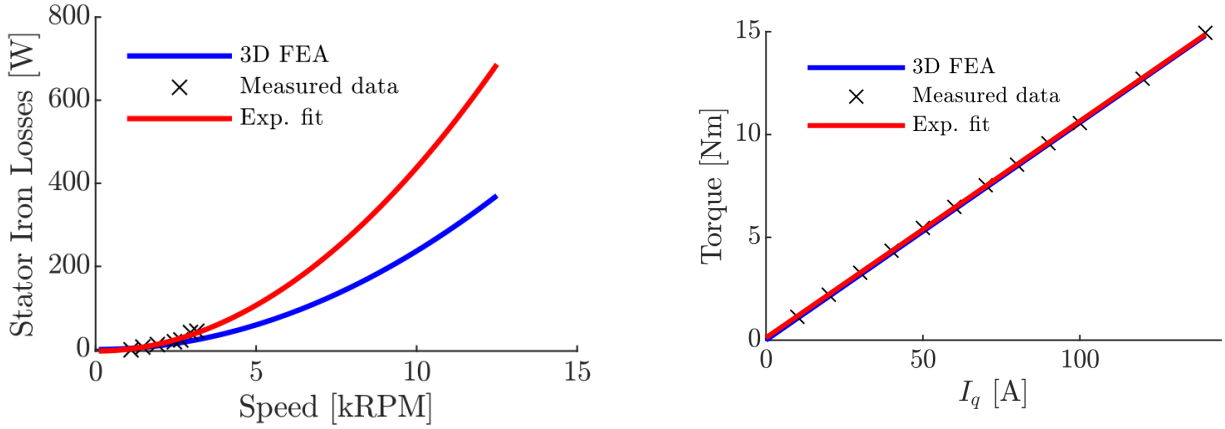

(a) (b)

Fig. 3.C18: 3D FEA v/s experimental results: (a) stator iron loss v/s speed for $I_Q = 140A$; (b) torque v/s q-axis current

An efficiency map computed over the entire operating range of the machine by curve fitting the experimentally measured iron loss and analytically computed copper loss data is shown in Fig. 3.C19. The machine promises an efficiency greater than 90% over a wide torque and speed range.

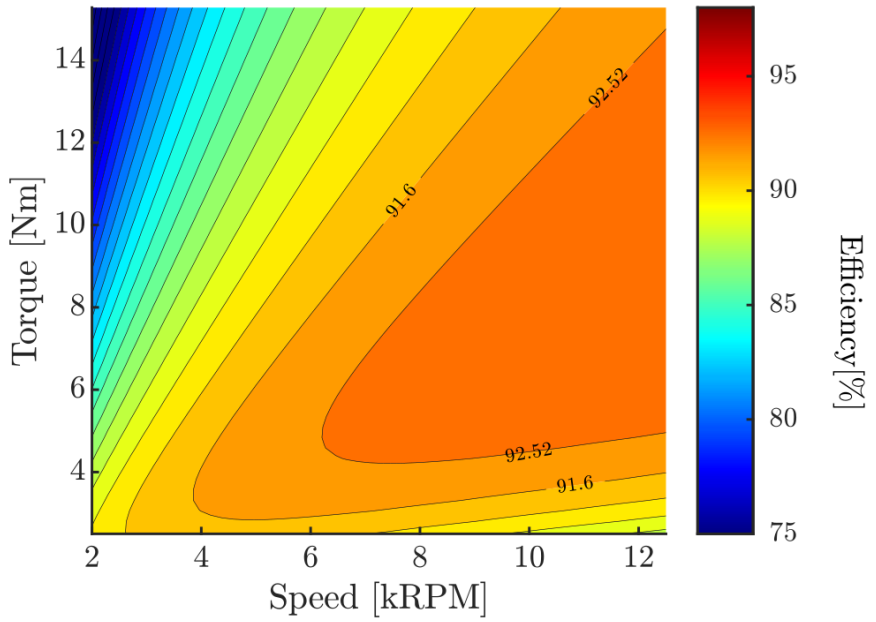

Fig. 3.C19: Efficiency map of the electric machine

2. **Air Gap viscous losses:** Hydraulic fluid in the electric machine air gap results in air gap viscous losses, which is a function of speed. The hydraulic pump is designed to use low-viscosity ISO 22 grade hydraulic fluid. However, since ISO grade 22 hydraulic fluid was unavailable at the time of

testing, automatic transmission fluid (approximately ISO grade 32) was used for the electric machine characterization. To experimentally measure these losses, the spindle of the test setup was allowed to spin freely and the electric machine was run in the motoring mode using the motor drive at speeds ranging from 100 RPM to 6000 RPM, first without oil in the case and next by filling the case with oil. Automatic transmission fluid (approximately ISO grade 32) was used since the hydraulic oil of ISO grade 22 was unavailable. The electric power input to the machine was measured at each speed for the tests with oil and without oil. The electric power input to the machine was measured at each speed for the tests with oil and without oil. The measured electric power input when the case was dry P_{dry} and when the case was filled with oil P_{oil} were used to compute the air gap viscous losses P_{visc} as follows:

$$P_{visc} = P_{oil} - P_{visc}$$

The following polynomial was fit using the measured data to express the viscous losses as a function of speed ω in units of rad/s.

$$P_{visc} = 0.00175\omega^2 + 0.2243\,\omega - 4.631$$

The experimentally measured viscous losses and curve fit to the experimental data are compared against the analytically estimated losses in Fig. 3.C20.

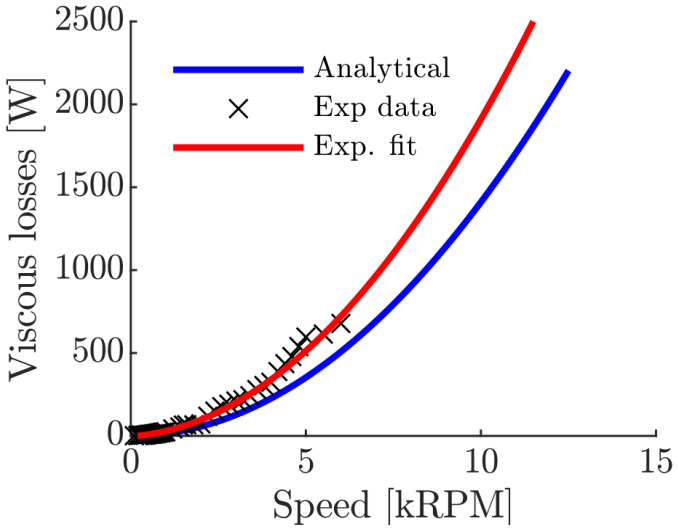

Fig. 3.C20: Viscous shearing losses in the electric machine.

Since the electric machine testing utilized automatic transmission fluid (ATF) of approximately ISO 32 grade, the viscous losses computed using the curve-fit to the measurement and plotted in Fig. C.3 needs to be corrected. As the viscous loss is directly proportional to the dynamic viscosity, the ratio of dynamic viscosities $(\mu_{iso\,22}/\mu_{ATF})$ is used as a correction factor to update the viscous losses. μ_{ATF} represents the ATF dynamic viscosity and $\mu_{iso\,22}$ represents the ISO 22 grade oil dynamic viscosity. At the temperature that the test was performed, 24^{o}C, $\mu_{ATF} = 0.051\ Ns/m^2$ per the ATF datasheet. The temperature of the ISO 22 oil in the hydraulic

test was approximately 30^0 C and at that temperature $\mu_{iso\ 22} = 0.026\ Ns/m^2$ per the oil datasheet. Using this data the curve-fit to the viscous losses can be updated as follows:

$$P_{visc-corr} = (0.00175\omega^2 + 0.2243\,\omega - 4.631) * (\mu_{iso\ 22}/\mu_{ATF})$$

With this corrected viscous shearing losses included, the electric machine efficiency map is plotted in Fig. 3.C.21. It can be seen from Fig. 3.C.21b that the experimentally measured peak efficiency of the electric machine is approximately 87.1%, which is lower than the maximum efficiency (90.7%) predicted using analytical and FEA models in Fig. 3.C.21a.

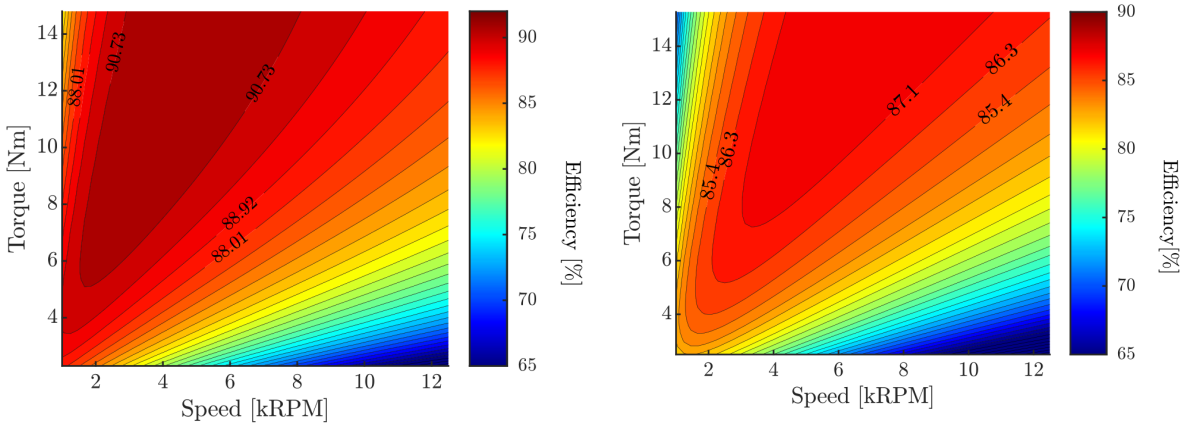

(a) (b)

Fig. 3.C.21: Efficiency map of the electric machine including air gap viscous losses: (a) analytically determined; (b) using experimental measurements.

It can also be seen from Figs. 3.C21a and 3.C22b that at the rated condition of 20 kW, 12,500 RPM, the experimentally derived efficiency map shows approximately a 2% drop in efficiency. This can be attributed to factors below:

1. The stator phase resistance in the prototype is 28 $m\Omega$ per phase while analytical models assumed a stator phase resistance of 20 $m\Omega$ per phase computed using the coil dimensions. The increase in stator resistance in the prototype is due to the end-winding length, non-ideal resistivity of the magnet wire, and the contact resistance at the end-winding connections, which cannot be analytically predicted. The 8 $m\Omega$ increase in resistance per phase, results in approximately 240 W of additional copper losses at the rated current of $100A_{rms}$ (approximately 1.2% drop in efficiency at rated power of 20kW).
2. It can be seen from Fig. C.1 that the measured iron losses are significantly higher compared to the iron loss computed using 3D FEA. This can be attributed to the change in material properties due to manufacturing induced stresses and manufacturing tolerances.
3. It can be seen from Fig. 3.C21 that the experimentally measured viscous shearing losses in the air gap are higher than the analytical prediction. The analytical prediction assumes idealized geometry shapes and flow patterns to estimate the viscous losses in the air gap. Using higher fidelity models (such as CFD) can potentially improve the accuracy of the analytical viscous loss estimates.

3. **Drive cycle tracking:** This test is used to evaluate the motor's ability to perform dynamic control tasks. In the HECM application, the integrated electric-hydraulic machine must buck or boost the pressure from the selected pressure rail to the desired pressure for the drive cycle. As far as the electric motor is concerned, this is equivalent to controlling the electric motor torque. In this test, The drive cycle for the integrated electric-hydraulic machine, based on OEM provide drive cycle and the optimal rail-selection algorithm was provided by Thrust-A in terms of pressure differentials Δp and flow rates Q (Fig. 3.C21).

   The drive cycle tracking capability of the electric machine was experimentally validated using the contact-free dynamometer setup. To characterize the electric machine within the capability of the test equipment, the drive-cycle data was processed as follows:

   1. Since the contact-free dynamometer does not allow loading of the electric machine when run as a motor, the electric machine was configured as a generator per the schematic.
   2. The electric machine torque command T was computed by normalizing the pressure differential data as $T = \frac{abs(\Delta p)}{max(\Delta p)} T_{max}$ where, $T_{max} = 14.8\,Nm$ is the rated torque of the electric machine.
   3. Since the test setup does not allow varying the torque and speed simultaneously, the dynamometer was set to a constant rotational speed. Torque commands computed in step 2 were applied to the electric machine. These commands and the electric machine response were logged.

   The command torque and the electric machine response are plotted in Fig. 3.C22. It can be seen from these plots that the machine can satisfactorily track the torque commands.

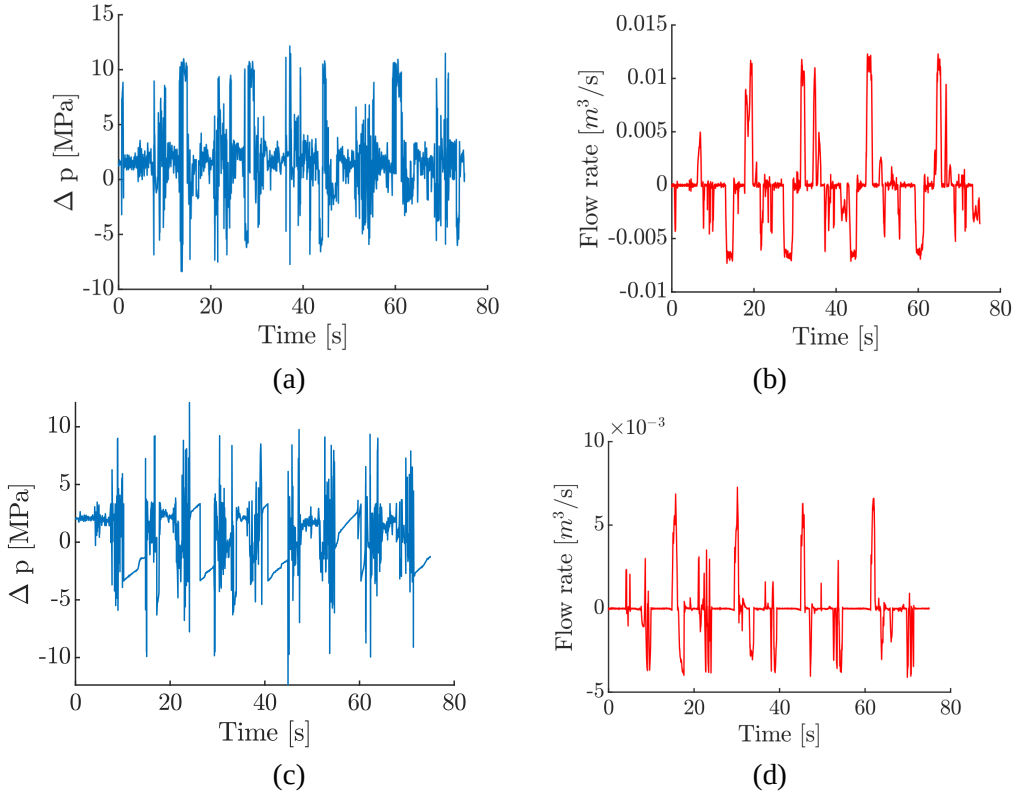

Fig. 3.C21: Drive cycle data: (a) drive cycle 1 pressure differential; (b) drive cycle 1 flow rate; (c) drive cycle 2 pressure differential; (d) drive cycle 2 flow rate.

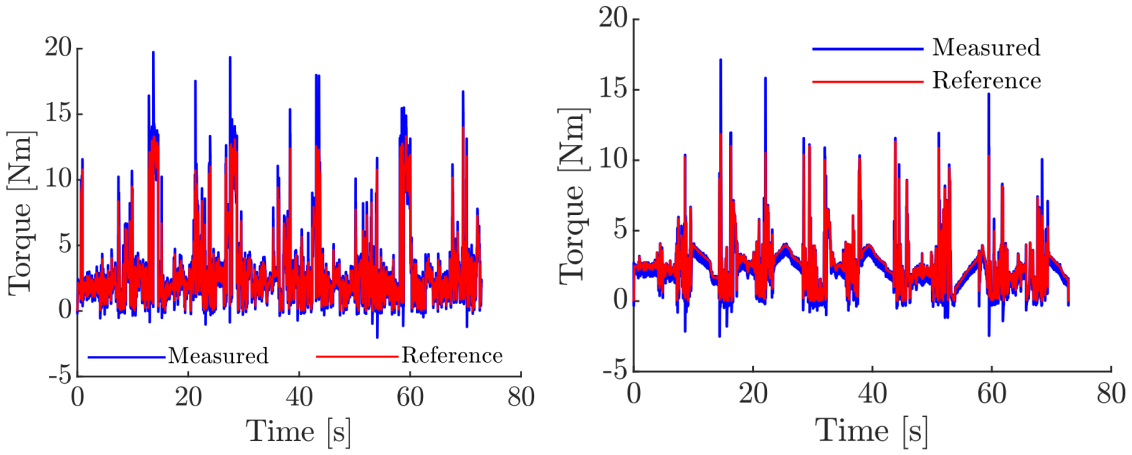

Fig. 3.C22: Drive cycle tracking performance: (a) Drive cycle 1; (b) Drive cycle 2.

Hydraulic machine side: To experimentally characterize the prototype, two experimental test setups were prepared.

a) *Hydrostatic radial piston pump test setup:* An experiment setup was built at the UMN facilities to test the high-speed pump as an isolated device. Figure 3.C12 shows the hydraulic circuit prepared for this radial piston pump characterization. A hydraulic power unit (HPU) is used to run a Rexroth bent-axis motor (A6VM 28 EP1/ 63W-VAB010A[1]) that is mechanically coupled with the hydrostatic piston pump shaft. This is a bidirectional hydraulic motor and its displacement is controlled by a proportional solenoid valve. A torque transducer (Futek Torque Sensor – model TRS605 50 Nm with rotary encoder) will be used between this pump shaft and the hydraulic motor shaft to estimate the torque and speed delivered to the pump respectively. Additionally, a charge pump will be used to provide 2MPa pressure at the low-pressure port (B port). A needle valve in the circuit (in parallel with the pressure relief valve) will be used as a pump load. Two pressure transducers will measure the inlet and outlet pressures and two flow meters will measure the discharge flow and leakage flow via the case drain. A temperature probe at the pump's outlet will measure the casing oil temperature to estimate the oil viscosity. The cam inside the pump will freely rotate; to estimate the cam speed a magnetic proximity sensor will be mounted on the casing with a ring magnet mounted on the cam.

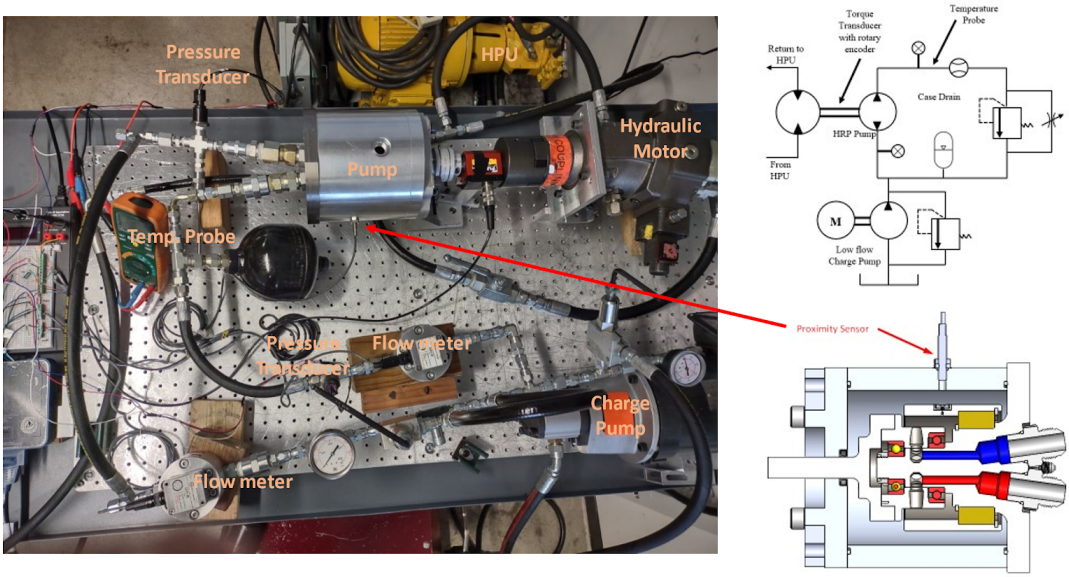

Fig. 3.C23: Hydrostatic Radial Piston Pump Test Setup**.**

Before running this full phase experiment, two separate experiments (with/without oil-filled casing) were run to find a relation between the churning losses and rotational speed of the pump. At a speed of 1750 rpm, the torque losses were only 0.5 Nm which demonstrated very low bearing friction, drive shaft friction losses, and churning losses. In the full phase experiment, the pump operated very quietly, generating smooth flow. However, the leakage was found to be higher than what was expected from the model. The reason behind that was the tolerance between the manufactured pintle and cylinder block (35 micrometer) was almost double what was in the model (18.5 micrometer). However, this leakage could be isolated, therefore, still, the pump performance can be demonstrated.

While testing the radial hydrostatic piston pump, several incidents have occurred which have necessitated redesigning and remanufacturing the pump piston. The accidents occurred when the charge pump was randomly shut down leading to insufficient pressure to keep the piston on the cam, causing the pistons to collide with the cylinder. Fig. 3.C24 shows one of the bent pistons.

Fig. 3.C24: Collisions between piston and cylinder, and damages on the piston/slipper

A redesigned new piston shown in Fig. 3.C25 has been designed and remanufactured with these improvements: i) The thickness of the piston has been increased; ii) The joint between the slipper and piston is ensured by a partial press fit and threaded joint. M3X0.5 vented button head screw has been used in this regard. It was designed carefully with an additional washer so that the button head does not touch the cam. The pistons were originally made of Aluminum and the slippers were made of bronze. To increase the strength and robustness of the pistons, the materials for the pistons and slippers were changed from aluminum and bronze to 4340 Steel and 4140 Steel respectively. However, these steel pistons and slippers increased the total mass of the pistons which would generate higher centrifugal loads compared to the original design. The mathematical model shows that beyond an operating speed of 9000 rpm with a high-pressure differential ~ 7 MPa the slipper would touch the pad which would increase the frictional losses. The single-phase TEFC electric motor (that failed during the experiment) was replaced by a 3 phase ODP type electric motor. A high flow (0.37 in^3/rev) gear pump was also purchased to work as a charge pump.

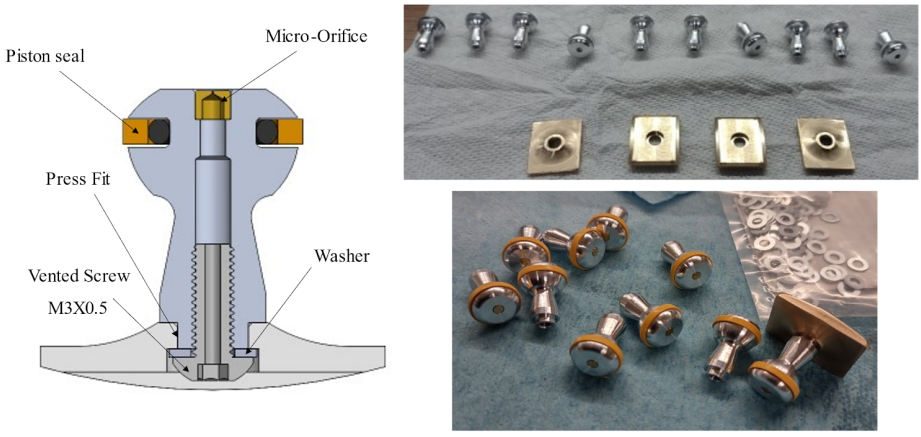

Figure 3.C25: New pistons and slippers

A. **Rotary shaft seal loss, bearing loss, pintle-cylinder block gap loss and churning losses**: To characterize the rotary shaft seal loss, bearing loss, pintle-cylinder block gap loss, and churning losses, the pump was installed without any piston in it and then the casing was filled with hydraulic ISO 22 grade oil. The pump was run at different speeds and all these losses were captured as torque loss using a torque transducer installed between the source (hydraulic motor) and the pump. Figure 3.C26 shows the torque (rotary shaft seal loss, bearing loss, pintle-cylinder block gap loss, and churning losses) at different speeds. All these losses are proportional to the speed, therefore, the losses are increasing with speed as expected.

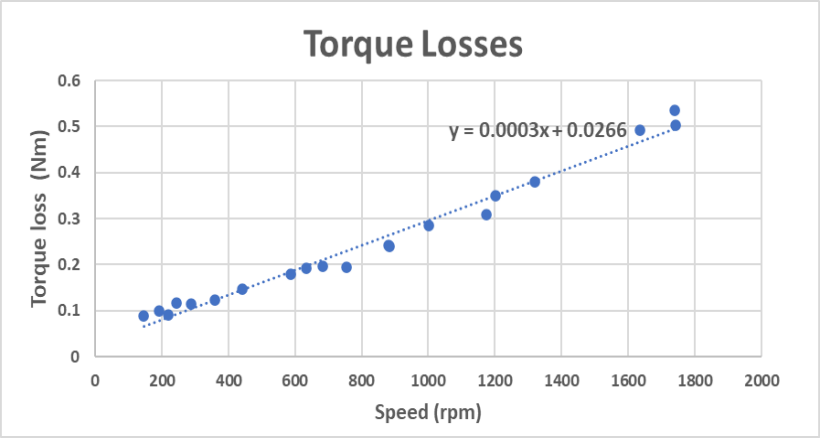

Fig. 3.C26: Rotary shaft seal loss, bearing loss, pintle-cylinder block gap loss and churning losses of the pump at different operating conditions.

B. **Pump volumetric losses**:

The prototype radial hydrostatic piston pump successfully ran under different operating conditions up to a peak speed reached is 2723 rpm and a pressure differential of 1.5 MPa. The peak speed is imposed by the teststand's flow limits. High speed (~12500 rpm) testing and high pressure differential (~7MPa) will be tested for the integrated electric motor and pump. However, testing the pump in these limited speed and pressure conditions at the UMN facilities is still beneficial. The mechanical and volumetric losses found in the limited speeds and pressure differentials can be extrapolated to any higher speeds and pressure differentials.

Two flow meters were connected at the inlet and outlet of the pump to collect flow data under different operating conditions. The volumetric losses were calculated from the experiment and then the fit equations are used to calculate the volumetric loss at different operating conditions:

$$Vol.\ loss\ (in\ GPM)\ =\ 0.1817\ +\ 1.878e\ -\ 7\,\Delta P\ +\ 0.0005512\,\omega$$

In this equation the P is measured in Pa and measured in rpm. The experimental data was collected in gpm (small scale). Finally, the volumetric efficiency map is generated using the following equation and the map is shown in Fig 3.C27,

$$Vol.\ efficiency\ =\ (\omega D/60\ *\ 1585.3\ -\ Vol.\ loss)/(\omega D/60\ *\ 1585.3\ )\ *\ 100$$

In this equation, D represents the volumetric displacement in m^3/rev.

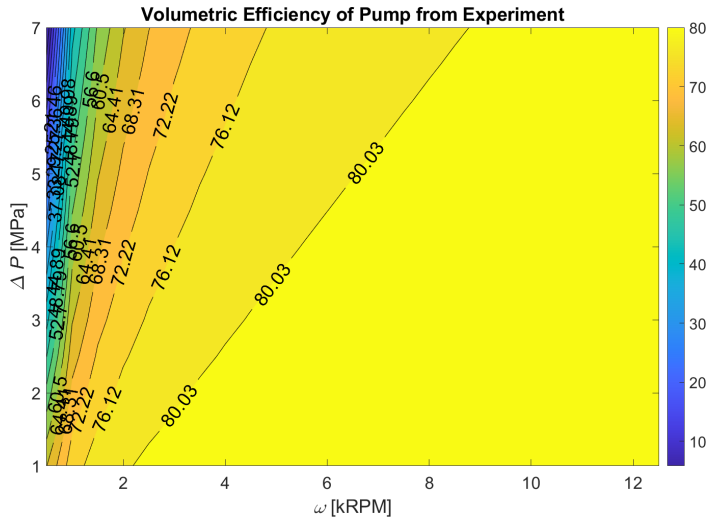

Fig. 3.C27: Experimental volumetric efficiency map of the radial hydrostatic piston pump.

Fig. 3.C27 shows the peak volumetric efficiency is approximately 80% for the pump, whereas from the mathematical model the peak volumetric efficiency was estimated to exceed 90%. There are several reasons behind that. First, the manufacturing tolerance between the pintle and cylinder block was 35.5µm, higher than the requested specification (27 µm), and second, during the piston failing events it created multiple scratches on the pintle outer surface (Fig. 3.C28) and cylinder block inner surface. These scratches were removed by polishing using grinding stones and emery paper which reduced the effective outer diameter of the pintle and the inner diameter of the cylinder block. All these in turn increased the gap between the pintle and cylinder block and hence, the leakage. From the mathematical model, the pintle-rotor interface leakage can be calculated as [14] :

$$Q_{pintle-case} = \frac{h_{pinte}^3}{6\mu} \frac{P(\theta) - P_{case}}{\delta_p} r_{pinte}\theta$$

where, h_{pintle} is the gap between the rotor (cylinder block) and the pintle. Due to the cubic power, increase in this gap increases the leakage drastically. For instance, at 1045 rpm speed and 1.63 MPa pressure differential, for a 27 µm gap, the leakage from the mathematical model was 0.16 gpm. However, for the 35.5µm gap measured in the prototype, the model anticipates a leakage of 0.34 gpm. The experimental leakage from the pump prototype at this particular operating condition was found to be 0.84 gpm due to further reduction of pintle outer diameter and cylinder block inner diameter which were required to remove the scratches from the pintle and cylinder block surfaces.

As the leakage is pressure dependent, therefore, at high pressure the leakage increases significantly which decreases the volumetric efficiency at high-pressure conditions.

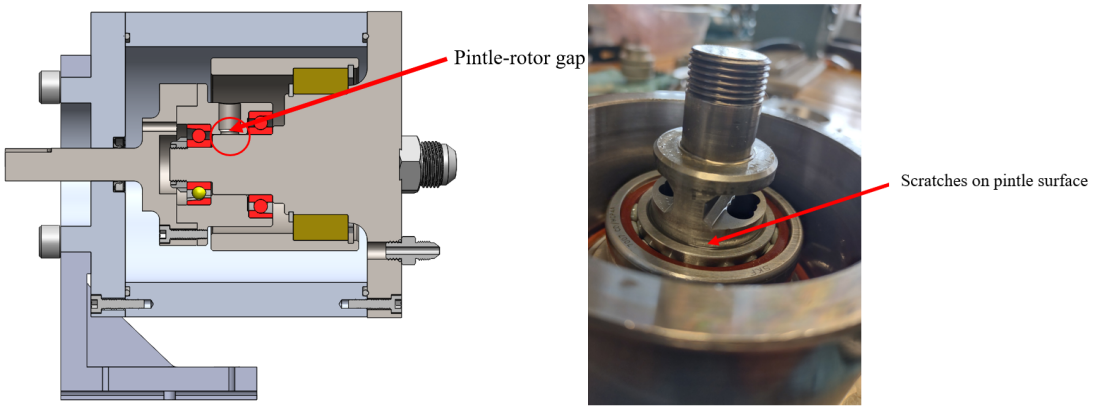

Fig. 3.C28: (a) Gap between the pintle and rotor (b) Scratches on the pintle surface.

C. Pump mechanical losses: Mechanical losses in the pump include the following components: rotary shaft seal loss, piston seal loss, slipper pad losses, pintle-cylinder block gap losses, churning losses, and throttling losses. A torque transducer was used to calculate the input torque and the mechanical losses are calculated using the following equation at different operating conditions:

$$Mechanical\ loss\ =\ Input\ torque\ -\ \Delta PD/2/\pi$$

The following fit equation is used to calculate the volumetric loss at different operating conditions.

$$Mechanical\ loss\ (in\ Nm)\ =\ 2.452\ +\ 1.968e\ -\ 7\ \Delta P\ +\ 0.0004779\ \omega$$

Fig. 3.C.29 shows the mechanical efficiency map of the pump using the following equation:

$$Mechanical\ efficiency\ =\ (\Delta PD/2/\pi)/(\Delta PD/2/\pi\ +\ Mechanical\ loss)\ *\ 100$$

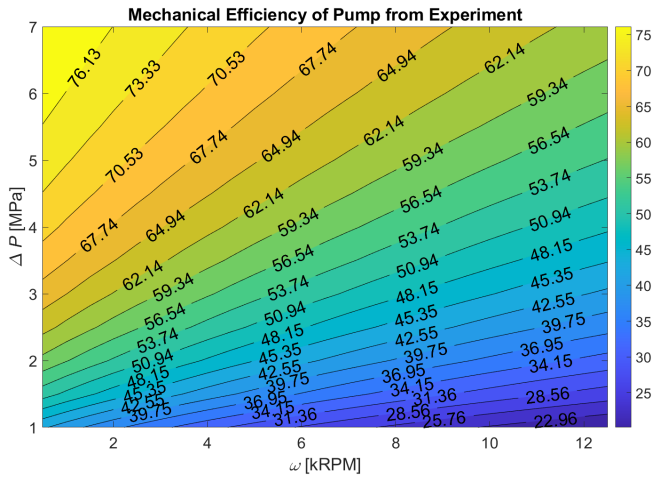

Fig. 3.C29: Pump mechanical efficiency map generated from the experiment.

Combining the mechanical and volumetric efficiencies of the pump generated from the experiment Fig. 3.C30 shows the overall efficiency of the pump.

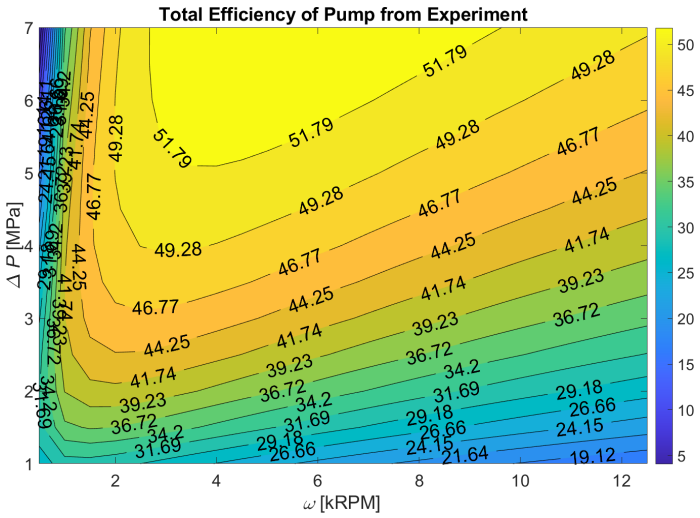

Fig. 3.C30: Pump overall efficiency map

It was found in experiments that the drive shaft touched the casing (Fig. 3.C31) overcoming the seal in between and generating higher frictional losses in all the tested operating conditions. This decreased the mechanical efficiency by around 10%. The pump efficiency with this problem does not reflect the true pump efficiency. This problem can be solved by careful assembly of the drive shaft and casing, keeping a proper seal in between. On the other hand, the integrated machine does not require any drive shaft, therefore, these losses would not occur there, which is an additional benefit of the integrated machine.

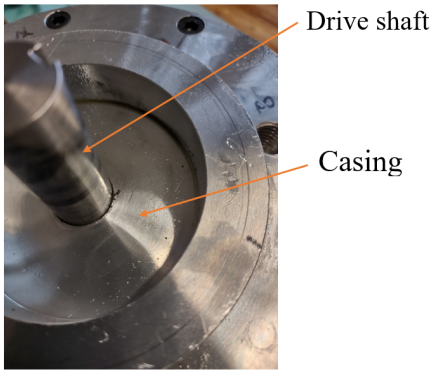

Fig. 3.C31: The drive shaft touched the casing in the seal land

To resolve this issue, the experimentally calculated rotary shaft seal losses, churning losses, pintle cylinder block gap losses, bearing losses and piston seals losses are added with the analytically determined throttling and slipper-pad frictional losses to determine the total mechanical losses. With that, the ideal pump efficiency is shown in Fig. 3.C32.

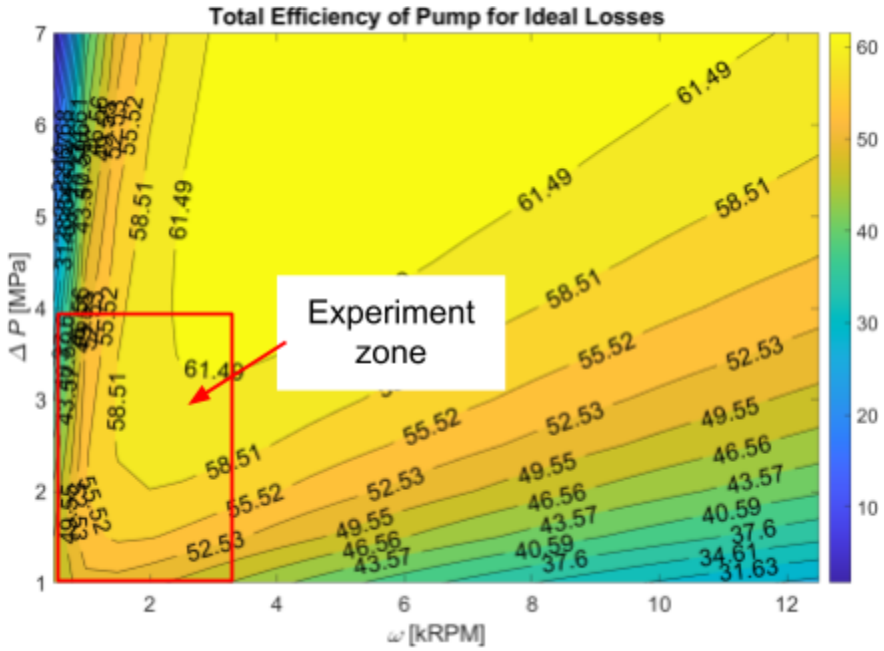

Fig. 3.C32: Pump overall efficiency map considering the ideal losses

Note that for the radial hydrostatic piston pump/motor, the volumetric and mechanical efficiency measurements were taken at a relatively small range of speeds and pressure differences as shown in Fig. 3.C33. Nevertheless, the losses and hence, efficiencies, can be extrapolated to other speeds and pressure differences with proper curve-fitting functions.

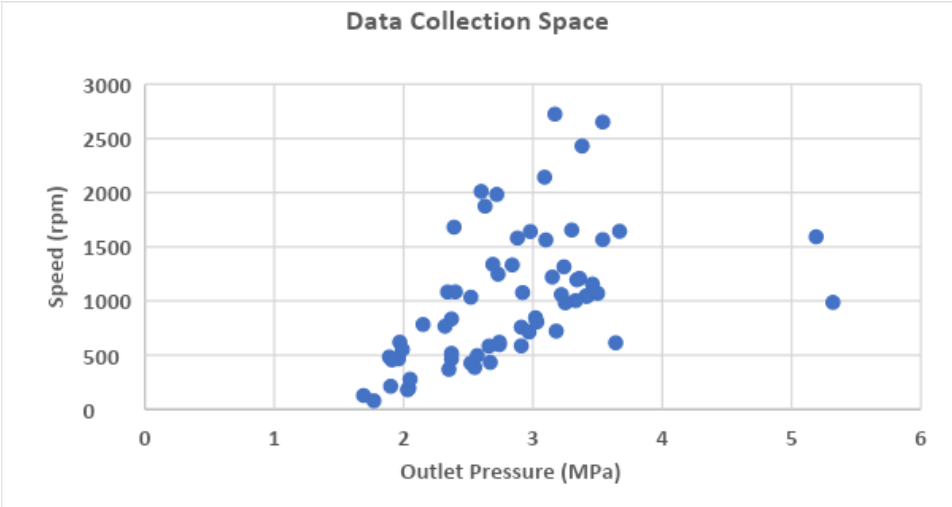

Figure 3.C33: Data collection space

b) *Integrated machine test setup:* The integrated machine was assembled and tested at the UW-Madison facility for validation of the integrated machine model and thermal model. In the integrated machine test setup, an inductive encoder will sense the position of the electric rotor-cylinder block assembly, which will signal the controller (inverter) switching. Fig. 3.C13 shows

the integrated machine test setup. In this test set up instead of measuring the torque and speed, the applied voltage and current will be measured directly to determine the power input. The pressure differential across the pump and flow rate will be measured in a similar manner to the hydraulic test setup.

In addition to flow and pressure sensors, thermocouples are also connected to stator tooth, yoke, and three locations in the slot windings and transmitted via a passthrough, allowing component temperatures to be determined at different operating conditions.

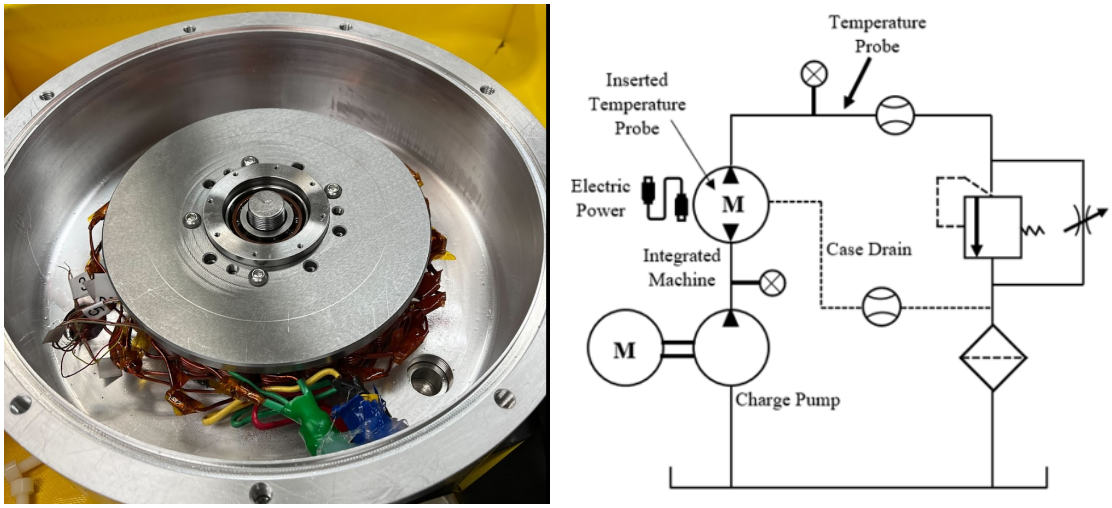

Fig. 3.C34: Integrated electric-hydraulic machine and schematic of the test circuit.

Some pictures of the test setup are shown in Fig. 3.C35-3.C36.

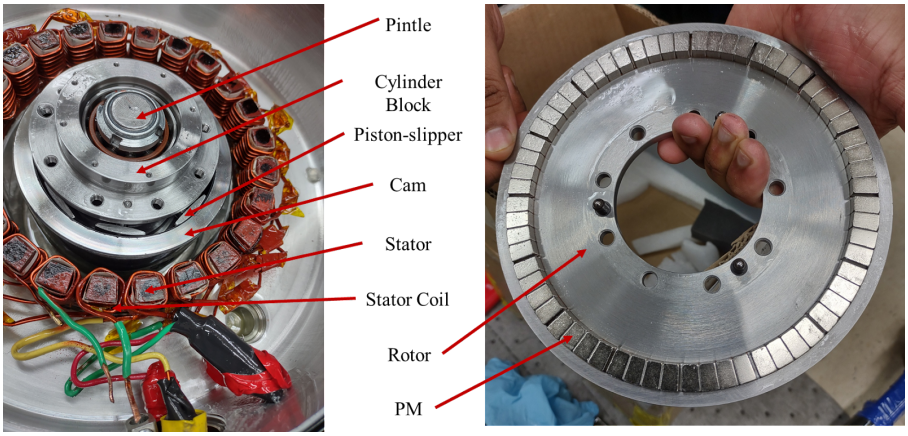

Fig. 3.C35: Integrated electric-hydraulic machine with an axial flux motor and a radial piston pump.

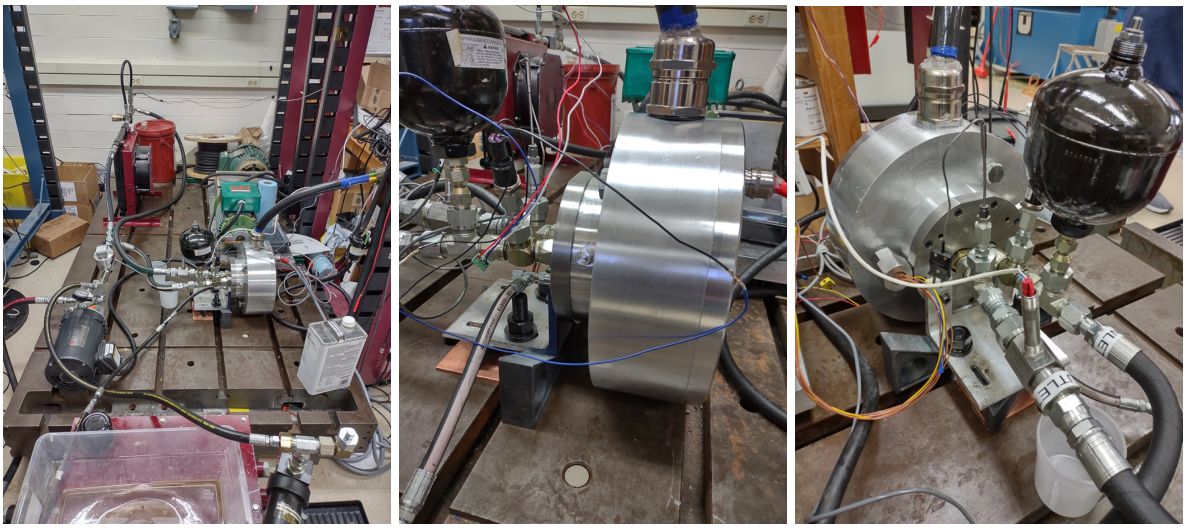

Fig. 3.C36: The integrated motor on the test-stand

The initial testing of the integrated machine involved running the hydraulic unit as a motor, and the electric unit as a generator. Three phase voltage waveform as shown in Fig. 3.C37 confirms the proper operation of the machine.

Fig. 3.C37: 3 phase voltage waveform confirms operation of the integrated machine

As testing progressed, unfortunately, the machine stopped working. It was revealed that the encoder which is necessary for the control of the power electronics has failed. Since the encoder is integrated in the machine (note that the integrated machine has not exposed shaft), a repair will require a complete teardown and rebuild of the machine. Also, because a replacement encoder is not readily available due to supply backlog, it was not possible to repair the sensor given the short time remaining. Effort was made to apply a self-sensing approach. Despite success in simulation, when the approach was applied to the setup, a component (may be a bearing) was apparently dislocated. At this point, it was decided that it was not possible to continue testing the integrated machine within the timeframe of the DOE grant. The team is however committed to repair the machine and continue testing.

Milestone 3.3: Control with integrated HECM:

Although the prototype integrated electric-hydraulic machine could not be directly tested, its capability to perform control was validated by the duty cycle test of the electric subsystem. Figs. 3.C21-3.C22 clearly show that the electric machine was able to track the torque trajectories demanded of the control based on OEM provided trajectories, and optimally selected pressure rails. Since the integrated HECM control is achieved by controlling the electric machine, these results also validate the integrated machine's control performance.

Milestone 3.4: Prototype integrated HECM characterized

The electric machine and hydraulic pump of the integrated HECM were separately characterized by the electrical engineering team and the hydraulic team respectively. Although these tests did not cover the entire operating range, the losses could be meaningfully extrapolated for other speeds and pressures. Moreover, since these tests capture nearly all the physics of the integrated HECM, the integrated HECM efficiency map can be obtained by combining the experimentally determined electric machine and the hydraulic pump efficiency maps. The efficiency map of the integrated HECM is plotted in Fig. 3.C38 below.

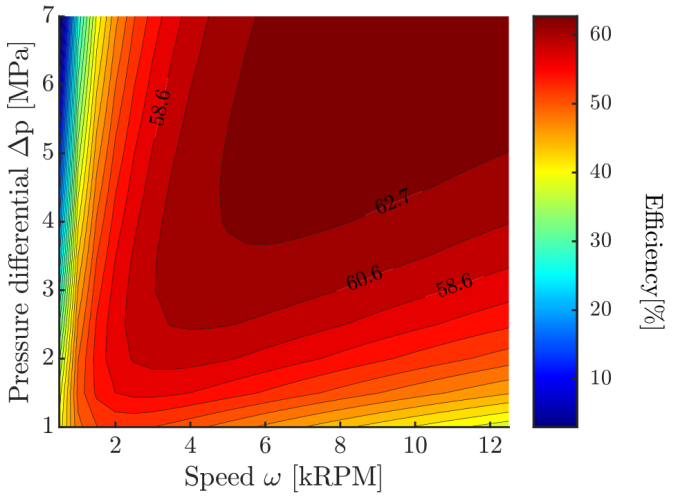

Fig. 3.C38: Efficiency map of the integrated HECM

It can be seen from Fig. 3.C38 that the peak efficiency of the integrated HECM is approximately 62.7% at the rated torque and speed. The lower than expected efficiency (of 85%) can be attributed to: a) larger than expected stator resistance; b) higher stator iron losses; c) higher air gap viscous losses; and most importantly, d) excessive leakage due to the larger than expected gap between the cylinder block and pintle.

With these results, the prototype integrated electric-hydraulic machine has been characterized.

Discussion on the performance of integrated electric-hydraulic machine

This project targets an active material power density of 5 kW/kg, efficiency greater than 85%, and active material cost of less than 20 $/kW for the integrated machine. This section discusses the performance of this prototype on each of these metrics and identifies avenues for future work.

a. **Power density:** The power output of the machine is the product of torque and speed. The electric machine torque capability was experimentally validated. Although the electric machine was only

tested up to 6000 RPM (rating of the dynamometer), since the bearings and other mechanical components have been rated for 12,500 RPM, this machine is capable of operating at the rated speed to achieve the rated power. The active material mass of this machine was computed to be 3.3 kg (1.88kg for the electric machine and 1.42kg for the hydraulic pump) using the machine dimensions and mass density of the materials used. This results in a power density of 6.1 kW/kg, clearly exceeding the project target of 5 kW/kg.

b. **Efficiency:** Although analytical models predicted that the HECM would meet the 85% efficiency target, the maximum efficiency of the integrated HECM from hardware measurements was found to be approximately 62.7%. As discussed earlier, there were higher than expected stator resistance; stator iron losses; air gap viscous losses; and excessive leakage gap between the cylinder block and pintle.

c. **Cost:** Based on commodity prices for the active materials, this machine was shown to meet the cost targets with an active material cost of 3.8 $/kW in the update for Task 2. C4 and Milestone C5. Since there was no change in the active materials used or the dimensions of the prototype design, this prototype HECM meets the cost targets.

It is expected that efficiency can be improved to reach the efficiency goal:

i. Using thicker gauge magnet wire, shorter end-windings, and using interconnects with low contact resistance can reduce the stator resistance and improve the efficiency by up to 1.2% at the rated power.

ii. Vertical orientation of the integrated machine can ensure that only the stator is in contact with the oil (for cooling) and the air gap has no oil. This eliminates the air gap viscous losses and is expected to improve the efficiency by up to 7% at the rated torque and speed. Alternatively, an oil spray cooling can also be used to avoid flooding the case with oil and achieve similar efficiency improvements.

iii. Post-processing the electric machine stator (by techniques such as annealing) can relieve the manufacturing stresses. This reduces the iron losses and can potentially improve efficiency by up to 2% at rated power. Using thinner gauge electrical steel can further improve efficiency by reducing the eddy current losses. However, this can increase the active material cost (undesirable).

iv. A tight tolerance between the cylinder block and pintle can decrease the leakage and increase the volumetric efficiency. Due to low tolerance, the measured leakage was approximately 2.5 times the analytically predicted value. If this leakage can be reduced, the efficiency can be improved by 10%.

In addition to meeting 2 of the 3 performance metrics, this project has successfully demonstrated the following innovations:

1. *Modeling, optimization, and fabrication of an axial flux electric machine:* Axial flux machines, although well-known for realizing power-dense designs, are challenging to fabricate[7] and have very low commercial availability compared to conventional radial flux machines. This project

[7] F. Nishanth, J. V. Verdeghem and E. L. Severson, "Recent Advances in Analysis and Design of Axial Flux Permanent Magnet Electric Machines," 2021 IEEE Energy Conversion Congress and Exposition (ECCE), 2021, pp. 3745-3752

developed a modeling and optimization framework for axial flux machines, fabricated a power-dense axial flux machine design, and characterized it to demonstrate the power density. The achieved electric machine power density (approximately 10 kW/kg considering active materials) features among the highest power density reported in the literature for electric machines without exotic materials. This will be of interest not just for hydraulic integration but also for other applications that benefit from high power density.

2. *High-speed hydraulic pump design:* To achieve the power density targets, this project has developed a high-speed hydraulic machine to directly interface with a high-speed 12,500 RPM electric machine without a gearbox. Conventional mobile hydraulic machines with premium efficiency are typically designed for operating speeds lower than 4,000 RPM. Although high-speed (> 10,000 RPM) hydraulic pumps have been developed for aerospace actuators, they are extremely inefficient and unsuitable to meet the efficiency targets in this project. Therefore, a novel Hydrostatic Radial Piston (HRP) Pump architecture is developed to solve this problem. This pump has a novel piston design with a spherical head that allows it to tilt while reciprocating inside the cylinder chamber and eliminates the need for a joint between the piston and slipper. Additionally, the cam is mounted on the bearing, allowing it to freely rotate keeping the same eccentric position with respect to the pintle. This unique design can significantly reduce frictional losses at the high speed operating conditions. This project developed a detailed framework of the pump design, beginning from the mathematical model development, optimization, and detailed CAD modeling to the experimental setup and characterization of the pump which are milestones for any high-speed pump design. This miniature pump has demonstrated its working capability at different operating conditions and fits nicely inside the hollow space of the designed AFPMSM machine to turn it into an integrated machine or, HECM. Other than HECM, it has a great prospect in the electro-hydraulic actuator (EHA) application.
3. *Tight integration of a high-speed hydraulic pump with an axial flux electric machine:* The integrated HECM developed in this project is one of the first designs to tightly integrate a power-dense axial flux machine with a high-speed hydraulic pump. This integration eliminates redundant components such as shaft seals and couplings, re-uses the common surfaces and bearings to improve the power density and efficiency and lower the cost compared to realizing a HECM that couples a discrete electric machine with a discrete hydraulic pump. It must be noted that most attempts to integrate hydraulic and electric machine designs reported in literature utilize low-speed gear pumps coupled with conventional radial flux electric machines. This project explored different integrated hydraulic-electric machine concepts based on the radial flux and axial flux electric machine configurations to come up with the final HECM design that promises to best meet the project targets and the practically relevant metrics such as fast response time which are necessary for commercialization. Additionally, the axial flux machine was designed to be cooled using the leakage from the hydraulic pump. This allowed pushing the axial flux machine stator current density to realize power-dense designs.
4. *Multi-physics optimization:* Power-dense electric machine designs are nearly always rated for high operating speeds (>10,000 RPM) owing to their limited torque density. Hydraulic machines are inefficient at high speeds as their losses increase as a function of operating speed. In addition, the integrated HECM developed in this project uses the hydraulic pump leakage to cool the electric machine. All these factors necessitate using a framework that evaluates the

electro-magnetic, hydraulic, and thermal design to explore the design space of the HECM. A multi-physics optimization framework was developed and used to investigate the trade-off between power density, cost, and efficiency to explore the integrated HECM design space. The findings from this multi-physics optimization showed that integrated HECM designs rated for operating speeds >13,000 RPM were power-dense but inefficient. Low speed (<10,000 RPM) HECM designs were efficient but failed to meet the power density targets. The optimization results showed that an operating speed of 12,500 RPM offered the best compromise between efficiency and power density with several designs meeting both the power density and efficiency targets. Based on the multi-physics optimization, a design that promises to meet the project targets was selected for prototyping.

4. Project Output

Patent:

1. P. Y. Li, “Device having hybrid hydraulic-electric architecture”, Utility U.S. Patent 11,060,539 (16/781,446, filed February 4, 2020, granted July 13, 2021).

Publications:

Journal papers:

1. P. Y. Li and J. Siefert, “Optimal control of the Energy Saving Hybrid Hydraulic-Electric Architecture (HHEA) for Off-Highway Mobile Machines”, IEEE Transactions on Control Systems, Accepted in November, 2021.
2. F. Nishanth, G. Bohach, M. M. Nahin, J. Van de Ven and E. L. Severson, "Design and Experimental Evaluation of a Power Dense Axial Flux Machine with an Integrated Hydraulic Pump to Electrify Off-Highway Vehicles," IEEE Transactions on Industry Applications. Accepted in July 2022.

Conference papers:

1. Nishanth FNU, Bohach, G., Van de Ven, J., and Severson, E. 2019, “Design of a Highly Integrated Electric-Hydraulic Machine for Electrifying Off-Highway Vehicles”, IEEE Energy Conversion Congress and Exposition (ECCE-2019), Sept. 29-Oct.3, 2019. Baltimore, MD.
2. P. Y. Li, J. Siefert, and D. Bigelow, 2019, “Hybrid Hydraulic-Electric Architecture for Mobile Machines”, 2019 ASME/Bath Symposium on Fluid Power and Motion Control, Sarasota, FL, Oct 7 - Oct. 9, 2019.
3. Bohach, G., Nishanth, Severson, E., and Van de Ven, J., 2019, "Modeling and Optimization Study of a Tightly Integrated Rotary Electric Motor-Hydraulic Pump," 2019 ASME/Bath Symposium on Fluid Power and Motion Control, Sarasota, FL, Oct 7 - Oct. 9, 2019.
4. J. Siefert and P. Y. Li 2020, “Optimal Operation of a Hybrid Hydraulic Electric Architecture (HHEA) for Off-Road Vehicles Over Discrete Operating Decisions”, 2020 American Control Conference, Denver, June 2020.
5. A. Chatterjee and P. Y. Li 2020, “Motion Control of Hydraulic Actuators In the Presence of Discrete Pressure Rail Switching,” 2020 ASME/IEEE Int. Conference on Advanced Intelligent Mechatronics, Boston (Virtual), July 2020.
6. F. Nishanth, A. Khamitov and E. L. Severson, "Comparison of Linear and Rotary Electric

Machine Topologies for a Hybrid Hydraulic Electric Architecture of Off-Highway Vehicles", *2020 IEEE Transportation Electrification Conference and Exposition (ITEC)*, Chicago, IL (Virtual) September, 2020, pp. 1-6.

7. J. Siefert and P. Y. Li, "Optimal Control and Energy-Saving Analysis of Common Pressure Rail Architectures: HHEA and STEAM", 2020 Bath/ASME Sym. on Fluid Power & Motion Control, FPMC2020-2801, September 9-11, Bath, UK (virtual) 2020.
8. G. Bohach, M. M. Nahin, E. Severson, and J. Van de Ven, “Impact of Dynamics on the Losses at Radial Ball Piston Pump Interfaces,” 2020 Bath/ASME Symposium on Fluid Power and Motion Control, FPMC2020-17761, September 9-11, Bath, UK (virtual) 2020.
9. F. Nishanth, G. Bohach, J. Van de Ven and E. L. Severson, "Design of an Axial Flux Machine with an Integrated Hydraulic Pump for Off-Highway Vehicle Electrification", 2020 IEEE Energy Conversion Congress and Exposition (ECCE), Detroit, MI, Oct 2020, pp. 22 1-6
10. F. Nishanth, J. V. Verdeghem and E. L. Severson, "Recent Advances in Analysis and Design of Axial Flux Permanent Magnet Electric Machines," 2021 IEEE Energy Conversion Congress and Exposition (ECCE), 2021, pp. 3745-3752
11. A. Khandekar, J. Siefert and P. Y. Li, “Co-Design of a Fully Electric Hybrid Hydraulic-Electric Architecture (FE-HHEA) for Off-Road Mobile Machines,” 2021 American Control Conference, New Orleans LA, June 2021.
12. Md Minal Nahin, Garrett R Bohach, FNU Nishanth, Eric L Severson, James D Van de Ven, “Dynamic Modeling and Design of a Radial Hydrostatic Piston Pump for Integrated Pump-Motor”, ASME/Bath Symposium on Fluid Power and Motion Control, Bath, UK, October 19, 2021, FPMC2021-68788 (URL: https://doi.org/10.1115/FPMC2021-68788)
13. J. Wills, A. Keester, and P.Y.Li, "A Power Take-Off (PTO) for Wave Energy Converters Based On the Hybrid Hydraulic-Electric Architecture (HHEA)", 2021 ASME/Bath Sym. on Fluid Power and Motion Control (FPMC 2021), Oct. 19-21, 2021. (Virtual)
14. A. Khandekar, J. Wills, M. Wang, and P. Y. Li, "Incorporating Valve Switching Losses Into a Static Optimal Control Algorithm for the Hybrid Hydraulic-Electric Architecture", 2021 ASME/Bath Sym. on Fluid Power and Motion Control (FPMC 2021), Oct. 19-21, 2021. (Virtual)
15. A. Chatterjee and P.Y.Li, "HIL Testbed and Motion Control Strategy for the Hybrid Hydraulic Electric Architecture (HHEA)", 2021 ASME/Bath Symposium on Fluid Power and Motion Control (FPMC 2021), Oct. 19-21, 2021. (Virtual)
16. J. Wills and P. Y. Li, “Accumulator sizing for the hybrid hydraulic electric architecture (HHEA) using dynamic programming” ASME/Bath Sym. on Fluid Power and Motion Control, Sept 2022 (To appear).
17. F. Nishanth and E. L. Severson, "A Review of Torque-Dense Electric Drive Systems with Potential to Bridge the Gap with Hydraulics for Off-Highway Vehicle Electrification," 2022 IEEE/AIAA Transportation Electrification Conference and Electric Aircraft Technologies Symposium (ITEC+EATS), 2022, (Accepted) June 14-17, 2022, Anaheim, CA, pp. 1-6.

Follow-On Funding

This project led to another DOE project: DE-EE0009875: “Fully Electric Powered, Hydraulic Assisted, Compact Track Loader” with the goal of applying the HHEA to a Compact Track Loader machine.

Acknowledgment and Disclaimer:

Acknowledgment: This material is based upon work supported by the U.S. Department of Energy's Office of Energy Efficiency and Renewable Energy (EERE) Vehicle Technologies Office (VTO) Award Number DE-EE008384.

Reference

[1] L. J. Love, "Estimating the Impact (Energy, Emissions and Economics) of the US Fluid Power Industry." 2012. doi: 10.2172/1061537.

[2] S. Helduser, "Electric-hydrostatic drive—an innovative energy-saving power and motion control system," *Proceedings of the Institution of Mechanical Engineering - Part I*, vol. 213, pp. 427–437, 1999, [Online]. Available: http://journals.sagepub.com/doi/abs/10.1243/0959651991540250

[3] M. Vukovic, S. Sgro, and H. Murrenhoff, "STEAM: A Mobile Hydraulic System With Engine Integration," *ASME/BATH 2013 Symposium on Fluid Power and Motion Control*. 2013. doi: 10.1115/fpmc2013-4408.

[4] Z. Du, K. L. Cheong, and P. Y. Li, "Energy management strategy for a power-split hydraulic hybrid vehicle based on Lagrange multiplier and its modifications," *Proceedings of the Institution of Mechanical Engineers, Part I: Journal of Systems and Control Engineering*, vol. 233, no. 5. pp. 511–523, 2019. doi: 10.1177/0959651818801416.

[5] J. Siefert and P. Y. Li, "Optimal Control of the Energy-Saving Hybrid Hydraulic-Electric Architecture (HHEA) for Off-Highway Mobile Machines," *IEEE Trans. Control Syst. Technol.*, pp. 1–12, 2021, doi: 10.1109/TCST.2021.3131435.

[6] J. Siefert and P. Y. Li, "Optimal Operation of a Hybrid Hydraulic Electric Architecture (HHEA) for Off-Road Vehicles Over Discrete Operating Decisions," in *2020 American Control Conference (ACC)*, Jul. 2020, pp. 3255–3260. doi: 10.23919/ACC45564.2020.9147839.

[7] A. Chatterjee and P. Y. Li, "HIL Testbed and Motion Control Strategy for the Hybrid Hydraulic-Electric Architecture (HHEA)," Dec. 2021. doi: 10.1115/FPMC2021-68888.

[8] J. Siefert and P. Y. Li, "Optimal Control and Energy-Saving Analysis of Common Pressure Rail Architectures: HHEA and STEAM," *BATH/ASME 2020 Symposium on Fluid Power and Motion Control*. 2020. doi: 10.1115/fpmc2020-2799.

[9] A. Chatterjee and P. Y. Li, "Motion Control of Hydraulic Actuators In the Presence of Discrete Pressure Rail Switching," in *2020 IEEE/ASME International Conference on Advanced Intelligent*

Mechatronics (AIM), Jul. 2020, pp. 1956–1961. doi: 10.1109/AIM43001.2020.9158837.
[10] A. Khandekar, J. Wills, M. (Rachel) Wang, and P. Y. Li, “Incorporating Valve Switching Losses Into a Static Optimal Control Algorithm for the Hybrid Hydraulic-Electric Architecture (HHEA),” Dec. 2021. doi: 10.1115/FPMC2021-69045.
[11] J. Wills and P. Y. Li, “accumulator sizing for the hybrid hydraulic electric architecture (HHEA) using dynamic programming,” in *2022 BATH/ASME Symposium on Fluid Power and Motion Control*, Bath, England, pp. FPMC20222–90184.
[12] “IEEE Trial-Use Recommended Practice for the Preparation and Use of Symbols.” doi: 10.1109/ieeestd.1966.120169.
[13] F. N. U. Nishanth, G. Bohach, M. M. Nahin, J. Van de Ven, and E. L. Severson, “Development of an Integrated Electro-Hydraulic Machine to Electrify Off-highway Vehicles,” *IEEE Transactions on Industry Applications*. pp. 1–12, 2022. doi: 10.1109/tia.2022.3189609.
[14] M. M. Nahin, G. R. Bohach, F. N. U. Nishanth, E. L. Severson, and J. D. Van de Ven, “Dynamic Modeling and Design of a Radial Hydrostatic Piston Pump for Integrated Pump-Motor,” Dec. 2021. doi: 10.1115/FPMC2021-68788.